Title
Spectroscopic Characterizations of the Topological Insulator Bi2Se3

Author
Gross, Adam L

Publication Date
2023

Peer reviewed|Thesis/dissertation

Spectroscopic Characterizations of the Topological Insulator Bi_2Se_3

By

ADAM L. GROSS

DISSERTATION

Submitted in partial satisfaction of the requirements for the degree of

DOCTOR OF PHILOSOPHY

in

PHYSICS

in the

OFFICE OF GRADUATE STUDIES

of the

UNIVERSITY OF CALIFORNIA

DAVIS

Approved:

Inna M. Vishik, Chair

Dong Yu

Richard T. Scalettar

Slavomir Nemsak

Committee in Charge

2023

Abstract

Bi_2Se_3 is an ideal three-dimensional topological insulator in which chemical modifications such as doping and intercalation can be used to engineer surface properties or to further functionalize the topological surface state. In this work, we study the Bi_2Se_3 system of materials with three experimental techniques: 1) ultrafast optical pump-probe spectroscopy (OPP), 2) angle-resolved photoemission spectroscopy (ARPES), and 3) X-ray photoelectron spectroscopy (XPS). These spectroscopic techniques are utilized to study the out-of-equilibrium carrier properties, surface chemistry, and band structure of Bi_2Se_3, $Bi_{2-x}Sb_xSe_3$, and $Cu_xBi_2Se_3$.

The photoexcited carrier decay in $Bi_{2-x}Sb_xSe_3$ nanoplatelets was studied with ultrafast optical pump-probe spectroscopy, demonstrating a substantial slowing of the bulk carrier relaxation time in bulk-insulating $Bi_{2-x}Sb_xSe_3$ as compared to n-type bulk-metallic Bi_2Se_3 at low temperatures, which approaches 3.3 ns in the zero pump fluence limit. This long-lived decay is correlated across different fluences and antimony concentrations, revealing unique decay dynamics not present in n-type Bi_2Se_3, namely the slow bimolecular recombination of bulk carriers.

Using ambient pressure X-ray photoelectron spectroscopy, copper migration in intercalated $Cu_xBi_2Se_3$ is demonstrated, occurring on a timescale of hours to days after initial surface cleaving. The increase in near-surface copper proceeds along with the oxidation of the sample surface and large changes in the selenium content, with the development of copper and selenium gradients. These complex changes are further modelled with core level spectroscopy simulations (SESSA), which suggest a composition gradient near the surface which develops with oxygen exposure. These results shed light on a phenomenon that must be considered in intercalated topological insulators and intercalated materials in general.

Contents

Acknowledgments

When John Donne wrote down his famous 17th century words "No man is an island," he probably meant to say "No man's PhD dissertation in experimental physics is an island." Indeed, no PhD is solely built from individual effort alone. Here, I would like to thank the numerous collaborators and others who helped contribute to the experiments, data analysis, and publications in this work.

First, I extended my enormous gratitude to my PhD advisor Inna, who was brave enough to take on the risk of selecting me as the first PhD student in the lab at UC Davis. I learned far more from her about the process of experimental science than I initially set out planning to do. Her mentorship and research instincts were instrumental in helping my growth as a scientist, and her network of collaborators was crucial to making this work possible. I especially thank her for the intellectual and creative freedom she gave me throughout the PhD program in setting up and designing experiments, which in retrospect was a fantastic and rare situation to be in as a student. I am happy to report that no new equipment was damaged throughout the process! With the exception possibly being a BBO crystal (and perhaps an ND filter wheel).

For the $Cu_xBi_2Se_3$ project, I supremely thank Slavomir Nemsak and Lorenz Falling from the Advanced Light Source at Berkeley Lab. Without them and the facilities at LBNL, large portions of this thesis would not be possible. I thank Slavo for sharing his impressive command of synchrotron science and Lorenz for patiently explaining the numerous complications and pitfalls faced in XPS experiments. The capabilities and collective knowledge at LBNL are truly impressive. Much additional thanks to Henrique Martins for the initial synchrotron observations of Cu migration in $Cu_xBi_2Se_3$ and Kristie Koski for preparing the $Cu_xBi_2Se_3$ samples.

I want to extend my sincere gratitude to my collaborators Dong Yu, Yasen Hou, and Antonio Rossi. During my first two years at UC Davis, their feedback and advice were

enormously helpful in starting my research. Without Yasen's experimental know-how, the Bi_2Se_3 nanoplatelets would never have been made, and I would remain terrified of handling liquid helium. I thank Dong for all of the underlying work he has done on TIs, and for serving as the chair of my qualifying exam committee. I thank Antonio for introducing me to synchrotron experiments at the Advanced Light Source, and I appreciated our hard work in getting the lab set up at UC Davis. I thank Peter Klavins, David Barnes, and the machine shop crew for their hard efforts during the lab construction and moving process.

Several others must also be mentioned. From the lab at UC Davis: Matthew Staab for ARPES experiments, Kevin Fillhouer for ultrafast optics experiments and discussions on physics, and Sudheer Anand. I also thank Luke McClintock, Clark Travaglini, Rahim Ullah, and Metzli Montero for assistance with various experimental measurements and equipment issues. I again thank Peter Klavins for his crucial support in these areas as well. Additionally from Sandia: Tzu-Ming Lu, Chris Smyth, and Taisuke Ohta, for experiments and guidance on the ion irradiated-TaS_2 project. The summer in New Mexico helped me appreciate the novel and contemporary research directions in 2D materials and microelectronics.

Finally, my friends and my family, especially my parents, who have always been supportive during my studies. It took nearly six years, but I am happy to be finally finished, and excited for what the future holds.

Funding Acknowledgments

For the initial setup of the optical pump-probe experiment: UC Davis startup and NSF DMR-1838532 (Chapter 2 and Chapter 3). For ARPES measurements at UC Davis: UC Davis startup (Chapter 4). For the setup of 6 eV laser ARPES: DOE Contract No. DE-SC0014697 (Chapter 4).

For the AP-XPS components of the $Cu_xBi_2Se_3$ study: the Laboratory Directed Research and Development (LDRD) Program at Lawrence Berkeley National Laboratory under a grant titled 'Photoemission Investigations of Layered 2D Materials', and the Alfred P Sloan Foundation (FG-2019-12170) (Chapter 5 and Chapter 6). For the ARPES components of the $Cu_xBi_2Se_3$ study: AFOSR Grant No. FA9550-18-1-0156. (Chapter 6). This research used resources of the Advanced Light Source, which is a DOE Office of Science User Facility under contract no. DE-AC02-05CH11231.

For the acquisition of the Kratos AXIS Supra$^+$ instrument at UC Davis: NSF-DMR-MRI-1828238; and the collection of data: NSF-DMR-1838532 (Chapter 5 and Chapter 6).

List of Figures

Chapter 1

Introduction

Quantum materials are a categorization of materials, referring to any material where quantum mechanical effects play a dominant role in establishing macroscopic properties [1–8]. These materials include superconductors, topological insulators, Weyl and Dirac semimetals, 2D materials, and compounds exhibiting many-body electron correlations such as Mott insulators. Much of contemporary research in condensed matter physics is centered on experimentally characterizing quantum materials' properties, theoretically modeling their properties, and discovering new quantum materials, where ultimate progress in the field depends on a combination of all three approaches.

This work primarily focuses on the experimental study of one specific quantum material, the topological insulator Bi_2Se_3, as well as chemically doped and intercalated variants of Bi_2Se_3, using several different experimental techniques. Topological insulators are quantum materials that posses an insulating bulk and metallic surface states, demonstrating fundamentally new electron physics as compared to traditional classifications of materials such as normal insulators, semiconductors, and metals [1,9–15]. The properties of topological insulators are of great interest for technological applications in spintronics, quantum electronics, and optoelectronics [16–26]. Further characterization of their properties, both in and out

of equilibrium, are thus needed for validating any future uses of topological insulators in technology.

1.1 Overview of three-dimensional topological insulators

Here, we will briefly summarize the background behind topological insulators, specifically focusing on three-dimensional topological insulators (3D TIs) and the aspects specific to Bi_2Se_3. In general, a TI phase exists if the crystal Hamiltonian cannot be adiabatically transformed into that of a normal insulator (that is, slowly, without exiting the ground state) without passing through a conducting state [12]. This physically manifests in 3D TIs as an insulating bulk and conducting, metallic states at the surface. For a broader discussion of the theory underlying topological quantum materials, many excellent works provide detailed explanations which discuss the role of wavefunction topology, topological invariants, and the Berry phase in topological insulators [1, 9, 10, 12–15, 27, 28].

There are many distinct categories of topological quantum materials. These include, but are not limited to 3D TIs, 2D TIs (or quantum spin Hall insulators), topological crystalline insulators, topological Kondo insulators, Dirac semimetals, and Weyl semimetals [14, 15, 29]. These classifications are distinguished from one another by differences in present symmetries and by different possible topological invariants. Insulators that do not posses any novel topological features in their electronic band structures are considered topologically trivial. Indeed, it is becoming increasingly clear that most non-magnetic materials harbor at least some topological features in their band structures [30].

The nontrivial topology that distinguishes Bi_2Se_3 from a regular insulator arises from the band inversion at the Γ point in the Brillouin zone [13], which is caused by strong spin-orbit coupling (SOC) [31]. SOC of electrons arises when the magnetic dipole moment of an orbiting electron interacts with the electrostatic field of the nucleus, or equivalently a magnetic field in the rest frame of the electron ($\Delta H = -\mu \cdot B$). An illustrative schematic describing band inversion in Bi_2Se_3 is shown in Figure 1.1. When considering the bands of

Bi_2Se_3 without SOC, the bulk conduction and valence bands would not overlap, with the valence band (Se 4p) separated from the conduction band (Bi 6p) (Fig. 1.1(a)). In Bi_2Se_3, the large nuclear mass of Bi confers strong SOC to this system [10], so SOC must be included in modeling the bands [31]. When SOC is present, the conduction and valence bands invert (Fig. 1.1(b)) and split, opening up a bulk band gap (Fig. 1.1(c)). With this arrangement of bands, a topological insulator phase is now realizable.

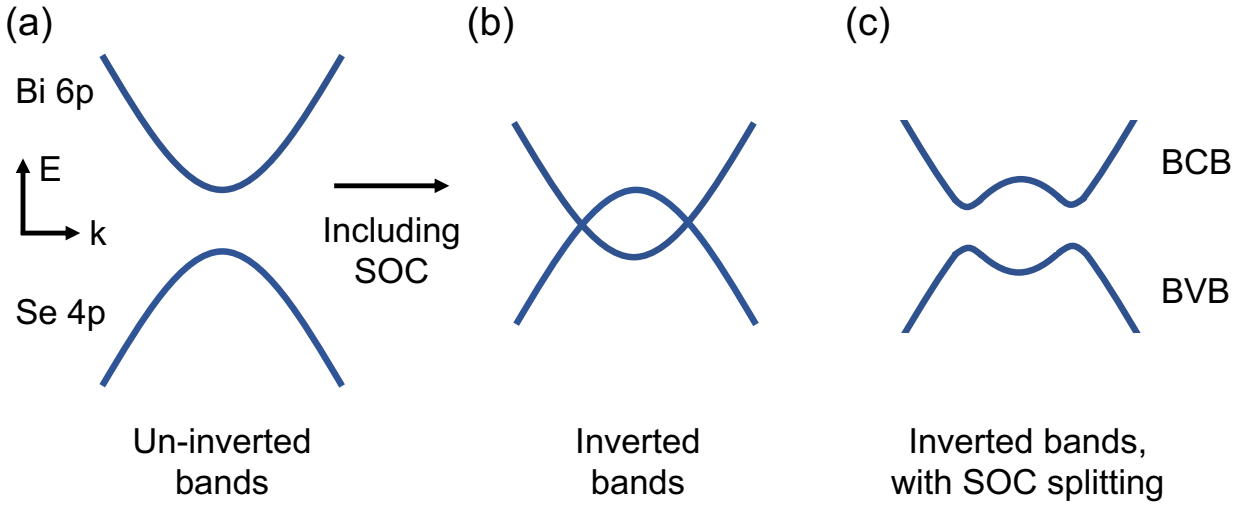

FIGURE 1.1. Band inversion in Bi_2Se_3. (a) Un-inverted bulk bands showing the Bi 6p conduction band (BCB) and Se 4p valence band (BVB). (b) Inverted bulk bands. (c) Final split bands, after including SOC. Figure adapted from Ref. [32].

There are several other aspects needed to fully realize a 3D TI. Importantly, the Hamiltonian must possess time-reversal symmetry [9, 10, 12, 27, 31]:

$$\Theta H(\mathbf{k})\Theta^{-1} = H(-\mathbf{k}) \tag{1.1}$$

where Θ is the antiunitary time-reversal symmetry operator, and $\mathbf{k}$ is the crystal momentum of the Hamiltonian H. In this sense, the topology of this system can be understood as being "protected" by the time-reversal symmetry of the Hamiltonian. In three dimensions, TIs have four topological invariants ($\mathbb{Z}_2$), which correspond to four degenerate points $\Gamma_{1,2,3,4}$ in

the surface Brillouin zone, each of which is also time-reversal symmetry invariant. These degenerate points are known as time-reversal invariant points.

Each time-reversal invariant point is identified with a corresponding surface state that obeys a linear Dirac dispersion relation. This specific dispersion relation arises from diagonalizing the two-dimensional Dirac Hamiltonian:

$$H_D = c\sigma \cdot \mathbf{p} + mc^2\sigma_z \tag{1.2}$$

where σ are the Pauli matrices and $\mathbf{p}$ is the electron momentum operator. In solid state materials, the speed of light c is replaced with the Fermi velocity v_F, and the mass vanishes $m \to 0$, closing the gap in the Dirac or "light-like" state. The Dirac Hamiltonian is by definition present in all Dirac materials, including in 3D TIs where it harbors a surface Dirac state [15]. The crossing point of the linear dispersions is called a Dirac point in the band structure, and a Dirac point is present in Bi_2Se_3 as well. It should be noted that in conventional materials like metals or doped semiconductors, the Hamiltonian takes the form $H = \frac{\mathbf{p}^2}{2m^*}$ and obeys the Schrodinger equation with effective mass m^*. In this sense, Dirac materials are a distinct classification of matter fundamentally different from the free quasiparticle picture of Schrodinger fermions [15].

Another consequence of strong SOC is that the surface states of 3D TIs exhibit spin-momentum locking of carriers at the surface [33]. Spin-momentum locking is a major property of carriers in TIs, which constrains spin-up electrons to move with momentum $+p$ and spin-down electrons to move in the opposite direction with momentum $-p$, prohibiting direct backscattering of carriers [11, 13]. Due to the presence of time-reversal symmetry and the topological invariants of this system, which apply to TIs like Bi_2Se_3 globally, the surface states are robust to local perturbations such as impurities and disorder in the material [34], so long as time-reversal symmetry is not broken. For example, spin-momentum locking is still present at the surface of Bi_2Se_3 even in fully amorphized thin film forms [34].

Technological proposals taking advantage of the reduced carrier backscattering and spin textures in Bi_2Se_3 greatly benefit from the protection afforded by topology, which is not the case in topologically-trivial materials [9, 12, 35–37]. As will be discussed in Chapter 4, the surface band structure of Bi_2Se_3 is directly measurable using angle-resolved photoemission spectroscopy (ARPES), which is the ideal tool for characterizing its topological surface properties.

1.2 Overview of Bi_2Se_3

Bi_2Se_3 has a bulk direct band gap of about 0.3 eV [13, 31], which is 13 times higher than room temperature energies and thus favorable for electronic and optical applications. The Bi_2Se_3 Fermi surface is isotropic unlike in the related 3D TI Bi_2Te_3, where it is hexagonal and warped due to cubic Dresselhaus spin-orbit coupling [13]. The Dirac point of Bi_2Se_3 lies within the bulk band gap and is well separated from the bulk bands, which is also not evident in Bi_2Te_3 [13, 33, 38–40]. This is a major appeal of Bi_2Se_3: its topological surface state is energetically distinct from its bulk states, allowing for greater access and control of the topological surface state in possible applications. Bi_2Se_3 has a single surface state compared to the first characterized 3D TI $Bi_{1-x}Sb_x$, which was observed to have five [41]. Additionally, Bi_2Se_3 is routinely synthesized in large, single crystal forms [42]. The synthesis uses common crystal growth methods [33, 38, 42, 43], and does not require manufacturing of heterostructures for achieving desired properties. The ease of synthesis and the existence of topological surface states in Bi_2Se_3 have greatly accelerated the surface characterization of this system. It should be noted that many of these TI properties are also preserved in insulating alloys [44].

Bi_2Se_3 has a tetradymite, rhombohedral structure that can be visualized as quintuple layers (Se-Bi-Se-Bi-Se) separated by Van der Waals gaps. The crystal structure is shown below in Figure 1.2. The broader family of bismuth-based topological insulators including Bi_2Se_3, Bi_2Te_3, Bi_2Te_2Se (BTS), and $Bi_{2-x}Sb_xTe_{3-y}Se_y$ (BSTS), has wide latitude to be

tuned chemically. The ability to chemically substitute in the sample synthesis is especially valuable because doing so can controllably tune major material properties, such as the chemical potential. Having the chemical potential be positioned inside the band gap can help limit detection of purely bulk phenomena, allowing better detection of purely surface state phenomena in experiments. The consequences of this on the carrier dynamics in $Bi_{2-x}Sb_xSe_3$ will be further explored in Chapter 3.

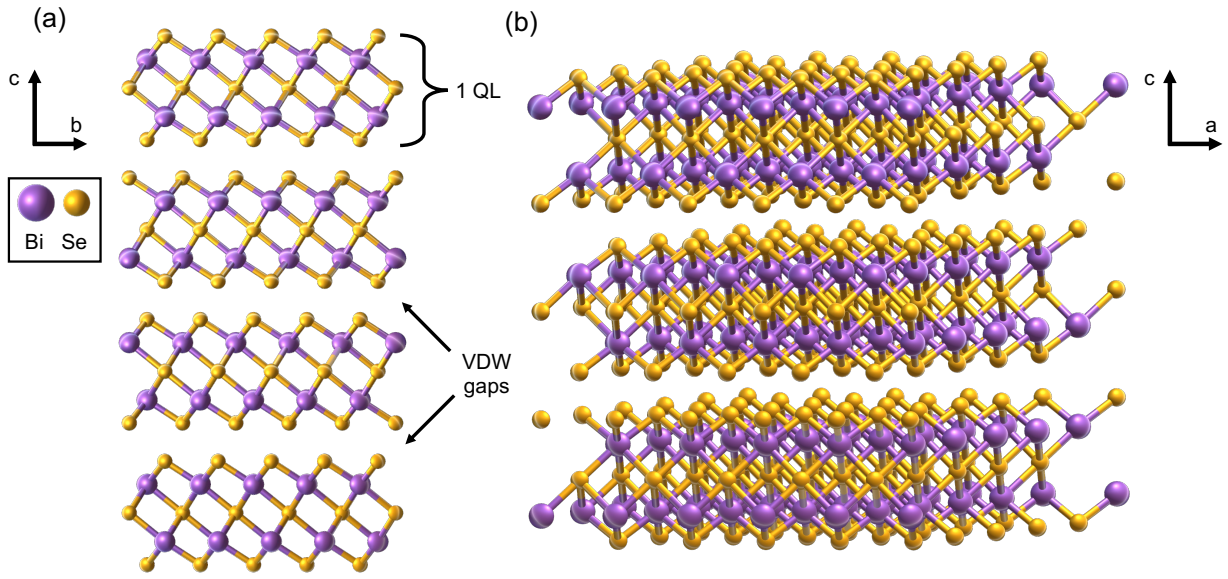

FIGURE 1.2. Crystal structure of Bi_2Se_3. (a) Structure shown along the a-axis. One quintuple layer (QL) and the Van der Waals gaps are indicated. (b) Structure shown along the b-axis with a slight tilt. The crystal structures have been rendered using the software in Ref. [45].

The crystal structure of Bi-based TIs also permits chemical intercalation. Intercalation is the insertion of atoms or molecules between layers, and in the case of Bi-based TIs, species are intercalated into the van der Waals gaps between adjacent quintuple layers. This can further alter the properties of TIs, such as producing superconductivity in $Cu_xBi_2Se_3$ by intercalating copper [46–53]. In modern condensed matter physics research, tunable materials systems like these are highly desirable as they allow for study of multiple phases in

close physical proximity (e.g., both superconductivity and topological surface states at the material surface), which may further lead to new applications.

1.3 Outline of this work

This work will be organized as follows. First, an introduction to ultrafast optical pump-probe spectroscopy will be given, providing a description of the experimental apparatus at UC Davis (Chapter 2). Following this, ultrafast optical pump-probe data on Bi_2Se_3 will be presented and compared to data on $Bi_{2-x}Sb_xSe_3$ nanoplatelets, showing evidence of long carrier lifetimes across differently doped samples (Chapter 3). In Chapter 4 and Chapter 5, overviews of ARPES and XPS experimental techniques will be provided, being discussed in the context of the Bi_2Se_3 materials system. Lastly, results from synchrotron-based AP-XPS experiments on intercalated $Cu_xBi_2Se_3$ will be presented and discussed (Chapter 6), showing evidence of Cu migration in $Cu_xBi_2Se_3$ samples when exposed to controlled ambient conditions.

Chapter 2

Ultrafast optical pump-probe spectroscopy

2.1 Introduction

Ultrafast optical pump-probe spectroscopy (OPP) is a time-resolved pump-probe technique that is extremely versatile in terms of the materials and out-of-equilibrium phenomena it can access. Ultrafast optical techniques are able to measure quantities such as electronic carrier lifetimes and carrier decay dynamics as a function of temperature, pump fluence, and different material compositions. Carrier dynamics behavior measured with an optical pump-probe experiment can be related to underlying phases present in the material, both in fluence- and temperature-dependent manners. In this chapter, we discuss the fundamentals behind the technique, focusing the discussion on the specific OPP setup constructed at UC Davis.

In an OPP experiment, a pump pulse creates excitations into originally unoccupied states, and a second probe pulse measures the transient change in reflectivity $\Delta R/R$ (or transmission) at a time delay t_{delay} later while the excited states return to equilibrium. The magnitude of $\Delta R/R$ can be used as a proxy for the number of nonequilibrium electron-hole excitations [54], and its evolution $\Delta R(t_{\text{delay}})/R$ can reveal the processes by which photoexcited carriers return to equilibrium. Recently, OPP has been successful in studying low-energy

excitations (i.e., sub-excitation frequency) in superconductors [54–57], charge density wave systems [58], correlated electron systems [59], and topological quantum materials [60–62].

In OPP, the pump and probe photon energies (E_{ph}) can either be different or be degenerate. In the experiments in this thesis, a degenerate $E_{\text{ph}} = 1.55\,\text{eV}$ (or wavelength $\lambda = 800\,\text{nm}$) is used for the pump and the probe. OPP can measure changes in the reflectivity, which ultimately depend on the complex dielectric function [63]:

$$\frac{\Delta R}{R} = \frac{\partial \ln R}{\partial \epsilon_1}\Delta\epsilon_1(t) + i\frac{\partial \ln R}{\partial \epsilon_2}\Delta\epsilon_2(t), \tag{2.1}$$

where R is the reflectivity, ϵ_1 and ϵ_2 are the real and imaginary components of the complex dielectric function ($\epsilon(\omega) = \epsilon_1(\omega) + i\epsilon_2(\omega)$), and Δ denotes changes in these quantities following the initial pump excitation [63]. The transient changes in $\epsilon_2(\omega)$ are directly caused by transient changes in the joint density of states (JDOS) near the Fermi energy E_F [63, 64]. The dielectric function $\epsilon(\omega)$ can be further related to the optical conductivity $\sigma(\omega)$ by $\epsilon(\omega) = \epsilon_0 + i\frac{\sigma(\omega)}{\omega}$.

While OPP with $E_{\text{ph}} = 1.55\,\text{eV}$ pulses does not directly couple to lower energy excitations due to the different energy scales involved, it is still sensitive to lower energy carrier dynamics, which will be explained below. After photoexcitation, $\epsilon_2(\omega)$ changes according to the expression [65]:

$$\epsilon_2(\omega) = \frac{16\pi e^2}{\omega^2}\sum_{v,c}|M_{v,c}|^2\delta(\hbar\omega - (E_c - E_v)), \tag{2.2}$$

where v, c label the valence and conduction bands respectively, $|M_{v,c}|$ are the matrix elements connecting transitions between the bands, and $\delta(\hbar\omega - (E_c - E_v))$ is the JDOS. The real component of $\epsilon(\omega)$ can be related to the imaginary component by the corresponding Kramers-Kronig relation:

$$\epsilon_1(\omega) = 1 + \frac{2}{\pi}P\int_0^\infty \frac{\omega'\epsilon_2(\omega')}{\omega'^2 - \omega^2}d\omega'. \tag{2.3}$$

Because OPP measures changes in the reweighted JDOS post-excitation [64], and the Kramers-Kronig relations for $\epsilon_1(\omega)$ and $\epsilon_2(\omega)$ apply over all frequencies ω, changes in $\epsilon(\omega)$ at lower frequencies (or meV energies) can be indirectly picked up by the probe at higher frequencies (or eV energies). See Ref. [64] for further discussion of a method to obtain the full dielectric function in OPP. Fortunately, it is possible to achieve a $\Delta R/R$ sensitivity of 10^{-5} or greater in materials with good reflectivity with $E_{\text{ph}} = 1.55\,\text{eV}$, making OPP capable of inferring low energy carrier dynamics.

It is quite common for pump-probe measurements, if performed with sufficiently low intensity to avoid melting low-temperature orders, to observe dramatic changes at phase transitions involving very low energy modifications of single-particle spectra (e.g. superconductivity, CDWs, heavy fermion hybridization gaps, etc.) [54, 56, 63, 66–72]. Still, THz-probes can provide a more direct measure of meV-scale excitations and the optical conductivity $\sigma(\omega)$, at the cost of a larger spot size and a stronger constraint on the type of samples that can be studied (i.e., THz-transparent) [63]. Due to the practically of optical wavelengths and greater compatibility with standard optics, OPP is the more versatile of the two.

2.2 Ultrafast laser optics

Here, we provide a concise overview of the engineering and operation of the ultrafast laser used in the OPP setup at UC Davis. All of the OPP data in this work has been obtained using pulses generated using a Spectra Physics Mai Tai laser with a Ti:Sapphire lasing medium comprised of Ti^{3+}-doped Al_2O_3, utilizing active modelocking to generate a steady stream of optical pulses. Internally, the Mai Tai is actually comprised of two lasers: a green $\lambda = 532\,\text{nm}$ continuous wave (CW) laser and a regenerative, actively-modelocked Ti:Sapphire cavity pumped by the CW laser. Briefly, active modelocking can be summarized by the Master Equation [73, 74]:

$$T_R \frac{\partial A(t,T)}{\partial T} = -\Big((l-g) - \frac{g}{\Delta\Omega^2}\frac{\partial^2}{\partial t^2} + \frac{1}{2}M\omega_m t^2\Big)A(t,T). \tag{2.4}$$

The modelocking of pulses $A(t,T)$ is accomplished by introducing a periodic loss element (the final term in the Master Equation) modulated at a frequency $\omega_m = 2\pi/T_R$ with pulse cavity round-trip time T_R. In active modelocking, a fixed phase relationship between the cavity longitudinal modes with gain bandwidth $\Delta\Omega$ allows these modes to constructively interfere, generating an ultrafast train of pulses with steady-state pulse duration $\tau = \left(\frac{2g}{\Delta\Omega^2 M\omega_m^2}\right)^{1/4}$.

The main difference between the Mai Tai and the basic actively-modelocked laser is that the periodic loss element in the Mai Tai (an acousto-optic modulator) is not driven by an external frequency, but rather by an RF signal measured from within the laser cavity itself. Regenerative modelocking helps alleviate one of the main challenges of active modelocking, namely that the modulator need be driven at precisely ω_m, which is highly dependent on the cavity round-trip time T_R or length. Initially after powering on, the output modes of the CW laser are partially phase-locked, which results in beat frequencies $f = c/2L$. Inside the Mai Tai, a photodiode measures the intensity of the CW mode-beating, the resulting signal is phase-adjusted, amplified, and then fed back into the AOM for steady-state operation [**75**]. This regenerative feedback circuit allows the AOM to have optimally-timed transmission, so the final modelocked output of the Ti:Sapphire cavity is stable with a fixed phase relationship between the cavity modes, with minimal synchronization issues allowing steady state generation of pulses as short as $\sim 80\,\text{fs}$ with a $80\,\text{MHz}$ repetition rate.

The minimum timescale of processes that can be resolved with OPP depends on the $\sim 80\,\text{fs}$ pulse duration of the Mai Tai. This is sufficiently short to study fundamental carrier decay processes in a wide range of materials such as metals, insulators, semiconductors, and superconductors. It should be noted that in practice, ultrafast pulses are broadened after transmission through optics, due to the positive group velocity dispersion (GVD) experienced by pulses when travelling through dispersive media [**73**, **74**]. Ultrafast pulse broadening can be minimized by using reflective optics instead of transmissive ones where possible, using

dispersion-compensated mirrors, and by compensating pulse broadening by incorporating additional negative GVD components such as prism pairs into an optical system.

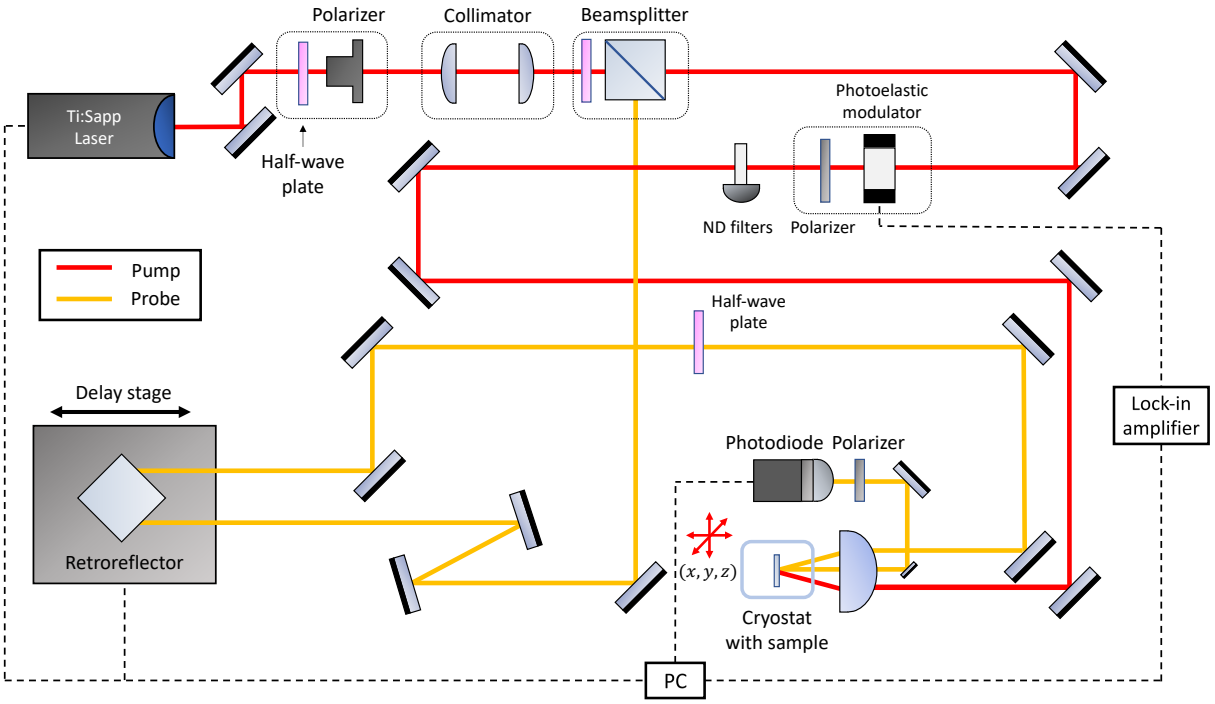

FIGURE 2.1. Ultrafast optical pump-probe apparatus at UC Davis, with the key components labeled. The pump and probe beam paths are shown as red and yellow, respectively.

2.3 Optical pump-probe experimental apparatus

Figure 2.1 shows the ultrafast OPP apparatus employed in this work. Laser pulses are generated using a mode-locked, Ti:Sapphire oscillator (Spectra Physics Mai Tai) with a minimum 80 fs pulse duration, which is optimized for sustained operation in energies around $E_{\text{ph}} = 1.55\,\text{eV}$. The time delay ($t_{\text{delay}}$) between the pump and probe pulses is controlled by a retroreflector mounted on a mechanical delay line in the optical path of the probe beam. To maintain a constant probe reflection R from the sample, the angle of incidence of the probe beam into the retroreflector is carefully tuned to maintain constant R through the

entire measured t_{delay} range. This is needed to avoid spurious R drift which may erroneously be interpreted as originating from ΔR. The pump and probe pulses are focused to a single spot at the sample surface with a plano-convex lens, and has a spot diameter of $d = 40\,\mu\text{m}$.

To calibrate the temporal overlap of the pump and probe pulses (i.e., "time-zero"), the pump and probe beams are focused onto a β-barium borate crystal (β-BBO), which uses second harmonic generation (SHG) to generate a third optical beam with double the input photon energy ($E_{\text{ph}} = 1.55\,\text{eV} \rightarrow E_{\text{ph}} = 3.1\,\text{eV}$) when the pump and probe beams are exactly temporally and spatially overlapped on the β-BBO crystal. Chapter 4 provides further explanation of the mechanism of SHG in β-BBO. After slowly scanning t_{delay} through the entire length of the delay stage, the third blue beam is visually confirmed at some point in the scan, and the delay stage is homed to this position to mark time-zero.

The probe reflection R from the sample is measured using a photodiode (Thorlabs PDA36A), and the pump-induced ΔR signal is obtained using standard lock-in detection (Stanford Research Systems SR-830) with the photodiode output as the lock-in input signal. The modulation of the pump beam is performed using a Hinds Instruments photoelastic modulator (PEM100) in combination with a linear film polarizer, which has the effect of chopping the pump with a frequency of $f = 100\,\text{kHz}$, and is used as the reference frequency of the lock-in. Typically, the pump and probe pulses are cross-polarized to minimize interference at the sample surface and to limit pump scatter incident on the photodiode.

Temperature-dependent experiments are performed by measuring the sample in an open-cycle optical cryostat (Janis ST-500) using liquid nitrogen ($T > 77\,\text{K}$) or liquid helium ($T > 4\,\text{K}$) to reach cryogenic temperatures, which are selected with a PID controller (Lakeshore 335) coupled to a heating element in the cryostat. The cryostat is mounted on an XYZ stage (Newport 462-XYZ-LH-M), which is used to position the sample at the focus of the pump and the probe beams, and to maximize the $\Delta R/R$ signal from the sample. This is especially useful for optimizing the position of small samples with rough or uneven surfaces. Prior

to each experiment, the probe reflection R from a large Bi_2Se_3 crystal is used to quickly optimize XY sample positioning. When time-zero is known, the maximum of the $\Delta R/R$ signal of Bi_2Se_3 is used to quickly confirm time-zero and to optimize sample Z-positioning at the focus of the beams.

The two main studies that can be done using this OPP apparatus are fluence- and temperature-dependent experiments. The pump fluence Φ is the deposited pump pulse energy per unit area ($\mu J\,cm^{-2}$), and different fluences can be selected with different neutral-density filters in the path of the pump beam. The fluence is calculated knowing the measured average pump power, the focused spot size ($d = 40\,\mu m$), and the repetition rate of the pulses ($f = 80\,MHz$). Often, the pump fluence is usually kept below $15\,\mu J\,cm^{-2}$ to minimize effects and damage from sample heating. Fluence-dependent experiments can relate changes in $\Delta R/R$ and τ, the carrier lifetime, to the number of excitations created by the pump pulse. As will be discussed in Chapter 3, fluence-dependent experiments can be used to infer particular processes occurring during carrier relaxation, such as the bimolecular recombination of carriers or the oscillatory decay of excited phonons. The use of temperature-control can also be used to access temperature-dependent phases in the measured material, in addition to reducing noise in the measurement at cryogenic temperatures.

Chapter 3

Nanosecond dynamics in the intrinsic topological insulator $Bi_{2-x}Sb_xSe_3$

3.1 Introduction

In this chapter, we first discuss using OPP to measure the ultrafast carrier dynamics in the 3D TI Bi_2Se_3. We then present observations of dramatically enhanced photoexcitation lifetimes in $Bi_{2-x}Sb_xSe_3$ nanoplatelets, and compare these observations to those seen in Bi_2Se_3. The increased carrier lifetimes only exists in bulk-insulating samples and exhibit fluence, temperature, and Sb-doping dependence distinct from the behavior in bulk-metallic Bi_2Se_3 [76]. The fluence-dependent decay rate is consistent with bimolecular recombination of electron-hole pairs in the TI bulk, and connections to evidence of exciton condensation are also discussed. This chapter was adapted from Ref. [76].

3.2 Optical pump-probe experiments on Bi_2Se_3

Here, the optical pump-probe apparatus described in Chapter 2 is employed to measure the OPP response in Bi_2Se_3, namely the transient reflectivity $\Delta R/R$. A photon energy of $E_{ph} = 1.55\,\text{eV}$ ($\lambda = 800\,\text{nm}$) was used, taking advantage of the high reflectivity of Bi_2Se_3 at this wavelength. Figure 3.1 shows room temperature OPP data on Bi_2Se_3. Prior to the

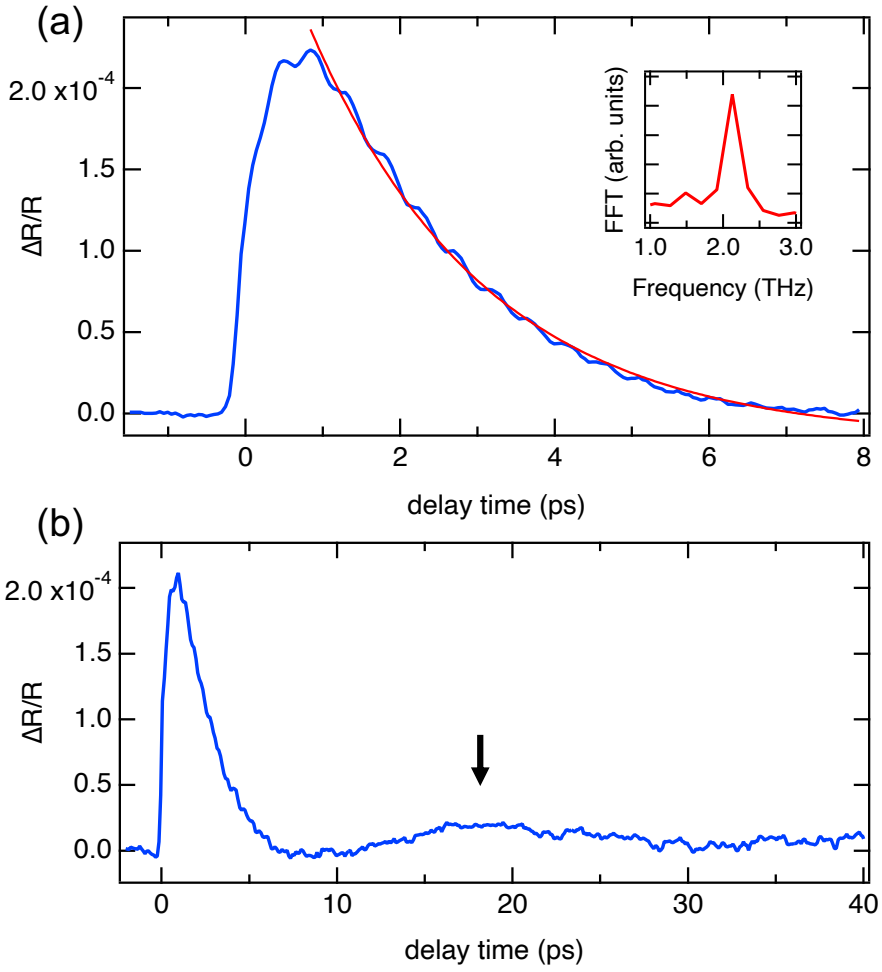

FIGURE 3.1. Optical pump-probe data on Bi_2Se_3 at room temperature. (a) Bi_2Se_3 $\Delta R/R$ decay plotted on a short $< 10\,\text{ps}$ timescale. Red curve is a single exponential fit to the decay ($Ae^{-t_{\text{delay}}/\tau} + B$). Inset shows fast Fourier transform (FFT) of the data after subtracting the overall exponential decay, showing the coherent optical phonon peak at 2.1 THz. The pump fluence is $\Phi = 95\,\mu\text{J}\,\text{cm}^{-2}$. (b) Bi_2Se_3 $\Delta R/R$ decay on a longer $< 50\,\text{ps}$ timescale. Notice the acoustic phonon oscillation peak near 18 ps, indicated by the black arrow. The pump fluence is $\Phi = 75\,\mu\text{J}\,\text{cm}^{-2}$.

pump pulse arriving at the Bi_2Se_3 sample, the $\Delta R/R$ signal is initially zero. Once the pulse arrives at the sample at $t_{\text{delay}} = 0\,\text{ps}$, $\Delta R/R$ increases until it reaches a maximum, as is shown in Fig. 3.1(a). Typically, the magnitude $\Delta R/R$ is usually small, in the range of

$10^{-7} - 10^{-4}$, and increases with increasing pump fluence. During the rise of $\Delta R/R$, initially unoccupied states become occupied after photoexcitation, after which they relax back to equilibrium. To obtain the time constant τ of the decay, a single exponential function $\Delta R(t_{\text{delay}})/R = Ae^{-t_{\text{delay}}/\tau} + B$ is fitted to the decay (red), which yields $\tau = 2.3\,\text{ps}$, the bulk carrier lifetime in Bi_2Se_3. The $\tau \sim 2\,\text{ps}$ lifetime is consistent with previous transient reflectivity measurements [60, 62, 77–79], as well as with transient THz conductivity work in thin films [80, 81].

During the decay, oscillations in $\Delta R/R$ are also observable. In Fig. 3.1(a), the fast oscillations are caused by an excited $A_{1g}^{(1)}$ coherent optical phonon mode, and higher fluences in the range of $\Phi = 95 - 75\,\mu\text{J}\,\text{cm}^{-2}$ are selected to best resolve the oscillations. The phonon mode is readily identified by subtracting the exponential component of the decay from the $\Delta R/R$ signal and by taking a Fourier transform of the result (inset). The center frequency is 2.1 THz, agreeing with prior pump-probe [60, 77] and Raman [82] values. The excitation of optical phonons in Bi_2Se_3 is explainable in the framework of the displacive excitation of coherent phonons (DECP) mechanism (see Ref. [83]). On longer timescales in Fig. 3.1(b), a large slower oscillation is also visible (arrow) and is consistent with the 60 GHz acoustic phonon mode that is also excited by the pump pulse [60, 62, 77], arising from the decay of coherent optical phonon modes [84]. Materials often show a plateau to constant $\Delta R/R$ at $\sim$ ns timescales. This plateau can arise from sample heating after the initial $\Delta R/R$ decay, which decays very slowly compared to photoexcited carriers.

From the point of view of OPP, undoped Bi_2Se_3 demonstrates bulk-metallic optical response. Due to the significant penetration depth of the probe pulses into Bi_2Se_3 ($\alpha \sim 24\,\text{nm}$ with $E_{\text{ph}} = 1.55\,\text{eV}$) [85] and the $\sim 1\,\text{nm}$ thickness of a quintuple layer, the probe reflection primarily samples the bulk. Thus OPP mainly measures the bulk carrier properties of TIs, with some detectable contributions from the surface. The initial decay of $\Delta R/R$ in

Bi_2Se_3 follows Allen's two-temperature model (TTM) framework for metals, where an out-of-equilibrium population of carriers with temperature T_e thermalizes with the lattice with temperature T_l by coupling to multiple phonon modes in the crystal lattice. [77, 78, 86–89]. In the TTM, the electron-phonon interaction (i.e., the exchange of energy between the carriers and the lattice) mediates the system return to equilibrium. This process is described by the differential equation [86]:

$$\frac{dT_e}{dt} = \gamma_T(T_L - T_e), \text{ with } \gamma_T = \frac{3\hbar\lambda\langle\omega^2\rangle}{\pi k_B T}. \tag{3.1}$$

Here, T_e and T_l are the electronic and lattice temperatures, respectively, with the thermal relaxation rate γ_T. Upon photoexcitation, T_e initially increases with only a very small initial change in T_l, which arises from instantaneous sample heating. Within the 2 ps carrier decay window, T_e decreases while T_l increases, after which the overall temperature decreases until the system returns to thermal equilibrium when $\Delta R/R = 0$. In the TTM, γ_T can be further related to the electron-phonon coupling constant λ and the second moment of the phonon spectrum $\langle\omega^2\rangle$. Therefore, for materials with higher electron-phonon coupling λ, the rate at which carriers decay measured in an OPP experiment is higher.

3.3 Optical pump-probe experiments on $Bi_{2-x}Sb_xSe_3$

Much of the previous work on bulk-insulating TIs centers on the $Bi_{2-x}Sb_xTe_3$ (BST) or $Bi_{2-x}Sb_xTe_{3-y}Se_y$ (BSTS) family of materials [19, 90, 91] based on Bi_2Te_3, but comparatively fewer studies exist on bulk-insulating TIs based on Bi_2Se_3, such as $Bi_{2-x}Sb_xSe_3$ [92]. Bulk-insulating Bi_2Se_3 can sometimes manifest optoelectronic phenomena uniquely or more robustly than in pure Bi_2Se_3 [25, 93], and can also be expected to result in different bulk dynamics of optically excited carriers, which heretofore have not been characterized in bulk-insulating Bi_2Se_3-based TIs.

Tuning the chemical potential so that it lies within the bulk band gap is needed for making Bi_2Se_3 bulk-insulating, rather than bulk-metallic from the selenium vacancies present.

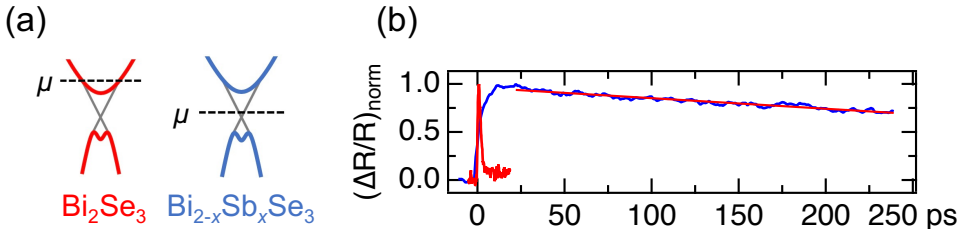

FIGURE 3.2. Comparison of optical pump-probe response in Bi_2Se_3 and $Bi_{2-x}Sb_xSe_3$ at 7 K, with a pump fluence of $\Phi = 7.4\,\mu J\,cm^{-2}$. (a) Cartoon of the chemical potential position μ relative to the bulk conduction and valence bands, showing the topological surfaces states (gray). (b) $\Delta R/R$ traces, showing the long decay for $Bi_{2-x}Sb_xSe_3$ that persists outside of the 250 ps measurement window. The traces were normalized to their respective maxima.

To accomplish this, $Bi_{2-x}Sb_xSe_3$ can be synthesized by substituting Bi with Sb, with the magnitude of the chemical potential shift given by the fraction of doped Sb. Sb-doping on the Bi site is isovalent, and thus does not introduce charge carriers directly. Instead, Sb addition changes the lattice constant of Bi_2Se_3, which results in a smaller unit cell which is thought to diminish the number of selenium vacancies in the studied doping range [**92**, **94**]. A schematic of the chemical potential shift from Sb-doping is shown in Fig. 3.2(a).

The $Bi_{2-x}Sb_xSe_3$ nanoplatelets were grown by chemical vapor deposition and the Bi_2Se_3 nanoplatelets were synthesized from the same precursors. Typical nanoplatelet dimensions are $150 \times 150 \times 0.1\,\mu m^3$. The ~ 100 nm thickness of the specimens is well outside the regime where hybridization between opposite surfaces leads to the opening of a gap at the Dirac point [**95**, **96**]. Sb composition ranges from $x = 0.22 - 0.34$ for the $Bi_{2-x}Sb_xSe_3$ samples, determined with energy-dispersive X-ray spectroscopy (EDS), which also correlates with carrier density [**94**]. After synthesis, the nanoplatelets are transferred by Kapton-tape onto a Si substrate covered with 300 nm-thick SiO_2. No signal from the bare substrate is observed for the fluences used in these experiments.

Fig. 3.2(b) shows a comparison of $\Delta R/R$ traces in $Bi_{2-x}Sb_xSe_3$ (blue, $x = 0.25$) and undoped Bi_2Se_3 (red, $x = 0$) at $T = 7$ K. In bulk-insulating $Bi_{2-x}Sb_xSe_3$, the carrier

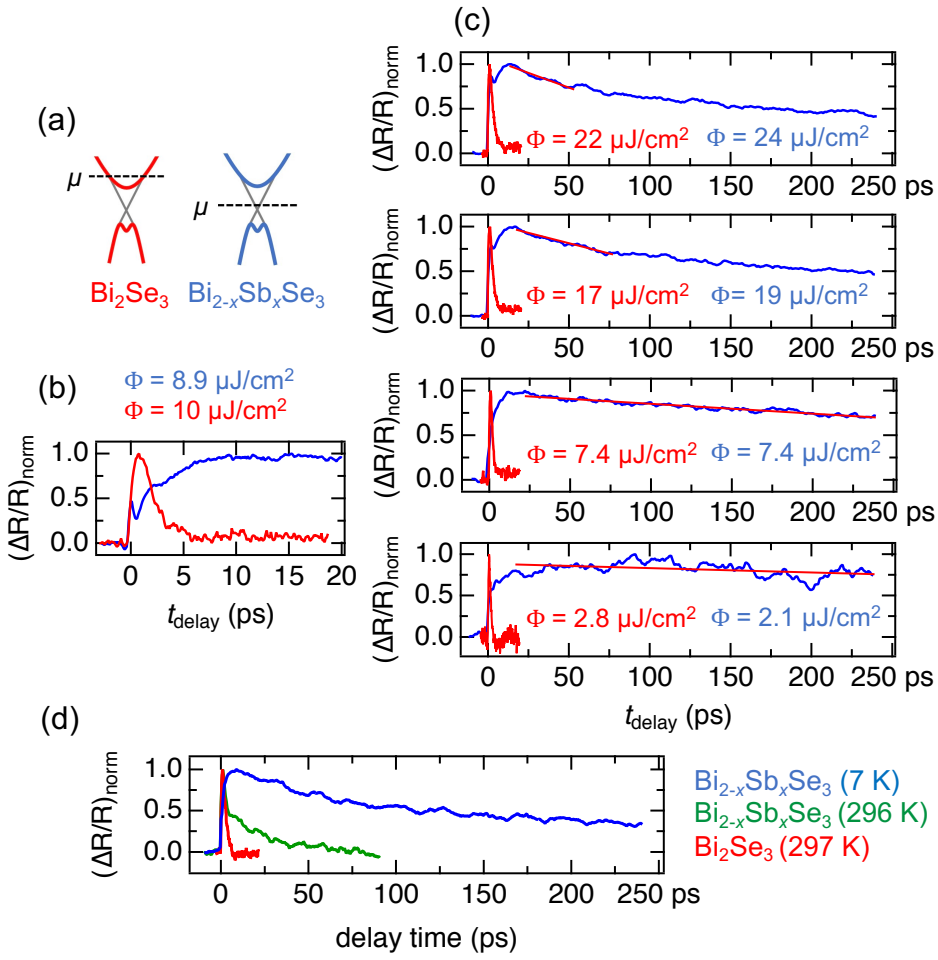

FIGURE 3.3. Effect of doping on relaxation dynamics at various fluences for Bi_2Se_3 (red) and $Bi_{2-x}Sb_xSe_3$ (blue) samples. (a) Band diagrams of Bi_2Se_3 and $Bi_{2-x}Sb_xSe_3$, with μ denoting the schematic position of the chemical potential. (b) Example short delay time $\Delta R/R$ traces at $T = 7\,\mathrm{K}$, normalized to their respective peak values. (c) Longer delay time traces with the same samples as in panel (b) at selected pump fluences at $T = 7\,\mathrm{K}$. The red lines overlaying the blue traces show linear fits to the decays for $(\Delta R/R)_{\mathrm{norm}} > 0.7$. (d) $(\Delta R/R)_{\mathrm{norm}}$ traces for a different $Bi_{2-x}Sb_xSe_3$ sample at 7 K (blue) and 296 K (green), with Bi_2Se_3 at 297 K (red) shown for comparison.

dynamics are pronouncedly different. Instead of a quick 2 ps decay, carriers in $Bi_{2-x}Sb_xSe_3$ can persist on the order of hundreds of ps, or several ns at the lowest usable fluences. Due to the bulk-insulating carrier dynamics in $Bi_{2-x}Sb_xSe_3$, the TTM is not applicable and suggest a slower recombination of electron-hole pairs across the bulk gap.

Figure 3.3 shows the normalized transient reflectivity traces for bulk-metallic Bi_2Se_3 (red, $x = 0$) and bulk-insulating $Bi_{2-x}Sb_xSe_3$ nanoplatelets (blue, $x = 0.25$) at 7 K for several different fluences. Upon reaching its peak, the Bi_2Se_3 transient reflectivity traces decay to equilibrium with the typical $\tau \sim 2$ ps. In contrast, the $Bi_{2-x}Sb_xSe_3$ traces in Fig. 3.3(c) show much longer-lived excitations with 90% of the reflectivity surviving near the edge of the measurement window at the lowest fluence ($\Phi = 2.1\,\mu J\,cm^{-2}$). The transient reflectivity of the $Bi_{2-x}Sb_xSe_3$ samples has a pronounced fluence dependence, which can be seen in the data in Fig. 3.3 by observing the magnitude of $(\Delta R/R)_{norm}$ near 250 ps. Relaxation becomes faster at higher temperature, but even at room temperature $Bi_{2-x}Sb_xSe_3$ shows longer-lived excitations than Bi_2Se_3 (Fig. 3.3(d), green). More details on the $\Delta R/R$ signal structure are given below.

3.4 Short and long time $\Delta R/R$ signal structure

There is some complicated structure in the $\Delta R/R$ traces at short delay times, namely the delayed onset in the $Bi_{2-x}Sb_xSe_3$ trace around $t_{delay} \sim 0.5$ ps and the kink preceding the peak of the Bi_2Se_3 trace in Fig. 3.4 (left). These features have been observed in earlier transient reflectivity studies on Bi_2Se_3 [**61**, **77**] and attributed to a negative amplitude component arising from the trapping of electrons by Se vacancies [**77**]. In our work, we can safely ignore the early structure because our primary focus is on the long-lived component to the decay for $t_{delay} \gg 0.5$ ps, when any negative transients are expected to die out.

At longer time delays, there are also long-lived $f \sim 40$ GHz oscillations in the $Bi_{2-x}Sb_xSe_3$ traces, which can most clearly been seen in Fig. 3.4 (right). These oscillations are attributable to acoustic phonon oscillations [**60**, **62**, **77**], and can only be resolved at higher pump fluences ($\Phi > 10\,\mu J\,cm^{-2}$).

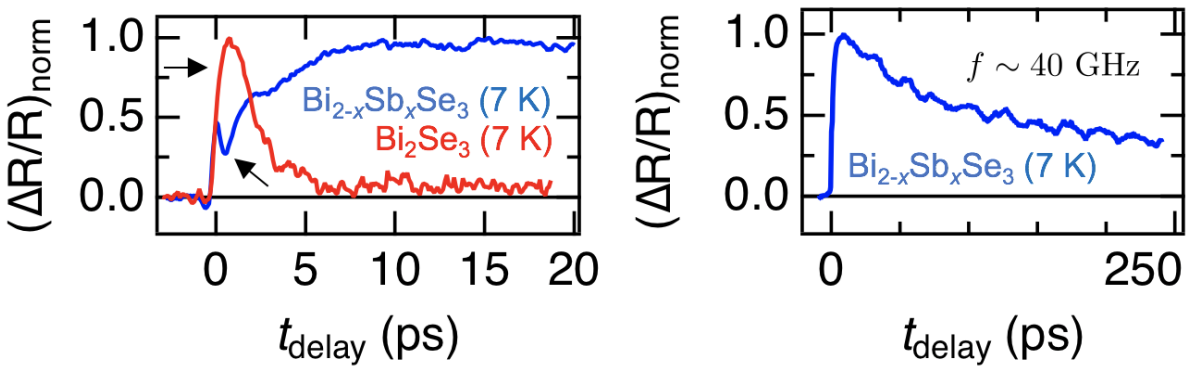

FIGURE 3.4. Additional features in $Bi_{2-x}Sb_xSe_3$ OPP traces. Left: Short delay time traces showing the negative component and kink in $Bi_{2-x}Sb_xSe_3$. Right: Long delay time trace showing acoustic phonon oscillations in $Bi_{2-x}Sb_xSe_3$.

3.5 Pump fluence dependence and bimolecular recombination

Figure 3.5 quantifies the fluence dependences for $Bi_{2-x}Sb_xSe_3$ and Bi_2Se_3 at 7 K. For $Bi_{2-x}Sb_xSe_3$ at lower fluences, we quantify the decay rate using linear fits to the normalized traces over intervals where the decay is linear in time (red lines in Fig. 3.3(c)). The decay rates γ from these fits are plotted in Fig. 3.5(a) as a function of fluence for $Bi_{2-x}Sb_xSe_3$. This model-independent fitting shows that the decay rates become slower as the number of excitations, as parametrized by the fluence, is reduced, and suggests a linear relationship between the two. This linear relationship is characteristic of a bimolecular recombination process. Extrapolating to the zero fluence limit, the $Bi_{2-x}Sb_xSe_3$ samples yield a decay rate of $\gamma(\Phi \to 0) \sim 0.30\,\mathrm{ns}^{-1}$, or a decay time of 3.3 ns, substantially slower than in metallic Bi_2Se_3.

In contrast, the decay rates, derived from single-exponential fits, for Bi_2Se_3 in Fig. 3.5(b) show fluence dependence *opposite* of that of $Bi_{2-x}Sb_xSe_3$. Data on n-type Bi_2Se_3 samples show a plateau at sufficiently long delay times (> 10 ps), which increases with fluence, demonstrating steady state heating [60]. This plateau reaches $< 10\%$ of the maximum

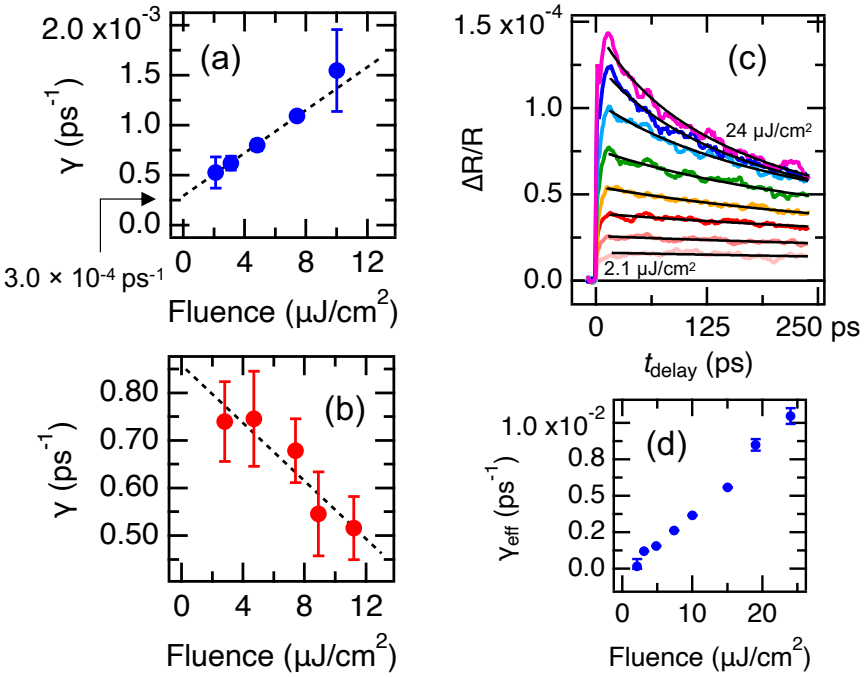

FIGURE 3.5. Pump fluence dependence at 7 K in $Bi_{2-x}Sb_xSe_3$ and Bi_2Se_3. (a) Decay rates γ for $Bi_{2-x}Sb_xSe_3$ from linear fits of $(\Delta R/R)_{\text{norm}}$ vs t_{delay}. Dashed line: linear fit to γ vs. fluence. (b) Decay rates for Bi_2Se_3 from single exponential fits as a function of fluence. (c) $Bi_{2-x}Sb_xSe_3$ traces at different fluences, overlaid by fits to Eq. 3.2 (black). (d) Extracted bimolecular decay rates γ_{eff} from the fits to Eq. 3.2.

$\Delta R/R$ for $\Phi < 22\,\mu\text{J}\,\text{cm}^{-2}$, indicating minimal steady state heating in the fluence regime where our analysis of insulating samples is performed.

Following these model-independent observations, we now turn to a fitting scheme which specifically assumes bimolecular recombination (i.e., electron-hole recombination across the bulk band gap) to describe the decay dynamics in $Bi_{2-x}Sb_xSe_3$ [54, 56, 57]. This fitting also includes the effects of the exponential decay of the pump and probe pulses in the sample, which implies the generation of a nonuniform $\propto n_0 e^{-\alpha z}$ excitation density. This is accounted for with the following function for the transient reflectivity [54]:

$$\frac{\Delta R(t)}{R} = \frac{\Delta R(0)}{\gamma_{\text{eff}} t}\left[1 - \frac{\ln(1+\gamma_{\text{eff}} t)}{\gamma_{\text{eff}} t}\right]. \tag{3.2}$$

The fitting parameters are $\Delta R(0)$ and γ_{eff}, the initial reflectivity change and the effective decay rate for the bimolecular process. Here, the decay rate is defined as $|\gamma_{\text{eff}}| \equiv \beta n$, with a quasiparticle density n and the coefficient for the bimolecular process β. By accounting for the depth-dependent fluence, we can extend the applicability of the bimolecular recombination model to higher fluences. These traces and their fits to Eq. 3.2 are plotted in Fig. 3.5(c), and the extracted fluence-dependent rates γ_{eff} are plotted in Fig. 3.5(d).

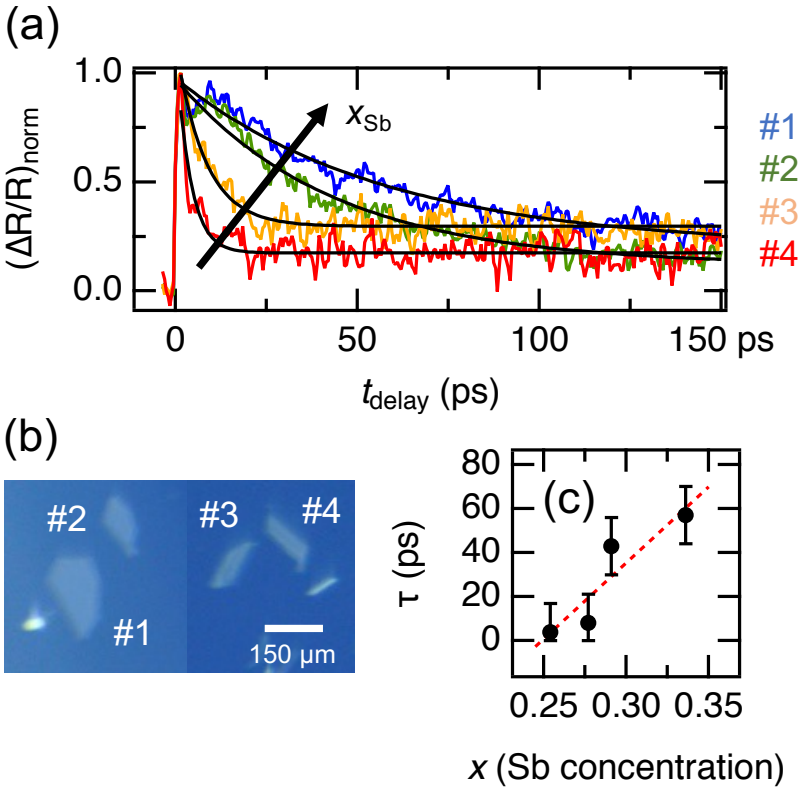

FIGURE 3.6. Doping dependence of relaxation dynamics in $Bi_{2-x}Sb_xSe_3$. (a) $(\Delta R/R)_{\text{norm}}$ traces at $T = 7\,\text{K}$ and $\Phi = 10\,\mu\text{J}\,\text{cm}^{-2}$, with increasing Sb concentration denoted by arrow. (b) Corresponding sample images. (c) Extracted time constants from $(\Delta R(t_{\text{delay}})/R)_{\text{norm}} = Ae^{-t_{\text{delay}}/\tau} + B$ fits.

Fig. 3.6(a) shows the variation in the $\Delta R/R$ traces as a function of Sb-doping, measured with the same pump fluence. The specimens in this figure are different nanoplatelets from a single growth. The traces are fitted to single exponentials to quantify decay times

$(\Delta R(t_{\text{delay}})/R)_{\text{norm}} = Ae^{-t_{\text{delay}}/\tau} + B$. The time constants from the fits are plotted in Fig. 3.6(c) as a function of x, the Sb concentration in $Bi_{2-x}Sb_xSe_3$. As x increases, the carrier lifetime monotonically increases.

3.6 Discussion

We begin by discussing bulk-metallic Bi_2Se_3. The initial decay of $\Delta R/R$ in Bi_2Se_3 follows the framework of the two-temperature model for metals, where an out-of-equilibrium population of carriers with temperature T_e thermalizes with the lattice with temperature T_l by coupling to multiple phonon modes [**77**, **78**, **86**–**89**]. The fast initial bulk carrier decay in Bi_2Se_3 is consistent with previous transient reflectivity measurements [**60**, **62**, **77**–**79**] as well with transient THz conductivity work in thin films [**80**, **81**]. Thus, we can generalize the response of our Bi_2Se_3 samples as that of a typical metal. As noted earlier, the rates γ for Bi_2Se_3 in Fig. 3.5(b) follow an opposite fluence dependence from the insulating samples, which underlines the importance of tuning the chemical potential for influencing TI response to optical excitation.

We now turn to bulk-insulating $Bi_{2-x}Sb_xSe_3$. As with metallic Bi_2Se_3, photoexcitation at t_{delay}= 0 ps causes electrons from within the bulk valence band to populate bulk states far above E_F, but unlike the n-type system, electrons relax to the edge of the bulk conduction band which is minimally occupied at low temperature. This rapid initial 1-5 ps thermalization has been verified by time-resolved ARPES (trARPES) [**89**,**97**–**101**], and thus the optical pump has the effect of an indirect injection of gap-energy excitations. The observed linear fluence dependence of the decay rate in $Bi_{2-x}Sb_xSe_3$ is consistent with bimolecular recombination, where photoexcited electron-hole pairs of density n recombine and follow the simple rate equation $\frac{dn}{dt} = -\beta n^2$, which can be integrated to yield a decaying quasiparticle density $n(t) = \frac{n_0}{1+n_0\beta t}$ [**54**, **56**, **57**]. The effective decay rate γ_{eff} then takes the form $\gamma \equiv \frac{1}{n}\frac{dn}{dt} = -\beta n$, where β is the bimolecular coefficient. The linear fluence dependences in Figs. 3.5(a,d) are characteristic of bimolecular recombination, indicating that recombination of electron-hole

pairs dominates decay of bulk excitations in $Bi_{2-x}Sb_xSe_3$. This recombination is assumed to be radiative because the band gap of Bi_2Se_3 ($E_g \sim 0.3\,eV$) is much higher than the highest phonon energy ($E = 23\,meV$) in the material [62, 102].

3.7 Prior pump-probe works

For greater context, a summary of time-resolved optical, mid-IR, and THz studies that have reported bulk photoexcited carrier lifetimes in Bi_2Se_3-related compounds [60–62, 77–81, 91, 103] is shown below. A selection of these works are listed in Table I, alongside the relevant experimental conditions, carrier relaxation time, and the fluence-dependence of the carrier decay rate γ (or scattering rate for the THz studies). This table focuses on optical, mid-IR, and THz measurements in order to compare bulk sensitive measurements to one another.

Reference	**Pump, Probe**	**Material**	**Temperature**	**Relaxation time**	**Pump fluence**	**Fluence dependence**
Present study	Optical, Optical	$Bi_{2-x}Sb_xSe_3$ (insulating), Bi_2Se_3 (n-type)	7 K, Room T	~ 3 ns (insulating) ~ 2 ps (n-type)	2 - 11 $\mu J\,cm^{-2}$	γ inc. with inc. fluence (insulating), γ dec. with inc. fluence (n-type)
J. Qi et al. (2010) [77]	Optical, Optical	Bi_2Se_3 (n-type)	Room T	~ 2 ps	2.5 $\mu J\,cm^{-2}$	N/A
N. Kumar et al. (2011) [60]	Optical, Optical	Bi_2Se_3 (n-type)	Room T	~ 2 ps	0.6 - 50 $\mu J\,cm^{-2}$	Weak/no fluence dependence
C. W. Luo et al. (2013) [103]	Optical, MIR	Bi_2Se_3 (n-type)	Room T	1.5 - 90 ps	3 - 105 $\mu J\,cm^{-2}$	N/A
Y.-P. Lai at al. (2014) [78]	Optical, Optical	Bi_2Se_3 (n-type)	11 K - 295 K	~ 2 ps	37 $\mu J\,cm^{-2}$	N/A

Continued on next page

TABLE I – *Continued from previous page*

Reference	**Pump, Probe**	**Material**	**Temperature**	**Relaxation time**	**Pump fluence**	**Fluence dependence**
L. Cheng et al. (2014) [61]	Optical, Optical	BSTS (insulating)	10 K - 300 K	~ 2 ps	1 - 10 μJ cm^{-2}	γ dec. with inc. fluence (300 K)
S. Sim et al. (2014) [80]	Optical, THz	Bi_2Se_3 thin films (n-type)	10 K - 230 K	~ 10 ps	10 - 90 μJ cm^{-2}	γ inc. with inc. fluence
Y. D. Glinka et al. (2015) [62]	Optical, Optical	Bi_2Se_3 thin films (n-type)	Room T	~ 2 ps	N/A	N/A
Y. Onishi et al. (2015) [91]	MIR, MIR	BSTS (insulating)	300 K	~ 3 - 10 ps	~ 30 μJ cm^{-2}	None
R. Valdés Aguilar et al. (2015) [81]	Optical, THz	Bi_2Se_3 thin films (n-type)	10 K	5 - 10 ps	3 - 200 μJ cm^{-2}	γ inc. with inc. fluence (only in $>$ 16 QL films)
G. Jnawali et al. (2018) [79]	Optical, MIR	Bi_2Se_3 films (n-type)	10 K, 300 K	<5 ps (fast) ~ 600 ps (long)	~ 1 mJ cm^{-2}	N/A

ARPES studies are excluded from this table because they are more surface sensitive, and these works are cited and discussed elsewhere. The list is not meant to be fully comprehensive, but rather to contextualize our findings within the broader landscape of works. Our measured long bulk carrier lifetimes in insulating samples, combined with the observed novel fluence dependence, distinguishes our study from these works.

Notably, neither long bulk carrier lifetimes in excess of 1 ns nor a fluence-dependence characteristic of bimolecular recombination has been reported simultaneously in those prior studies. Thus, our measured long bulk carrier lifetimes in insulating samples, combined with the observed strongly fluence-dependent carrier recombination, points to a distinct interpretation of bulk recombination dynamics in insulating 3D TIs.

TrARPES studies have reported long-lived carriers arising from bulk excitations relaxing through the metallic surface states or from surface photovoltage (SPV) in 3D TIs [**98**–**101**, **104**–**106**]. While the former may be the dominant relaxation mechanism near the surface,

it cannot produce the strong fluence dependence we observe for $Bi_{2-x}Sb_xSe_3$. The surface state has a limited density of states near the Dirac point which restricts faster relaxation with higher excitation-density. We note that the decay of SPV has the opposite fluence dependence from our results in Fig. 3.5(a) [**106**].

Additionally, the bulk decay dynamics of $Bi_{2-x}Sb_xSe_3$ are highly doping-dependent, as illustrated by the traces in Figure 3.6, which may be interpreted either in terms of a changing free carrier density or doping inhomogeneity. In this doping regime, the free carrier density decreases monotonically with increasing Sb concentration x [**92**]. These carriers are primarily thermally excited electrons in the conduction band, and thus lower values of x correspond to more recombination opportunities for photoexcited holes. Thus, the observed doping dependence is consistent with a bimolecular recombination model.

Another relevant aspect is possible distributions of local dopings, primarily due to varying Se vacancy density, which has been described in similar nanoplatelets [**107**,**108**]. In samples closer to the n-type regime (smaller x), small local deviations from the average doping are more likely to correspond to local metallicity. As shown earlier, metallic and insulating Bi_2Se_3 yield profoundly different decay dynamics, and an increased probability of locally higher carrier density may promote behavior more like the former. We note some variation between different growths, which presumably arises from precursor variability in the CVD synthesis process, and the sample in Fig. 3.3 was from a different growth.

A summary of relaxation and migration processes in the bulk and surface regions in $Bi_{2-x}Sb_xSe_3$ is shown in Figure 3.7, combining our results with those from literature. The pump initially generates electron-hole pairs in the bulk and surface regions of the material, which can subsequently undergo several processes during the decay to equilibrium. The first process for bulk carriers is bimolecular recombination across the bulk band gap. Near the band edge, bulk carriers recombine and release energy radiatively. The long nanosecond lifetime of this process allows time for other processes, such as photo-thermoelectric effects

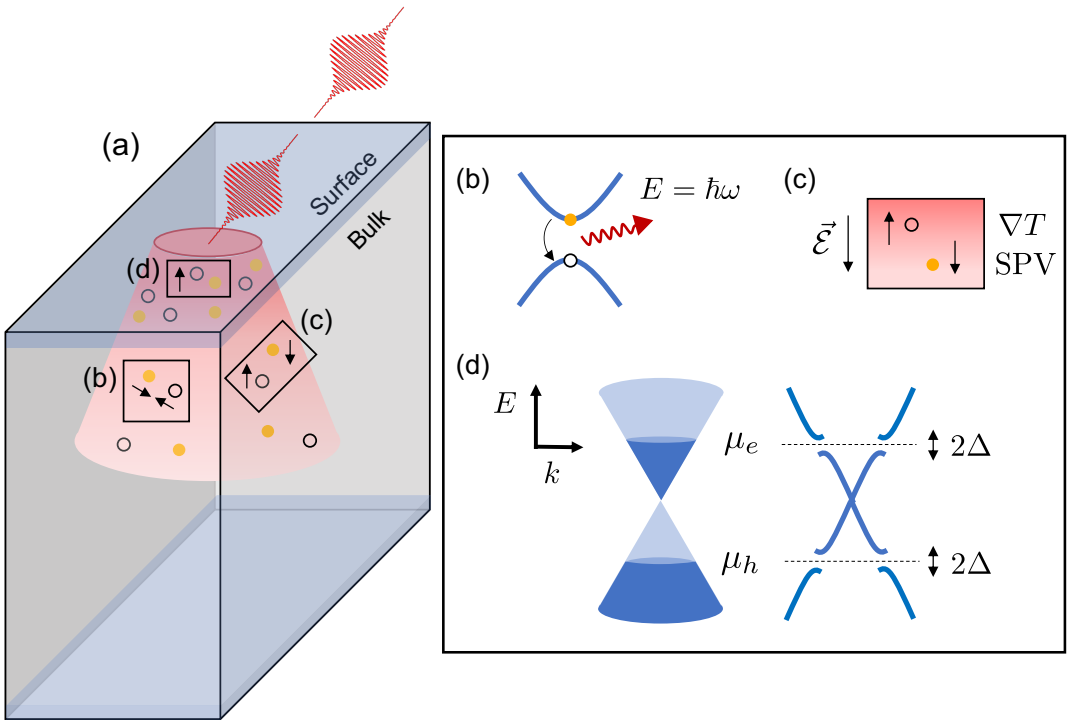

FIGURE 3.7. Schematic of carrier decay processes for $Bi_{2-x}Sb_xSe_3$. (a) Optical excitation generates electron-hole pairs in the bulk and surface of the TI. (b) Radiative, bimolecular recombination of electrons and holes. (c) Carrier migration due to a temperature gradient ∇T and surface photovoltage (SPV). (d) Long-lived carriers in surface Dirac state form different chemical potentials for electrons and holes (μ_e, μ_h) (left) where excitonic gaps (2Δ) can open (right).

and SPV to assist remaining carriers in migrating towards the surface [25, 105, 109, 110]. In both cases, either a temperature gradient [99] or a photodoping gradient produces an internal voltage that can sweep carriers from the deep bulk towards the surface (Fig. 3.7(c)). When carriers ultimately relax, they slowly recombine and return to equilibrium after $t_{\text{delay}} > 3\,\text{ns}$, well outside our measurement window.

Near the surface, we revisit trARPES measurements for completeness. These measurements showed that bulk carriers at the surface slowly relax through the surface state (Fig. 3.7(d), left) often establishing a long-lived carrier population at the surface [98–101, 104].

Importantly, these long-lived surface excitations are only observed in bulk-insulating or p-type samples (e.g., lifetimes exceeding 400 ps in $(Sb_{1-x}Bi_x)_2Te_3$ [100] and in Mg-doped Bi_2Se_3 [106]). Our transient reflectivity experiments contribute nuance to this picture by illustrating the behavior of bulk carriers away from the surface, which are excited at the same time and can populate the surface state at later times because they are even more long-lived.

3.8 Exciton condensation in $Bi_{2-x}Sb_xSe_3$

Excitons are bound electron-hole pairs found in semiconductors and insulators, bonded together by the Coulomb interaction: $E_C = \frac{1}{4\pi\epsilon_0\epsilon_r}\frac{e}{r^2}$. In response to optical excitation, excitons can be generated and persist for extended times in semiconductors, and OPP techniques are commonly used to measure the exciton lifetime in these materials. However, there are certain conditions where individual excitons are favored to condense into a collective ground state of excitons, exhibiting behavior known as exciton condensation. To form an exciton condensate, the thermal de Broglie wavelength λ_{dB} of the excitons must exceed the inter-exciton separation d to form a sufficiently dense phase,

$$\lambda_{dB} = \frac{h}{p_{dB}} = \frac{h}{\sqrt{2mk_BT}} > d. \tag{3.3}$$

Exciton condensation has been previously observed in GaAs/AlGaAs quantum wells [111], quantum hall bilayers [112], interband 1T-$TiSe_2$ [113], and $MoSe_2/WSe_2$ bilayers [114]. In these systems, the confined dimensionality of the 2D material geometry is able to sufficiently increase the exciton density, and as is seen in Eq. 3.3, exciton condensation is far likelier to be observed at cryogenic temperatures. Recently, ARPES evidence for a transient exciton condensate state in Bi_2Te_3 has also been been reported [115].

In the current situation for $Bi_{2-x}Sb_xSe_3$, a transient, nonequilibirum population of bulk excitons is formed. The decay bottleneck near the surface allows electrons and holes to

develop separate chemical potentials (μ_e, μ_h) (Fig. 3.7(d), left) relevant for exciton condensation [16, 25, 115–122]. Dirac materials, including 3D TIs, are predicted to allow the formation of an exciton condensate, a Bardeen-Cooper-Schrieffer-like ground state of bound electron-hole pairs at the TI surface with gating or optical excitation [16, 122]. Key spectroscopic signatures of this state are excitonic gaps 2Δ that form in the surface states at the chemical potentials μ_e, μ_h (Fig. 3.7(d), right) [122, 123]. These gaps have an estimated magnitude up to $\sim 1-3$ meV. Bimolecular recombination of carriers across these excitonic gaps would also produce the presently observed fluence dependence, and ultrafast optics is sensitive to recombination across meV-scale gaps with an eV-scale probe as discussed in Chapter 2 [54–59, 68]. However, as discussed earlier in this chapter, it is likely that our signal is dominated by the bulk.

Lastly, a complementary study on the same samples reported highly non-local, millimeter-long surface photocurrents in bulk-insulating $Bi_{2-x}Sb_xSe_3$ after optical excitation [25], which have been interpreted in terms of exciton condensation. Tuning the chemical potential into the bulk gap is necessary for observing long relaxation times as it is for observing long decay lengths [25, 26]. Photocurrent decay lengths in $Bi_{2-x}Sb_xSe_3$ are maximized at low temperature ($T < 40\,\mathrm{K}$) and low fluence, precisely the regime where we observe the longest relaxation times. Importantly, our long $\tau > 3\,\mathrm{ns}$ lifetime, observed in the fluence regime relevant to potential exciton condensation, is incompatible with millimeter-long diffusive carrier travel, which would imply a carrier mobility of $\mu > 10^5\ \mathrm{m^2/V \cdot s}$, much higher than the highest measured values $\mu \sim 1\ \mathrm{m^2/V \cdot s}$ in Bi_2Se_3 [124, 125].

3.9 Summary

In summary, our transient reflectivity results show a three orders-of-magnitude slowing of the carrier decay rate $\gamma \to 0.30\,\mathrm{ns^{-1}}$ in the zero pump-fluence limit in photoexcited $Bi_{2-x}Sb_xSe_3$ at $T = 7\,\mathrm{K}$, as compared to n-type specimens. Our fluence-dependent data reveal a distinct process to consider in bulk-insulating TIs: bimolecular recombination of

bulk carriers after optical excitation. We additionally show the key role chemical potential position plays in both establishing long bulk carrier decay in bulk-insulating samples and in influencing carrier recombination rates. These findings underscore the role optically excited bulk carriers play in TIs prior to migrating to the surface, relevant for interpreting optoelectronic phenomena of surface states.

Chapter 4

Angle-resolved photoemission spectroscopy

4.1 Introduction

Angle-resolved photoemission spectroscopy (ARPES) is an experimental technique that measures the band structure of electrons and electron interactions in solid state materials. In this chapter, we describe the basics of the technique, focusing on the aspects of the technique that are useful for interpreting the band structures of Bi_2Se_3 and other materials of interest. The works where ARPES was used include studies on $Bi_{2-x}Sb_xSe_3$ (Refs. [25, 76]), a combined ARPES/AP-XPS study on $Cu_xBi_2Se_3$ (Ref. [126]), and ARPES measurements on the magnetic Weyl semimetal $Co_3Sn_2S_2$ (Ref. [127]). Additionally, we describe the construction and interfacing of a custom laser light source with ARPES, and describe spectra taken on Bi_2Se_3 using this light source.

The physical principle that ARPES is based on is the photoelectric effect, which relates the emitted electron kinetic energy E_{kin} to the photon energy ($E_{\text{ph}} = h\nu$) of the incident light, the electron atomic binding energy E_B, and the material work function ϕ:

$$E_{\text{kin}} = h\nu - E_B - \phi \tag{4.1}$$

$$\hbar\mathbf{k}_{||} = \sqrt{2mE_{\text{kin}}}\sin(\theta) \tag{4.2}$$

The first formula (Eq. 4.1) is a direct consequence of the conservation of energy in the photoemission process. The second formula (Eq. 4.2) is the in-plane crystal momentum of the electrons ($\mathbf{k}_{||} = k_x\hat{\mathbf{x}} + k_y\hat{\mathbf{y}}$), which is related to the ARPES electron emission angle θ from the sample surface normal, and is a consequence of applying the conservation of momentum to the ejected electrons.

One can also relate the full crystal momentum to the polar coordinate system (θ, ϕ) in an ARPES experiment. The description of the three Cartesian components of $\mathbf{k}$ is:

$$k_x = \frac{1}{\hbar}\sqrt{2mE_{\text{kin}}}\sin(\theta)\cos(\phi) \tag{4.3}$$

$$k_y = \frac{1}{\hbar}\sqrt{2mE_{\text{kin}}}\sin(\theta)\sin(\phi) \tag{4.4}$$

$$k_z = \frac{1}{\hbar}\sqrt{2mE_{\text{kin}}}\cos(\theta) \tag{4.5}$$

where $\mathbf{k} = k_x\hat{\mathbf{x}} + k_y\hat{\mathbf{y}} + k_z\hat{\mathbf{z}}$, and k_z is the perpendicular (out-of-plane) component of the crystal momentum ($\mathbf{k}_{\perp} = k_z\hat{\mathbf{z}}$) [8,128,129]. Simultaneous measurement of E_{kin} and $\mathbf{k}$ yields the electronic band structure (i.e., the energy-momentum relation of electrons in the crystal).

In ARPES, electrons are usually detected using a hemispherical analyzer, which is in essence a hemispherical capacitor that accepts photoelectrons of a selected pass energy (i.e., the electron E_{kin} that the analyzer accepts) and directs them to a detector. To measure electrons of different E_{kin}, the voltages of the electrostatic lenses that retard the electrons to a given pass energy are varied during spectrum acquisition. The analyzer measures electron intensities as a function of kinetic energy and emission angle (θ, E_{kin}) to yield an ARPES spectrum, which can be ultimately converted to a band structure $(\mathbf{k}_{||}, E_B)$ in post-processing.

The measured photoemission intensity I can be described as the product of several factors dependent on the electron momentum $\mathbf{k}$ and energy ω inside the material:

$$I(\mathbf{k},\omega) = I_0(\mathbf{k}, h\nu, \mathbf{A}) f(\omega) A(\mathbf{k},\omega). \tag{4.6}$$

Here, the main term is the single-particle spectral function $A(\mathbf{k},\omega)$. The Fermi-Dirac distribution $f(\omega)$ describes the cutoff above the Fermi energy E_F, and restricts standard ARPES experiments to measuring occupied states. Matrix element effects in I_0 arise from varying photon energy, polarization dependence of the light source, and the geometry of the experiment, which also affects the final measured intensities. In ARPES experiments such as the ones described in this work, the single-particle spectral function is the main quantity of interest. The spectral function can be related to the electron self-energy $\Sigma(\mathbf{k},\omega) = \Sigma'(\mathbf{k},\omega) + i\Sigma''(\mathbf{k},\omega)$, and written as [8]:

$$A(\mathbf{k},\omega) = -\frac{1}{\pi} \frac{\Sigma''(\mathbf{k},\omega)}{[\omega - \epsilon_{\mathbf{k}} - \Sigma'(\mathbf{k},\omega)]^2 + [\Sigma''(\mathbf{k},\omega)]^2}. \tag{4.7}$$

Here, the electron band energy $\epsilon_{\mathbf{k}}$ is offset by Σ' and the linewidth is broadened by Σ'', the real and imaginary components of the electron self-energy, respectively. Thus, the spectral function is sensitive to *both* electron band structure and electron interactions [8, 128, 129].

Photon energies in the VUV range are most suitable for resolving the valence bands near E_F because they permit the highest energy and momentum resolution of the electronic band structure, at the cost of being less bulk sensitive [130]. Photoemission spectroscopies, including ARPES and XPS, are highly *surface* sensitive probes of materials due to the small inelastic mean free path (IMFP) of photoelectrons. The relationship between IMFP and photon energy is summarized by the universal mean free curve [130] (see Fig. 5.6(b)). Measured photoemission intensities generally follow an exponential form for attenuation [131]:

$$dI = I_0 \cdot X(z) \cdot e^{-z/\lambda\cos(\theta)} dz. \tag{4.8}$$

Here, the measured photoemission intensity I_0 depends on the total photoelectron intensity I_0, the vertical depth below the sample surface z, the atomic fraction $X(z)$ at each depth z, the IMFP λ, and the photoelectron collection angle θ from the surface normal. From Eq. 4.8, the measured intensity is $I \approx 0.95 I_0$ within three IMFPs below the surface, which provides an upper limit for the probing depth accessible by ARPES. For a typical He emission line ($E_{\mathrm{ph}} = 21.2\,\mathrm{eV}$), the IMFP is 2.8 Å, corresponding to an effective measured depth of 8.4 Å. Thus, ARPES measurements should be interpreted to be valid only within 1 nm of the sample surface, which makes ARPES especially suitable for quantum materials with novel surface physics such as topological insulators.

4.2 ARPES on Bi_2Se_3 and $Co_3Sn_2S_2$

An example of ARPES data collected on Bi_2Se_3 is shown in Figure 4.1, taken with the Scienta Omicron ARPES system at UC Davis with $E_{\text{ph}} = 21.2\,\text{eV}$. Here, as with most ARPES experiments, the Bi_2Se_3 sample is freshly cleaved *in situ*, with the analysis pressure in the ultra-high vacuum regime ($< 1 \times 10^{-10}\,\text{mbar}$) to minimize surface adsorbates and contaminants that will degrade the ARPES spectrum. In the spectrum in Figure 4.1, all of the expected features of the Bi_2Se_3 band structure are present. The Fermi-Dirac cutoff is visible at E_F and is indicated by the black line. The regions of spectral intensity (green) show the bulk conduction and bulk valence bands separated by the bulk band gap of $E_g = 0.3\,\text{eV}$. In this Bi_2Se_3 sample, E_F intersects the bulk conduction band, confirming the bulk metallicity of the sample. E_F can be determined by identifying the spectral intensity cutoff, and the energy axis is offset to be in units of binding energy ($E - E_F = -E_B$).

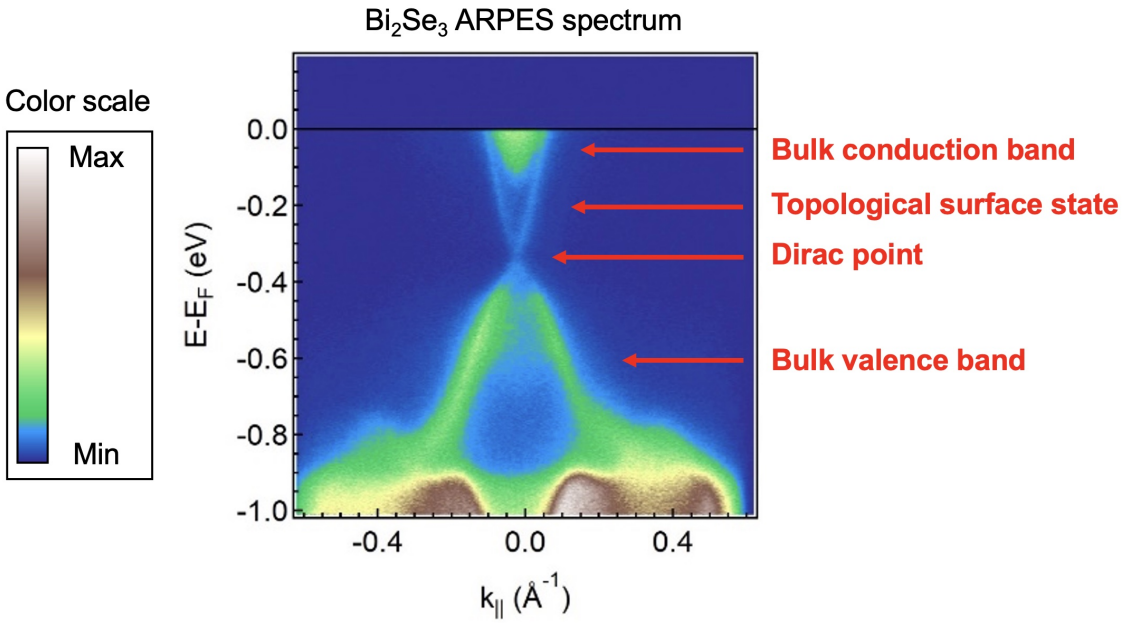

FIGURE 4.1. ARPES spectrum of Bi_2Se_3 taken with the Vishik Lab system at UC Davis, using $E_{\text{ph}} = 21.2\,\text{eV}$ at $T = 14\,\text{K}$. Key features of the band structure are labeled: the bulk bands, topological surface state, and the Dirac point. The intensity color scale is shown at the left.

The APRES data also shows several features indicative of the 3D TI character of Bi_2Se_3. The bulk valence band shows the distortion near the valence band edge originating from the characteristic band inversion of Bi_2Se_3. The topological surface state is observable in between the bulk bands showing the characteristic linear Dirac dispersion, with a corresponding Dirac point near $E_B = 0.35\,\text{eV}$. Due to the surface sensitivity of ARPES, the topological surface state is observable along with the bulk bands.

It should be noted that the Bi_2Se_3 spectra were taken at a fixed, low temperature ($T = 14\,\text{K}$) to maximize the quality of the spectrum. In other materials, it is common to observe temperature-dependent changes in the band structure, which ARPES is also sensitive to. In a different topological quantum material, the magnetic Weyl semimetal $Co_3Sn_2S_2$, ARPES measurements demonstrate a rigid band shift through the ferromagnetic transition at $T_c = 177\,\text{K}$ [**127**]. Figure 4.2 shows ARPES energy distribution curves (EDCs) demonstrating this shift, which is about $\sim 115\,\text{meV}$ and can be most prominently seen when comparing the curvature plots in Fig. 4.2(b1,b5) at $k_x = 0\,\text{Å}^{-1}$. These experimental results and supporting tight-binding modeling suggest that the material evolves from a Mott ferromagnet below T_c to a correlated metal above T_c. In $Bi_{2-x}Sb_xSe_3$ and $Cu_xBi_2Se_3$, future temperature-dependent ARPES measurements can provide insight into the band structure changes concomitant with the onset of the low temperature excitonic and superconducting phases in these materials, respectively.

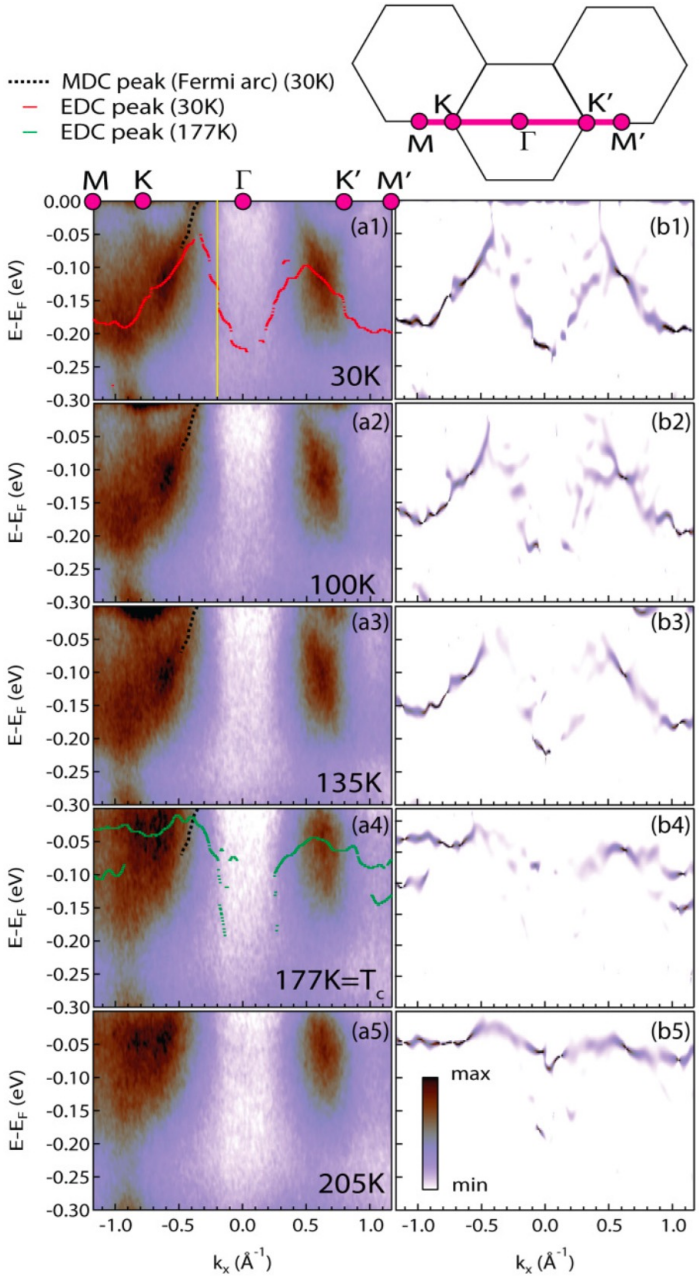

FIGURE 4.2. $Co_3Sn_2S_2$ ARPES spectra taken at Beamline 7.0.2 (MAESTRO) at the Advanced Light Source (ALS). Panels (a1)-(a5) are spectra taken at the indicated temperatures, with the panels (b1)-(b5) showing the respective curvature plots [132]. The shown k_x range is along the $M - K - \Gamma - K' - M$ cut of the Brillouin zone, and the Fermi-Dirac cutoff convolved with the energy resolution has been divided out for all spectra. All spectra were taken using $E_{\text{ph}} = 115\,\text{eV}$. The energy distribution curve (EDC) local maxima are indicated by the red and green points overlaying the spectra in (a1, a4). The black dashed line indicates the position of a band that forms a Fermi arc. Figure adapted from Ref. [127].

4.3 6 eV laser ARPES

Historically, VUV energies have been attained either by using gas-discharge lamp sources or synchrotron light sources. Laser-based light sources are increasingly becoming ubiquitous as advances in ultrafast and nonlinear optics now allow for practical generation of intense VUV pulses and high harmonics in typical laboratory settings. The ultrafast pulses of the Mai Tai laser used in the OPP apparatus in Chapter 2 and Chapter 3 can be used to seed VUV pulses, and serves as a quasi-steady state replacement for the He gas lamp. To do this, the energy of the optical pulses must be tuned from $E_{\text{ph}} = 1.55\,\text{eV}$ to higher VUV energies, which is well outside the intrinsic tunability of the Mai Tai laser. Fortunately, nonlinear optical processes provide a pathway to doing this, namely second harmonic generation (SHG).

In linear optics, the electric polarizability is assumed to be proportional to the applied electric field ($\mathbf{P} = \chi\mathbf{E}$), with the electric susceptibility χ being the constant of proportionality. This assumption is only valid in situations when the electric field is small, which breaks down when considering the case of intense laser pulses. In the high E-field limit, the electric susceptibility and polarizability can be expanded as a Taylor series in increasing powers of E [133]:

$$\chi(E) = \chi^{(1)} + \chi^{(2)}E + \chi^{(3)}E^2 + \dots \tag{4.9}$$

$$P = \chi(E) \cdot E = \chi^{(1)}E + \chi^{(2)}E^2 + \chi^{(3)}E^3 + \dots \tag{4.10}$$

In the high E-field limit, higher order nonlinear terms in P become significant and cannot be ignored optically.

In general, nonlinear optics allows one to generate a nonlinear output wave ω_p from multiple input waves $\omega_1, \omega_1, \dots, \omega_n$ governed the n^{th} order electric susceptibility for the process: $\chi^{(n)} = f(\omega_p, \omega_1, \omega_2, \dots, \omega_n)$. In the case of second harmonic generation, the susceptibility

is $\chi^{(2)} = f(2\omega, \omega, \omega)$, which generates of a single wave of frequency 2ω by mixing two input waves of frequency ω (i.e., the second harmonic). Given an intense input wave with propagation wavevector $\mathbf{k}(\omega)$

$$E(x,t) = Ae^{-i[\omega t - k(\omega)x]}, \tag{4.11}$$

the resulting nonlinear polarization to second order is

$$\chi^{(2)}E(x,t)^2 = Be^{-i[2\omega t - 2k(\omega)x]} \tag{4.12}$$

where A and B are arbitrary constants. To produce an output wave with frequency 2ω, there must be an electric field with 2ω produced:

$$E_{2\omega}(x,t) = Ce^{-i[2\omega t - k(2\omega)x]} \tag{4.13}$$

Equating $E_{2\omega}(x,t) = \chi^{(2)}E(x,t)^2$ yields the phase matching condition: $2k(\omega) = k(2\omega)$. Since $k(\omega) = \frac{n(\omega)\cdot\omega}{c}$, the phase matching condition can also be usefully expressed in terms of the index of refraction of the medium:

$$n(\omega) = n(2\omega). \tag{4.14}$$

To satisfy the SHG phase matching condition in Eq. 4.14, uniaxial birefringent crystals can be used as they naturally have different $n(\omega)$ for different input polarizations. In the 6 eV ARPES setup at UC Davis, negative uniaxial β-barium borate ($\beta-$BBO) crystals are used for SHG, which combine two ordinary polarized input waves to generate one frequency doubled extraordinary polarized output wave. This is known as Type I phase matching for negative uniaxial crystals, and the polarization directions are flipped for positive uniaxial crystals. In Type II phase matching, the polarizations of the input waves are perpendicular to one another.

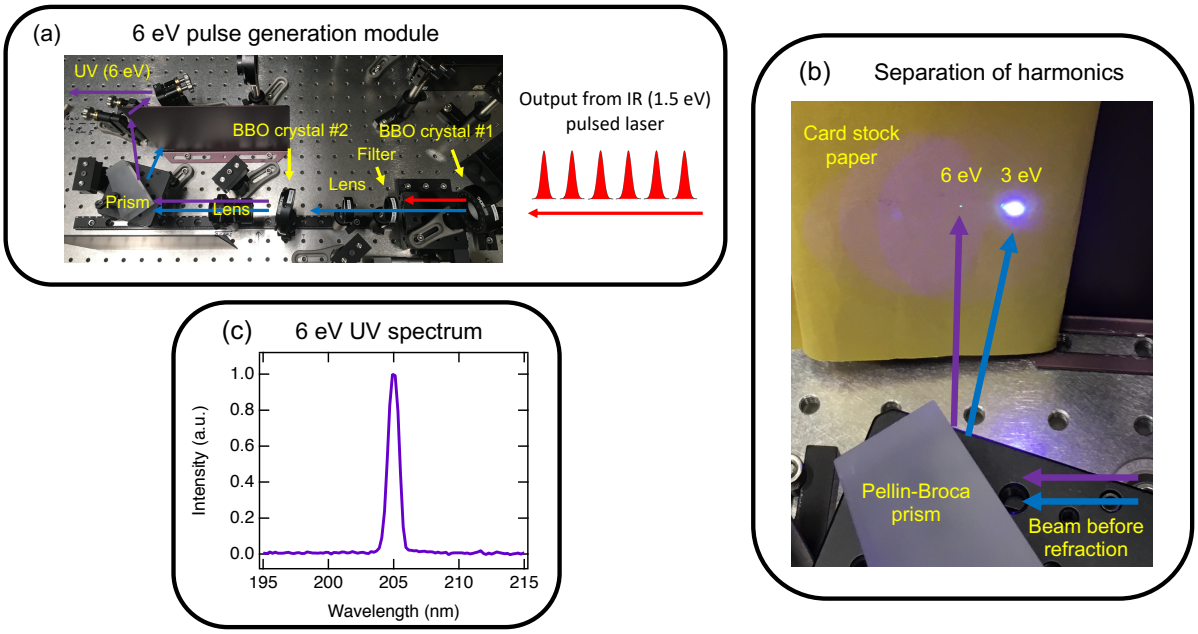

FIGURE 4.3. Schematics of the 6 eV SHG module. (a) Photographs of the 6 eV module components, with the 3 eV beam (blue) and the final 6 eV beam (purple). (b) Photograph of SHG-generated and prism separated 3 eV and 6 eV harmonics, confirmed by observing two spots on card stock paper. (c) UV spectrum of the 6.05 eV beam centered around $\lambda = 205$ nm, with FWHM = 1.1 nm (0.032 eV).

A diagram of the 6 eV pulse generation module is shown in Figure 4.3. After redirecting the output of the Mai Tai laser with a removable mirror, the beam is focused with lenses (Thorlabs) onto two collinear β-BBO crystals (Inrad Optics) placed in the optical path used to frequency quadruple ($2 \times$ SHG) the input ($E_{\text{ph}} = 1.51\,\text{eV} \rightarrow E_{\text{ph}} = 3.02\,\text{eV} \rightarrow E_{\text{ph}} = 6.05\,\text{eV}$). The β-BBO crystals are angled in (θ, ϕ) to satisfy the phase matching condition and to maximize the SHG intensity. A bandpass filter (Thorlabs FBH400-40) is placed after the first β-BBO crystal to block unconverted $E_{\text{ph}} = 1.51\,\text{eV}$ light from passing through the second β-BBO crystal, and a Pellin-Broca prism (Thorlabs ADBU-20) disperses out the final $E_{\text{ph}} = 6.05\,\text{eV}$ output from the collinear $E_{\text{ph}} = 3.02\,\text{eV}$ beam (Fig. 4.3(b)). The UV spectrum of the 6.05 eV laser is plotted in Fig. 4.3(c), showing a narrow full width at half maximum of 0.032 eV (1.1 nm), demonstrating the success of the 2xSHG approach.

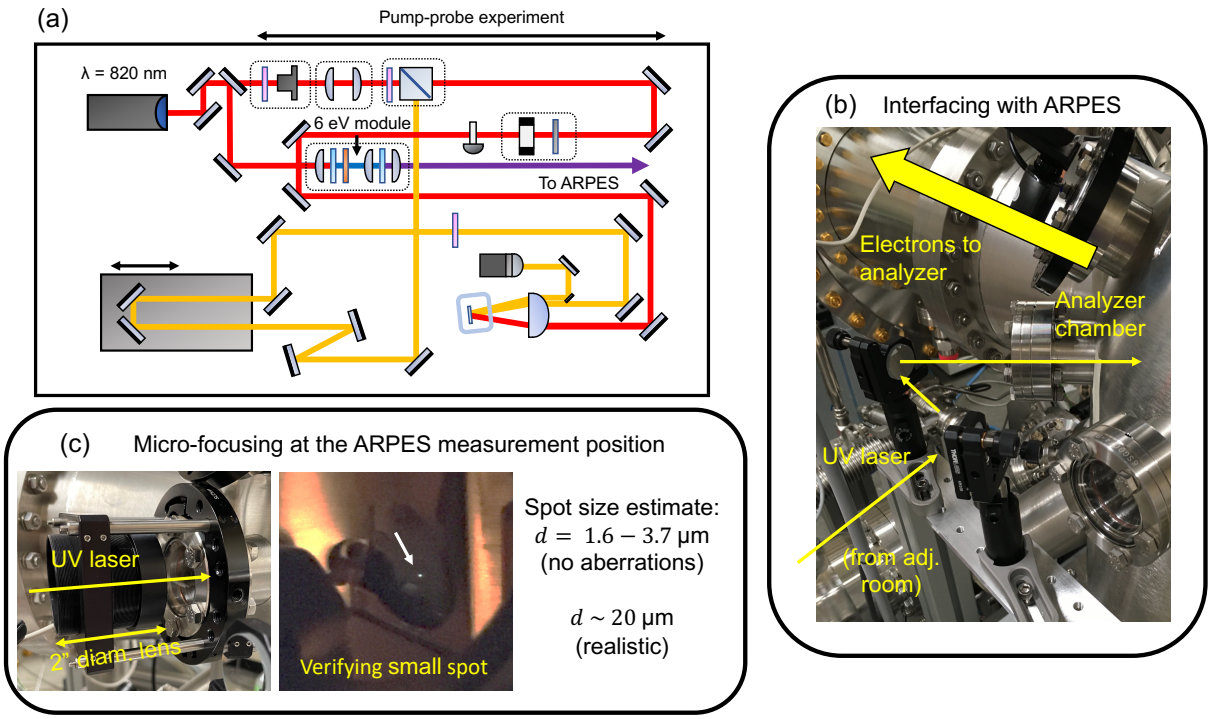

FIGURE 4.4. Interfacing the ARPES system with the 6 eV laser. (a) SHG module located with respect to the existing OPP apparatus. (b) Mirrors directing the 6 eV beam to the ARPES system. (c) Optical cage to focus the 6 eV into the ARPES analysis chamber. The UV-grade fused silica lens (Thorlabs) is held in an adjustable lens tube mount, allowing for fixed control of the focused spot position. A fluorescent spot on silver epoxy shows the final focused 6 eV spot.

Figure 4.4 shows the how the 6 eV laser is interfaced with the ARPES system. After the 6 eV beam is generated by the module in Fig. 4.3, it is directed into the ARPES analyser chamber in the adjacent room using the Al-coated mirrors (Newport) in Fig. 4.3(a) and Fig. 4.4(b), and is focused into the chamber through a VUV-compatible fused silica viewport (MDC Vacuum). The photographs in Fig. 4.4 show the final focused 6 eV spot on the ARPES sample manipulator, which has an estimated spot diameter of $d < 20\,\mu$m.

To demonstrate the photoemission capabilities of the 6 eV laser, Figure 4.5 shows an example of data taken with the ARPES basement system pictured in Fig. 4.5(a). The ARPES spectra using the 6 eV laser source is shown in Fig. 4.5(c), showing the well-defined

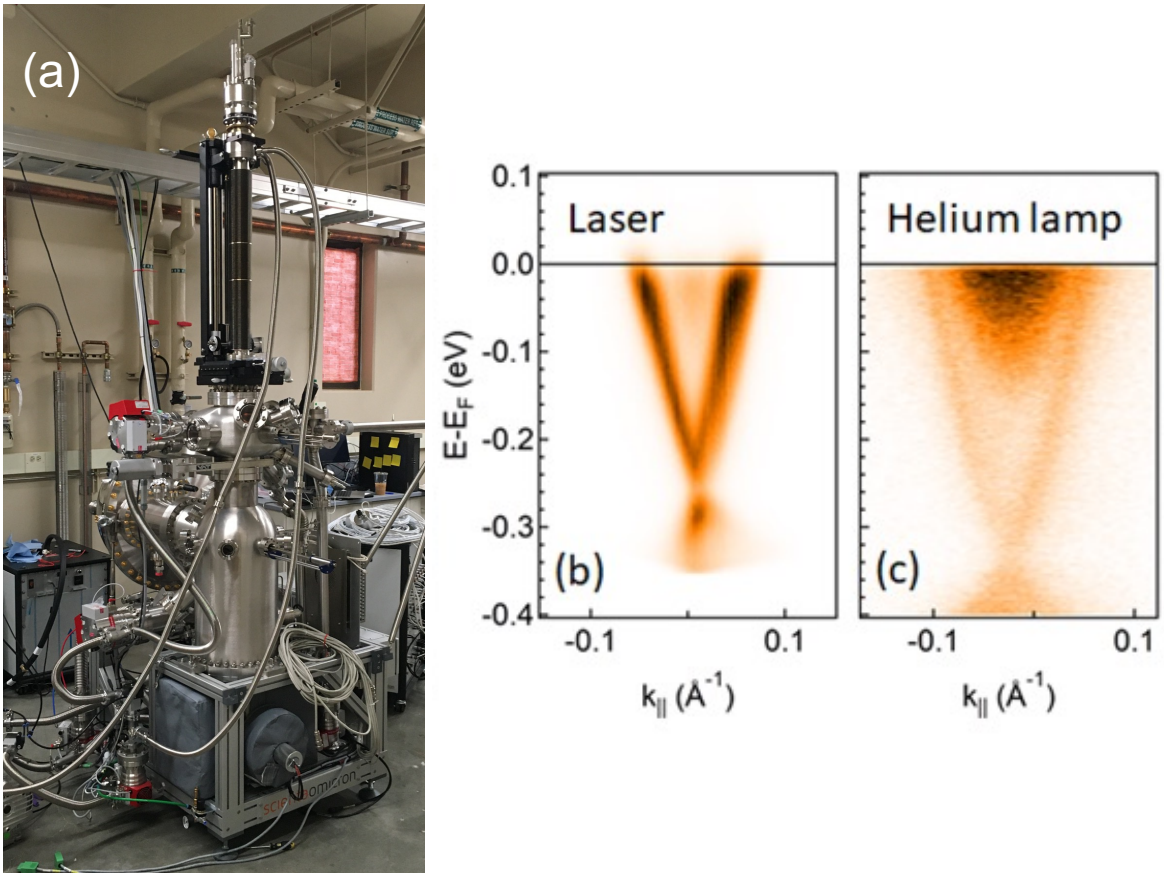

FIGURE 4.5. Bi_2Se_3 micro-ARPES spectra. (a) Photograph of the ARPES instrument. (b) Bi_2Se_3 ARPES spectra taken with 6 eV laser source at $T = 80$ K. (c) Bi_2Se_3 ARPES spectra taken with the He lamp source at $T = 10$ K, over a similar $k_{||}$ range.

Dirac cone of the topological surface state in Bi_2Se_3. Compared to corresponding spectra taken with the He lamp source (Fig. 4.5(c)), the 6 eV spectra are limited to a smaller $k_{||}$ range. This is due to the lower photon energy of the 6 eV laser compared to the $E_{\text{ph}} = 21.2$ eV He lamp energy. The He lamp is able to excite electrons from the full first Brillouin zone, while 6 eV is only able to access about two thirds of the first Brillouin zone [**134**]. The overall effect is a spectrum over a smaller $k_{||}$ range, which can be valuable if mainly interested in measuring features near $k_{||} = 0$ Å^{-1}, such as the topological surface state of Bi_2Se_3. It is notable that the Dirac cone appears more intense in Fig. 4.5(b), which is

possibly due to the different matrix elements of I_0 in Eq. 4.6 when using $E_{\text{ph}} = 6\,\text{eV}$ versus $E_{\text{ph}} = 21.2\,\text{eV}$. With further minimization of the 6 eV spot size to below the intrinsic sample surface irregularities, it can be possible to achieve further quality gains over the He lamp source and better resolution of the surface state.

Another advantage of using the 6 eV source is the ability to focus the beam to micron-scale spots. This is useful when optimizing sample position to identify an ideal spot on the surface to measure. In Bi_2Se_3 it is known that features of the electronic structure can vary spatially, namely the binding energy of the Dirac point [**135**], which micron-level focusing can help resolve or mitigate. Sample heterogeneity or variation in composition could point to a possible reason why the Dirac point energy is significantly shifted in the 6 eV data, as compared to the He lamp spectra taken over a wider area. A focused spot can also be used to target smaller samples like Bi_2Se_3 nanoplatelets, or nanoscale devices with the advent of nano-ARPES at synchrotron light sources [**136**].

Chapter 5

X-ray photoelectron spectroscopy

5.1 Introduction

X-ray photoelectron spectroscopy (XPS) is a photoemission technique sensitive to the core levels of elements, and therefore the composition and chemistry of materials. As with ARPES, it is based on the photoelectric effect:

$$E_{\text{kin}} = h\nu - E_B - \phi \tag{5.1}$$

where the main measurable is the photoelectron kinetic energy E_{kin} (or equivalently the binding energy E_B) of each core level ($1s, 2s, 2p, ...$). XPS has historically been used to great success in quantifying the composition of materials and discriminating between the different oxidation states of elements, allowing one to determine the bonding environment of different elements in a given material.

In XPS, the photon energies used ($200\,\text{eV} - 100\,\text{keV}$) are typically higher than in ARPES, providing full access to the core levels, instead of only the valence band states close to E_F. As with ARPES, both lab-based and synchrotron-based experiments are possible. In lab-based systems, Al-Kα ($E_{\text{ph}} = 1486.6\,\text{eV}$) and Mg-K$\alpha$ ($E_{\text{ph}} = 1253.6\,\text{eV}$) X-ray sources are commonly used, while at synchrotron endstations the X-ray source is synchrotron radiation.

A survey spectrum showing the core levels for $Cu_{0.3}Bi_2Se_3$ is shown in Figure 5.1. The measured XPS intensity is the photoelectron intensity originating from the different elemental core levels present in the material, and is usually reported in counts or counts per second. Each element in the material has a set of states that appear as peaks with defined binding energies E_B, which are commonly tabulated in standard references [**137**]. In this survey spectrum, all core levels below $E_B = 650\,\text{eV}$ are visible in the scan. To better measure peak intensity and structure, narrower, higher resolution scans of individual levels are taken to quantify XPS data.

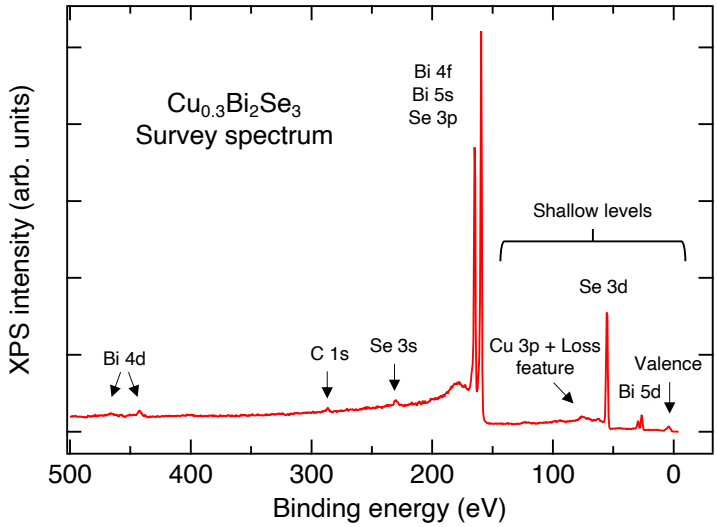

FIGURE 5.1. $Cu_{0.15}Bi_2Se_3$ XPS survey spectrum taken with $E_{\text{ph}} = 650\,\text{eV}$ in high vacuum. Cu, Bi, and Se core levels are labeled, with the dashed box indicating the shallow core levels analyzed in this work. The adventitious C 1s peak is also labeled.

5.2 Energy scales in spectroscopy

A useful way to compare the techniques presented so far is by considering the different excitation energy scales, or the photon energy ranges used for each technique. The previous optical pump-probe experiments employ optical excitation energies of $E_{\text{ph}} = 1.55\,\text{eV}$, providing a measure of the bulk and surface carrier dynamics in materials near the Fermi energy

E_F. ARPES uses higher excitation energies ($E_{\text{ph}} > 20\,\text{eV}$) and thus is directly sensitive to electronic states in the valance and conduction bands, like the metallic topological surface states in Bi_2Se_3. XPS uses X-ray excitation energies both in the soft X-ray ($E_{\text{ph}} > 200\,\text{eV}$) and hard X-ray regimes ($E_{\text{ph}} > 5000\,\text{eV}$) and is thus able to quantify elemental core levels at the surface of Bi_2Se_3. Hard X-ray energies in XPS can be used to study the bulk of materials in addition to the chemistry of the surface.

5.3 Lab-based XPS systems

Lab-based XPS systems are among the most commonly used characterization tools in modern surface science, due to their relative accessibility and proven ability to acquire high quality spectra. At UC Davis, the standard XPS instrument is the Kratos AXIS Supra$^+$. In addition to standard Al-Kα and Mg-Kα X-ray sources, it is equipped with a monochromatic dual Al-Kα/Ag-Lα 1486.6 eV/2984.2 eV source, which extends the usable photon energy range for greater surface measurement depth. Monochromatic sources are advantageous for providing a smaller XPS peak linewidth and greater energy resolution over non-monochromatic sources. The instrument is also equipped with a He I/He II ultraviolet photoelectron spectroscopy (UPS) source, to collect valence band XPS spectra complementary to band structure measurements from ARPES. Fig. 5.2(a) shows a photograph of the system.

To acquire spectra, samples are placed on a motorized stage and transported to the analysis chamber, which is kept at high or ultrahigh vacuum like with ARPES. After the sample is aligned to maximize the XPS signal, spectra are collected using the 128 channel Delay-Line Detector (DLD) in the electron analyzer. Commonly tuned parameters include the emission current of the X-ray source, the pass energy of the analyzer, and the acquisition time, which are selected based on the desired energy resolution and overall quality of the spectra. Appropriate settings, in combination with monochromatic sources and the DLD

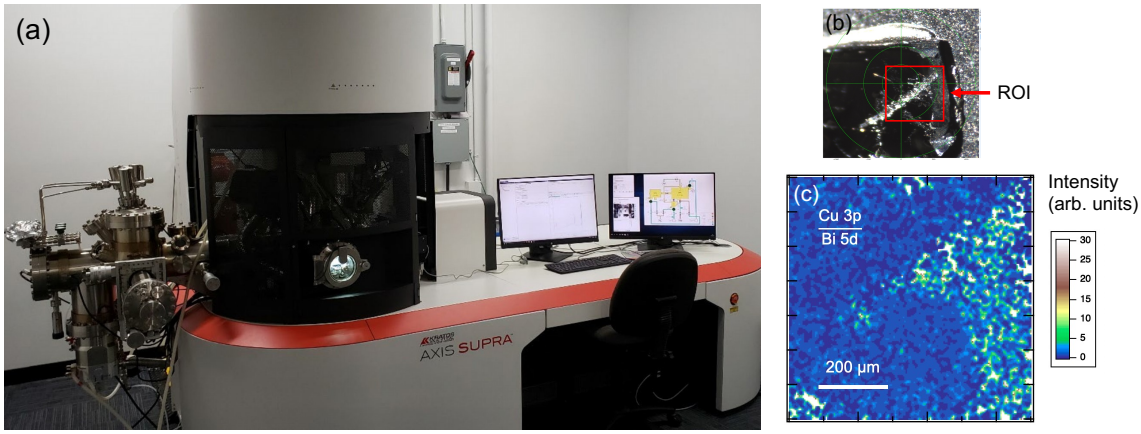

FIGURE 5.2. Kratos AXIS Supra$^+$ XPS instrument at UC Davis. (a) Image of the system, courtesy of Andrew Thron. (b) Optical microscope image of a $Cu_{0.15}Bi_2Se_3$ sample loaded in the analysis chamber, with the red box showing the approximate region of interest (ROI). (c) Micro-XPS image of the ROI. The image intensity is expressed as the total Cu 3p XPS peak intensity, normalized by the Bi 5d peak intensity.

detector, allow for excellent spatial and energy resolution to resolve small surface chemical concentrations (up to parts per million) and sub-eV chemical shifts of peaks.

Thanks to advances in electron optics and detection, imaging is now possible with lab-based XPS instruments. While not the focus of this work, XPS imaging allows for the collection of spectral images of a sample surface. In XPS images, each pixel is a complete spectrum including chemical shifts, with micron-scale resolution. This capability is advantageous in materials or devices with considerable surface heterogeneity in situations where precise chemical information is needed in addition to imagery. Fig. 5.2(c) is a micro-XPS image of a region of a rough $Cu_{0.15}Bi_2Se_3$ sample surface (Fig. 5.2(b)) showing considerable surface heterogeneity. Note the bright spectral region to the right, which indicates elevated concentration of surface Cu there versus at the center of the sample.

5.4 Quantification in XPS

There are often multiple quantities of interest in an XPS dataset, and care must be taken to accurately quantify XPS data. XPS is very sensitive to the chemical composition (i.e.,

the relative abundances of elements in a given compound within the probing volume), so to quantify the total fraction of a particular element, peaks are fitted to the data. There are several different functional forms for peaks that can be chosen (e.g., Gaussian, Lorentzian, Voigt, Doniach-Sunjic, etc.) and peak fitting is typically done using standard peak fitting software such as CasaXPS or KolXPD [**138**,**139**]. The total area of the fitted peak is typically what is reported as the XPS intensity, where the intensity of each peak is proportional to the amount of the corresponding element in the material. The selection of peak functions and the number of peaks to be fit depends on the material, the number of chemical shifts/oxidation states present for each element, and other assumptions specific to the scientific question being studied. To demonstrate XPS peak fitting, Figure 5.3 shows a typical XPS spectrum for a pair of Bi 5d core levels. In this example, the parameters of the fit were freely chosen to best fit the data, but parameters such as the spin-orbit peak splitting can be held fixed (if independently known) to increase quantification accuracy. The area under the overall fit and above the fitted background is the overall XPS peak intensity for this set of Bi 5d core levels.

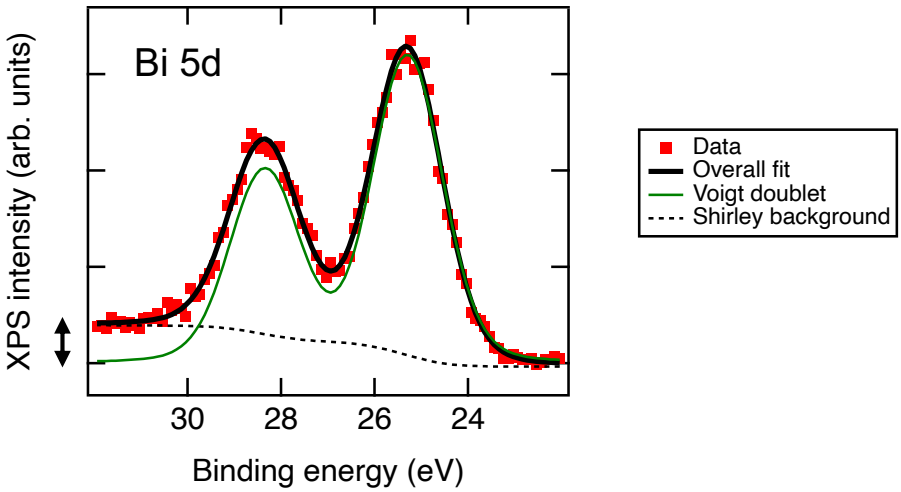

FIGURE 5.3. Bi 5d core levels in $Cu_{0.15}Bi_2Se_3$, taken with $E_{ph} = 900\,eV$. Two Voigt peaks (green) and a Shirley background (dashed) are fitted to the raw data. The black double arrow indicates the higher background on the higher E_B side.

After choosing a suitable background and fitting peaks, it is possible to meaningfully interpret the XPS intensities. The atomic fraction of each element X can be generally written as:

$$X = \frac{I/S}{\Sigma_j I_j/S_j} \tag{5.2}$$

where S_j is the relative sensitivity factor (RSF) for each present element j [140, 141]. As shown in Eq. 5.2, elements must be scaled by a factor S that is proportional to the sensitivity of that element per given E_{ph}, and these values are often tabulated by the manufacturer of the particular XPS instrument. For synchrotron-based experiments, the RSF can be generally expressed as $S_j = \sigma_j \cdot \Phi \cdot T \cdot \lambda$. The dominant term in the RSF is the photoionization cross section σ_j, which is the probability of emitting an electron for a particular core level per E_{ph}. The well known Yeh-Lindau formula can be used to compute the cross section for different photon energies in different experimental configurations [142]:

$$\frac{d\sigma_{nl}(h\nu)}{d\Omega} = \frac{\sigma_{nl}(h\nu)}{4\pi}[1 + \beta_{nl}(h\nu)P_2(\cos\gamma)], \tag{5.3}$$

where $\sigma_{nl}(h\nu)$ is the photoionization cross section for levels with quantum numbers (n, l), $\beta_{nl}(h\nu)$ is the asymmetry parameter, and $P_2(\cos\gamma) = \frac{1}{2}(3\cos^2\gamma - 1)$, with γ defined as the angle between the photoelectron emission direction and the X-ray polarization vector. In Figure 5.4, the photoionization cross sections are plotted for Se 3d, Cu 3p, and Bi 5d.

In the remaining terms in the RSF, Φ is the photon flux, T is the analyzer transmission function, and λ is the inelastic mean free path (IMFP). These terms are important when comparing XPS intensities taken with different photon energies and core levels with different E_{kin}. Typically Φ and T can be measured independently for a given XPS instrument, and the IMFP is estimated or calculated for the material of interest using the Tanuma, Powell, and Penn algorithm (TPP2M) [143].

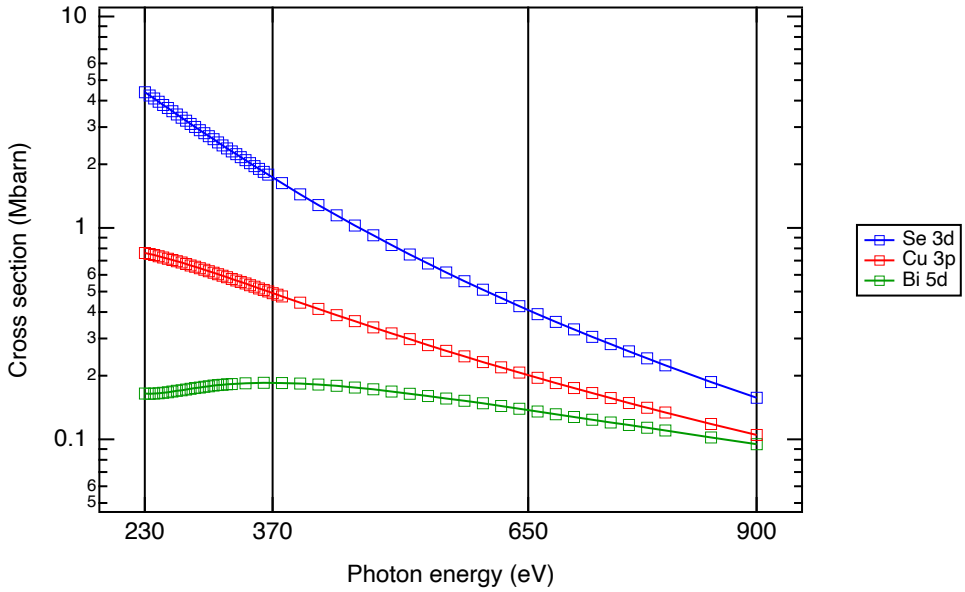

FIGURE 5.4. Photoionization cross sections $\sigma(h\nu)$ for Se 3d, Cu 3p, and Bi 5d. The beamline photon energies used in this work are indicated with solid black lines. Values obtained from Refs. [142, 144]

5.5 Backgrounds in XPS

All XPS spectra have a complicated background, with contributions arising from inelastically scattered electrons, surface nanostructures, plasmons resonances, detector artifacts, and sometimes overlapping adjacent peaks [131, 140, 141]. In the vicinity of each core level, the XPS intensity must thus be interpreted as being measured above some background. In the example in Fig. 5.3, it is clear that the intensity at the higher E_B side of the peaks is higher than the lower E_B side (double arrow), with the fitted Bi 5d core levels in the middle. The rising background arises from inelastic kinetic energy losses of photoelectrons as they are emitted from the material, which lowers their E_{kin} and increases the higher E_B side.

There are several approaches for fitting a background or otherwise background-correcting an XPS dataset. A simple linear background is often sufficient, which simply models the XPS background as a sloped line. A Shirley background is more accurate, which assumes that the changes in the background are proportional to the intensities of the peaks. A Tougaard

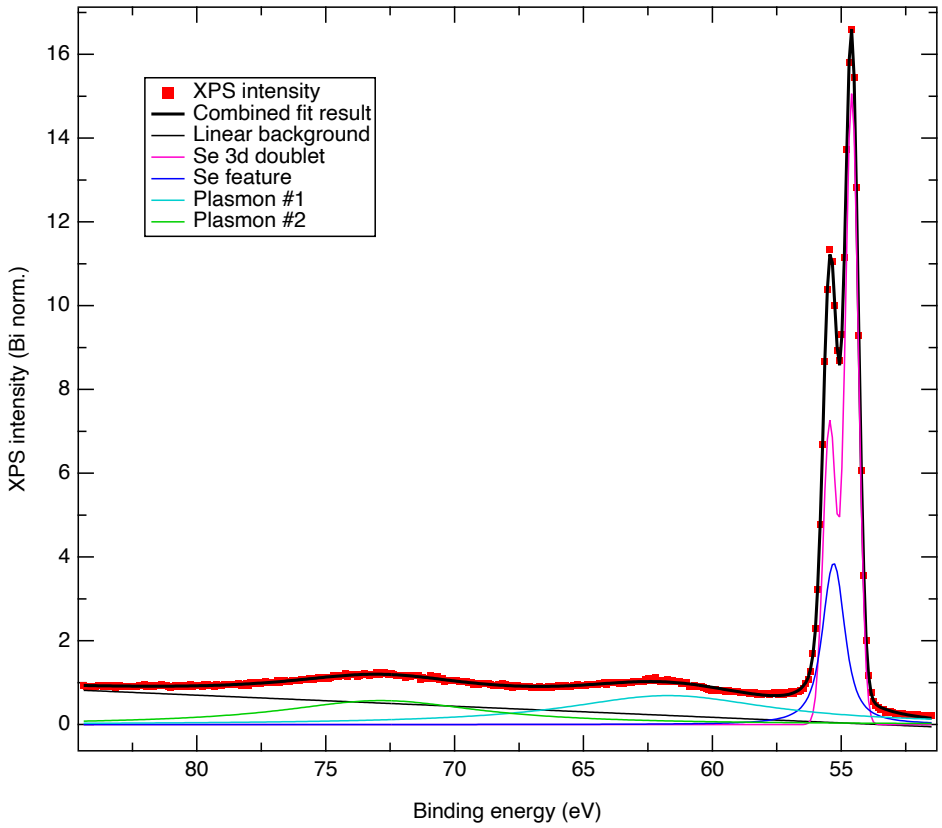

FIGURE 5.5. Loss feature fits for Bi_2Se_3 XPS spectra, taken right after cleaving the sample surface. The fitted XPS spectrum for Bi_2Se_3 includes the Se 3d core levels and the plasmon loss features. The measured data is in red, the individual fitted peaks are the colored curves, and the combined fit result is the solid black curve. A linear background was fitted over the entire region.

background fully models the inelastic scattering processes that comprise the background, and is thus the most physically accurate [131].

Backgrounds can also be empirically determined. For example, to model the background of the $Cu_{0.3}Bi_2Se_3$ spectrum in the region near the Se 3d and Cu 3p levels, a measured Bi_2Se_3 reference spectrum can be used. By way of modelling the background using a very closely related reference material, more complicated features in the background such as plasmon energy losses can be accounted for in XPS quantification. Figure 5.5 shows the fitting procedure employed to construct a background based on a Bi_2Se_3 reference spectrum. If any additional peaks like Cu 3p are present above the loss feature background in $Cu_{0.3}Bi_2Se_3$,

they can be accurately quantified. This background correction method will be the basis for interpreting the $Cu_{0.3}Bi_2Se_3$ AP-XPS results in Chapter 6.

5.6 Synchrotron-based XPS

A synchrotron is a light source capable of producing highly bright, monochromatic X-ray light that can serve as the X-ray source for X-ray spectroscopies and scattering experiments, including XPS and ARPES. Fig. 5.6(a) shows a schematic of the Advanced Light Source synchrotron at Lawrence Berkeley National Laboratory, with the key components labeled [**145**]. Electrons are initially generated and accelerated to near-light speed after passing through the linear accelerator and the booster ring. Electrons are subsequently stored in a circular storage ring, which tangentially emits synchrotron radiation that is then redirected by X-ray optics to beamlines and individual endstations. The chief advantage of performing an XPS experiment using synchrotron radiation is arguably the tunability of the X-ray photon energy, which can be easily controlled by the user with endstation monochromators. This is advantageous in XPS quantification because it makes it possible to fix the kinetic energy of emitted electrons solely by varying the energy of the incident X-rays, permitting more accurate quantification of elements whose core levels may be widely separated in binding energy. This approach is not possible with common fixed X-ray sources, where the kinetic energies of widely spaced core levels may be separated by hundreds of eV, meaning that non-constant depths in the material are sampled. This is due to the varying IMFP of photoelectrons versus kinetic energy, which is shown in Fig. 5.6(b). Conveniently, tuning the photon energy also allows one to reduce discrepancies arising from the energy-dependent analyzer transmission function by maintaining constant kinetic energy.

At a synchrotron light source, it is also possible to controllably tune the X-ray photon energy to obtain a depth profile of any particular element, where the measured depth is proportional to $3 \times$ IMFP. For example, using a higher photon energy (e.g., $E_{\text{ph}} \sim 1000\,\text{eV}$) will yield data that is more representative of the bulk of the material than using $E_{\text{ph}} \sim 100\,\text{eV}$

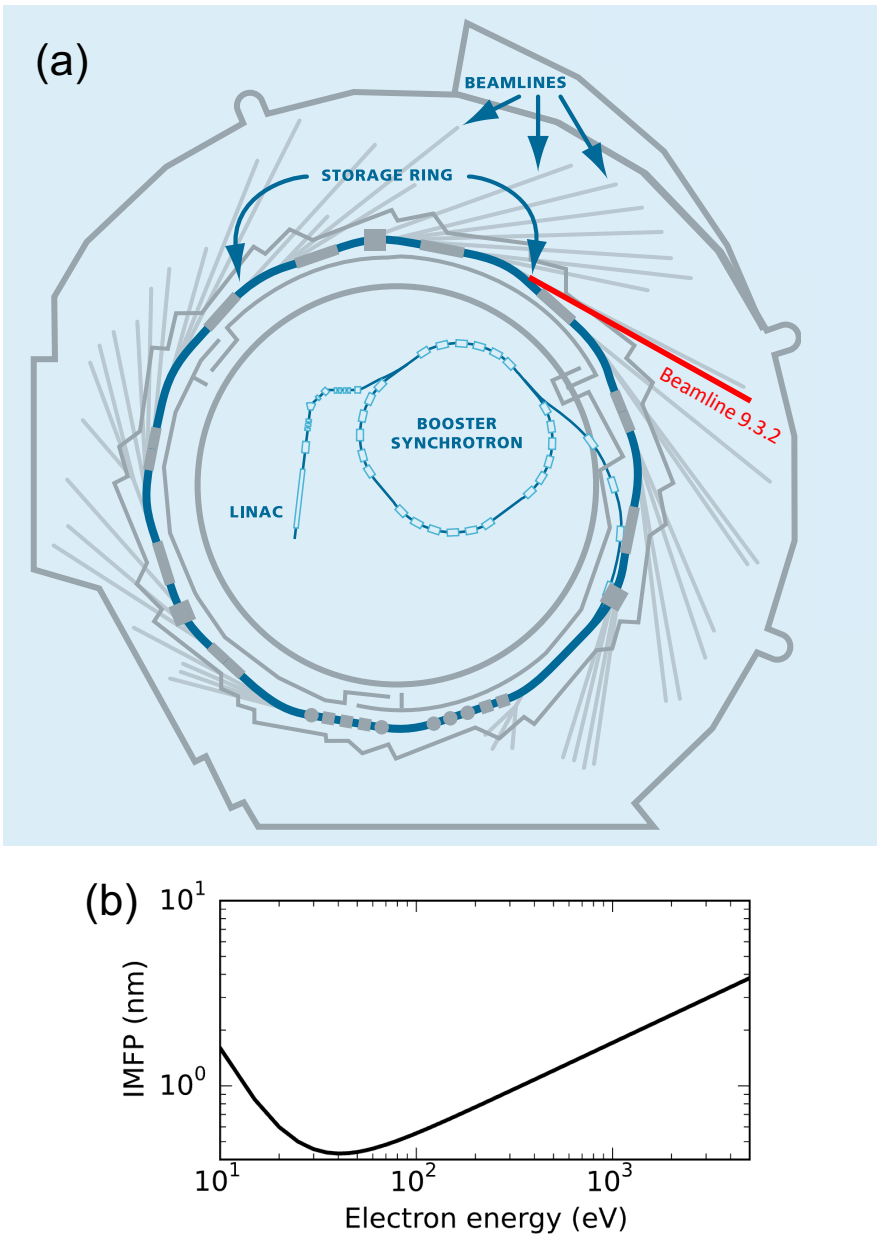

FIGURE 5.6. Photon energy tunability at the Advanced Light Source synchrotron. (a) Diagram of the Advanced Light Source at LBNL. Beamline 9.3.2 (Ambient Pressure Soft X-ray Spectroscopy) is indicated in red. Figure adapted from LBNL press release [145]. (b) Plot of the universal IMFP curve versus electron excitation energy [130] (adapted from Wikipedia).

because of the higher IMFP accessible using higher photon energies (Fig. 5.6(b)). For a given material, the actual IMFP may deviate somewhat from the universal curve shown in Fig. 5.6(b), so a more accurate determination of the IMFP specific to a particular material is often obtained with the TPP2M algorithm in software such as QUASES [**143**]. Thus, for any given core level, a sequence of E_{ph} can be chosen to yield a set of XPS spectra that correspond to a specific depth for each element in the material.

5.7 Ambient pressure XPS

Ambient pressure XPS (AP-XPS) is an enhancement of standard XPS, which additionally allows samples to be exposed to atmospheric gases *in situ* during measurements, providing the capability to quantify chemical changes in the XPS spectra in real-time [**146**–**148**]. Images of the AP-XPS station at the Advanced Light Source (Beamline 9.3.2) are shown below in Figure 5.7. Key to the success of the technique is the differential pumping of the analyzer, which gradually steps down the pressure of the analyzer from the ambient pressure of the analysis chamber (Figure 5.7(b)), allowing photoelectron spectra to be obtained [**147**].

Common gases employed include O_2, H_2O, CO_2, as well as mixtures of gases to approximate atmospheric compositions. Partial pressures in AP-XPS are limited to $\sim 100\,\mathrm{mbar}$ for many AP-XPS systems, making it more accurate to describe the pressures as near-ambient (NAP-XPS) rather than fully atmospheric in nature ($P = 1013.25\,\mathrm{mbar}$). However, compared to typical $< 1 \times 10^{-6}\,\mathrm{mbar}$ high vacuum pressures in XPS experiments, AP-XPS is an entirely distinct regime in XPS, capable of studying any material in a gaseous environment that yields a good XPS signal. As with synchrotron-based XPS, it is possible to perform AP-XPS measurements using synchrotron radiation, allowing one to reliably quantify surface changes in chemically-selective and depth-selective manners.

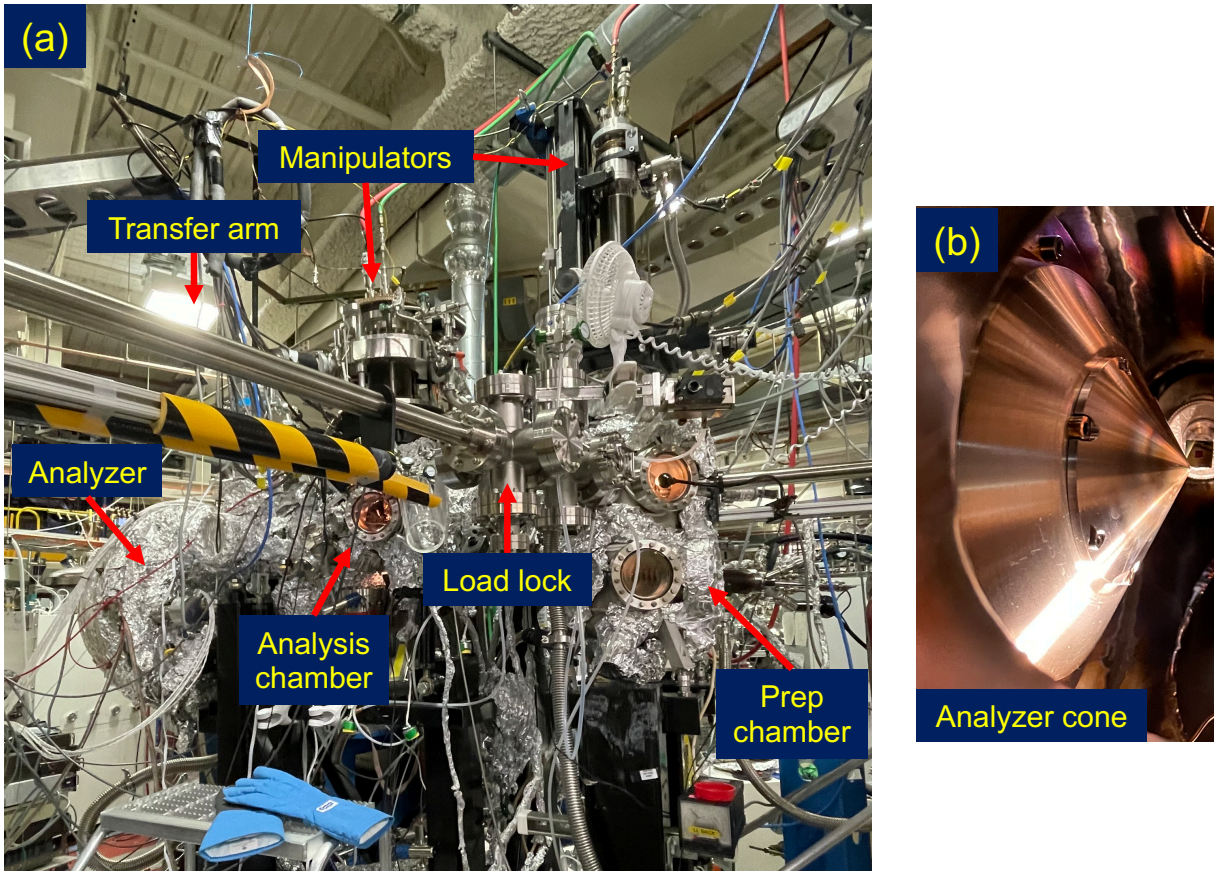

FIGURE 5.7. AP-XPS endstation (Beamline 9.3.2) at the Advanced Light Source. (a) Image of the endstation, with key components labeled. (b) Analyzer cone in the analysis chamber, which employs differential pumping.

Chapter 6

Copper migration and surface oxidation of the topological insulator $Cu_xBi_2Se_3$

6.1 Introduction

Chemical intercalation of TIs is the insertion of atoms or molecules between quintuple layers, and is an established strategy for modifying TI properties [53, 149–155] or creating additional electronic phenomena, such as superconductivity with Cu intercalation ($T_{c,\max} \sim 3.5\,\mathrm{K}$) [46–53]. The Cu-intercalated TI Bi_2Se_3 ($Cu_xBi_2Se_3$) is a known superconductor, with $T_{c,\max}$ and the superconducting shielding fraction strongly depending on the intercalated Cu content and preparation method [47–49, 156]. Controlling the Cu content and its variation during and after synthesis is thus important for realizing ideal superconducting properties in $Cu_xBi_2Se_3$.

Intercalated materials may be exposed to air during sample preparation or real world usage, such as in the operation of devices, which may affect composition. For instance, the intercalate guest can diffuse within battery cells left at a fixed potential, and it is known that intercalants can diffuse within and between layers in various compounds. [155, 157–159]. The effect of ambient conditions on intercalant chemistry is not fully understood due to experimental difficulties, despite its practical importance.

In this chapter, we use $Cu_xBi_2Se_3$ as a representative material to establish the effects of controlled ambient environments on evolving chemistry in the near-surface region of intercalated TIs. The near-surface Cu composition was found to increase under both controlled O_2 dosing and ambient air exposure, coincident with the formation and growth of an oxide layer that is strongest in full atmosphere [126]. Lastly, core electron spectroscopy simulations show that our XPS observations are consistent with a sample developing vertical gradient distributions of Cu and Se upon exposure to a controlled O_2 environment. This chapter was adapted from Ref. [126].

6.2 Materials and methods

Synchrotron ambient pressure XPS (AP-XPS) experiments were performed at the Advanced Light Source Beamline 9.3.2 in a photon energy range of $E_{\text{ph}} = 230 - 900\,\text{eV}$, with a spot size of $d \sim 1\,\text{mm}^2$. The core level spectra were collected with a Scienta R4000 HiPP electron analyzer with differential pumping, allowing the sample to remain near ambient pressures during data acquisition [147]. The analysis environment was initially at high vacuum ($\sim 1 \times 10^{-7}\,\text{mbar}$), and then containing O_2 at ambient pressure (0.133 mbar). The measured partial pressure of O_2 is equivalent to the total ambient pressure in the AP-XPS experiment. Longer timescale experiments were performed using a Kratos AXIS Supra$^+$ XPS instrument with a monochromated, unpolarized $E_{\text{ph}} = 1486.6\,\text{eV}$ Al-Kα source.

Samples were cleaved *in situ* with the top post method in the AP-XPS experiment, which is shown in Figure 6.1. The samples for the monochromated Kratos AXIS Supra$^+$ XPS experiments were cleaved *ex situ* with Scotch tape, keeping air exposure under several minutes prior to the initial measurements. ARPES spectra were collected at the Advanced Light Source Beamline 4.0.3 (MERLIN) with $E_{\text{ph}} = 39.2\,\text{eV}$. Core level peaks were identified using binding energy reference values [137].

Bi_2Se_3 samples were grown using the Bridgman method, and were then intercalated with Cu to form $Cu_xBi_2Se_3$ crystals using a solution-based process [160]. Bi_2Se_3 samples were

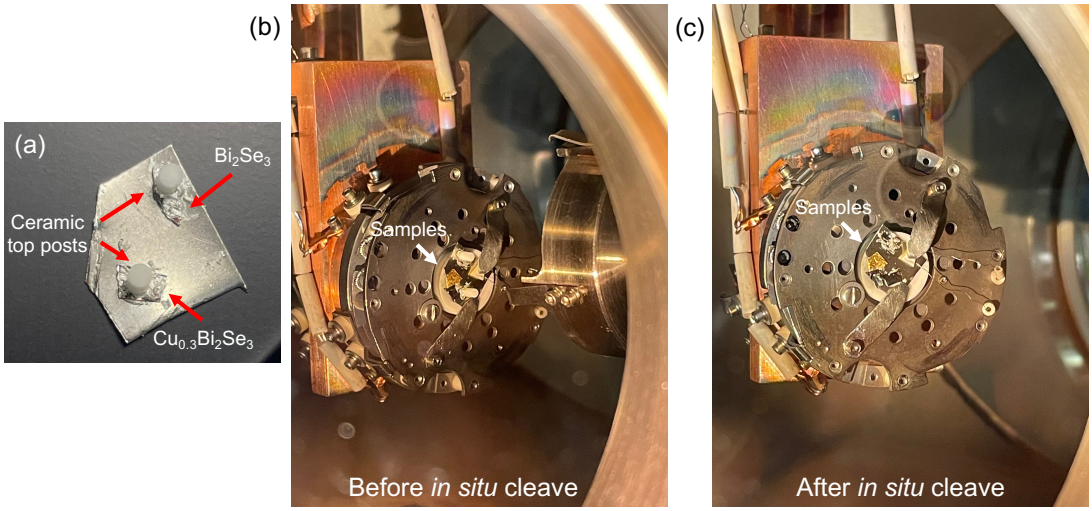

FIGURE 6.1. Images showing the *in situ* cleaving process at ALS Beamline 9.3.2. (a) Ceramic top posts adhered to the sample surfaces with silver epoxy. The samples are adhered to a steel plate, also with silver epoxy, to maintain a conductive path throughout the experiment. (b) Un-cleaved samples with top posts shown in a chamber of the AP-XPS endstation. The gold foil adjacent to the samples is used for obtaining the Au 4f calibration spectra. (c) *In situ*-cleaved samples after removing top posts with the endstation transfer arm (not shown).

grown using a modified form of the Bridgman method [42, 43], starting with pure Bi and Se precursors mixed into an evacuated quartz ampoule in a 2:3 ratio. After melting of the initial mixture, the ampoule was placed into the furnace with a temperature gradient between 750 °C - 650 °C. The ampoule pulled through the gradient at a rate of 2-3 mm h^{-1} forming high purity Bi_2Se_3 at the end of the process. Additional information on the custom furnace at UC Davis is available in Ref. [42]. A solution-based process was used to intercalate the Bi_2Se_3 with Cu to form $Cu_xBi_2Se_3$ [160]. The Bridgman-synthesized Bi_2Se_3 samples were placed in a tetrakisacetonitrile copper hexafluorophosphate solution and heated in 5 mL acetone at 45 °C, just below reflux, for 4 h. Samples were then heated under vacuum at 180 °C for 7.5 min, and the entire sequence was repeated for four cycles.

After synthesis, samples were kept away from moisture during storage to avoid H_2O contamination. Samples were mounted on a conductive substrate with silver epoxy, and

for cleaving in the AP-XPS experiment, ceramic top posts were adhered to the tops of the samples with silver epoxy. A mechanical transfer arm was used to detach the top posts when cleaving *in situ*.

Due to the variation of Cu and Se content highlighted in our study, our convention is to use the nominal bulk stoichiometries after synthesis ($Cu_{0.15}Bi_2Se_3$ and $Cu_{0.3}Bi_2Se_3$) to distinguish between samples in our analysis. No indications of superconductivity were found in these samples, which depend on the details of the synthesis and the intercalation [**49**,**156**,**161**,**162**].

6.3 AP-XPS on $Cu_xBi_2Se_3$

Figure 6.2 provides initial XPS and ARPES characterizations of $Cu_{0.15}Bi_2Se_3$ and $Cu_{0.3}Bi_2Se_3$ at several different photon energies. Fig. 6.2(a) shows a survey spectrum of the core levels accessible with $E_{\text{ph}} = 650\,\text{eV}$ in the AP-XPS experiment. The survey spectrum confirms the quality of the *in situ* cleaved sample, showing peaks for Cu, Bi, and Se. Fig. 6.2(b) shows an ARPES spectrum on an *in situ* cleaved sample, clearly showing the topological surface state and Dirac point at $E_B \sim 0.3\,\text{eV}$, indicating maintenance of crystallinity and topological electronic features after Cu intercalation.

Fig. 6.2(c) shows a diagram of the X-ray photoemission process, indicating the different sample depths accessible with the X-ray photon energies available at the beamline and used for depth profiling. The depths are represented as the electron inelastic mean free path (IMFP) for each photon energy. Fig. 6.2(d) shows the three core levels present in the shallow binding energy region in Fig. 6.2(a): Cu 3p, Se 3d, and Bi 5d, none of which show initial oxidation or hydroxylation. This set of three shallow core levels is sufficient to determine the chemical composition of $Cu_{0.15}Bi_2Se_3$ and $Cu_{0.3}Bi_2Se_3$ throughout the oxidation process using the four different E_{ph}; the relative peak intensities are proportional to the elemental composition after correcting for the relative sensitivity factor (RSF) for each photon energy [**141**, **142**]. To quantify the Cu content, we monitor the binding energy region around $E_B \sim 76\,\text{eV}$ where the Cu 3p doublet is present. All Cu 3p data are measured above the loss feature-containing background (Figs. 6.2(e,f)).

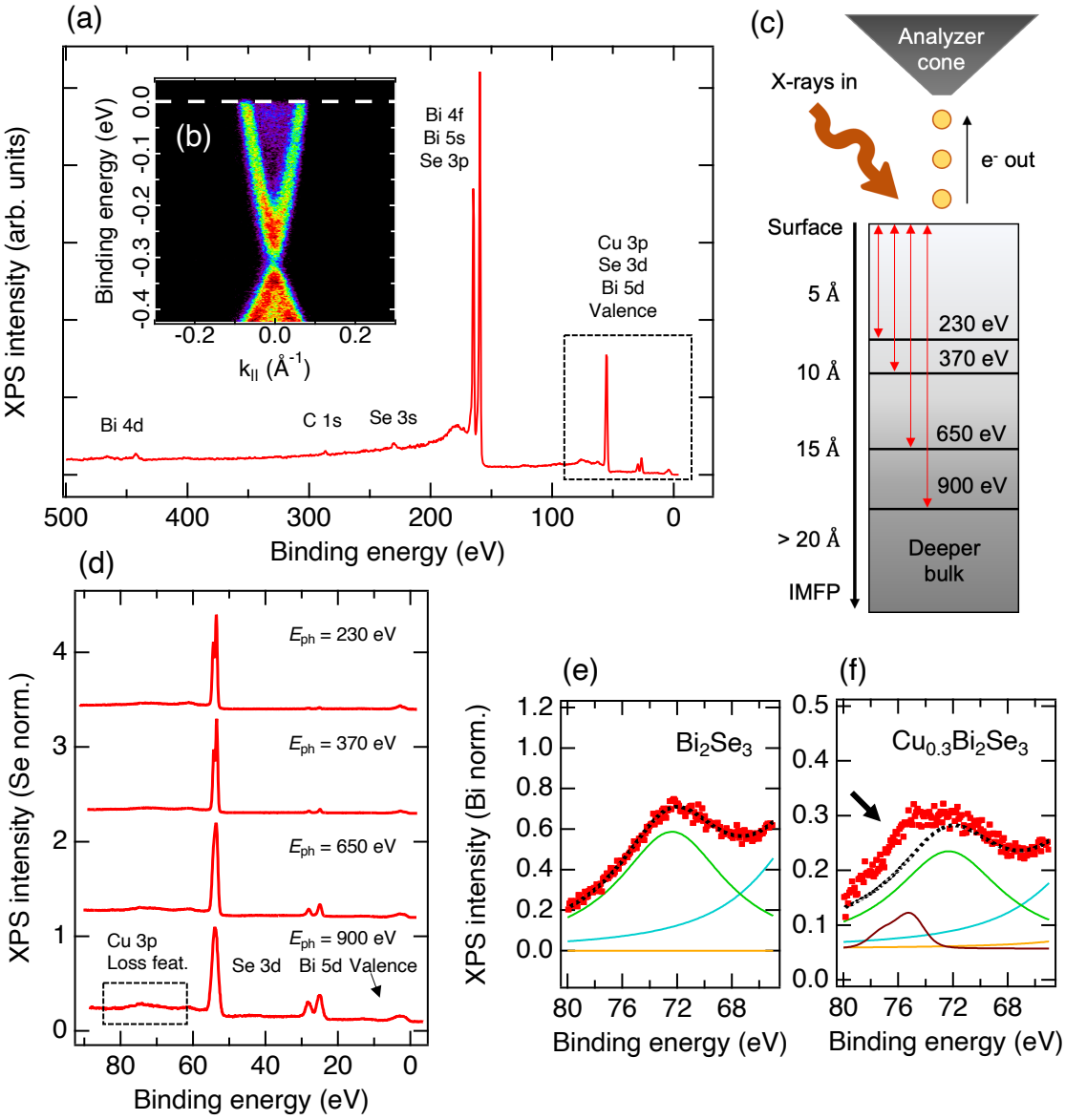

FIGURE 6.2. XPS and ARPES characterizations of freshly cleaved $Cu_{0.15}Bi_2Se_3$ and $Cu_{0.3}Bi_2Se_3$. (a) $Cu_{0.15}Bi_2Se_3$ XPS survey spectrum taken with $E_{ph} = 650\,eV$ in vacuum. Cu, Bi, and Se core levels are labeled, and the shallow core levels analyzed in this work are indicated. The adventitious C 1s peak is also labeled. (b) ARPES spectrum of the topological surface state in $Cu_{0.15}Bi_2Se_3$. (c) Diagram of the XPS photoemission process as a function of the X-ray photon energy, indicating the accessible IMFPs for each energy. (d) Shallow core levels in the dashed box in (a) taken with $E_{ph} = 230\,eV$, 370 eV, 650 eV, and 900 eV in vacuum. For best comparison, spectra are shown normalized to their Se 3d peaks and offset for clarity. (e) Illustration of the loss feature background in a Bi_2Se_3 sample, with the individual plasmon resonances indicated in green and cyan. (f) Corresponding spectrum in $Cu_{0.3}Bi_2Se_3$ showing the Cu 3p peaks (brown curve) and loss feature background, after dosing 0.133 mbar O_2. The black arrow indicates the additional spectral weight from the Cu. The data in (e) and (f) were taken with $E_{ph} = 370\,eV$.

To accurately quantify the Cu content in Fig. 6.2, which is present on top of a relatively large background, we utilize a background correction procedure incorporating the electron energy loss features in the $Cu_{0.3}Bi_2Se_3$ XPS spectrum. The loss features near $E_B \sim 72\,\text{eV}$ (green and cyan curves in Figs. 6.2(e,f)) originate from bulk plasmon resonances in Bi_2Se_3 [**163**]. Since this background is also present in a Bi_2Se_3 reference sample from the same batch (Fig. 6.2(e)), we use the Bi_2Se_3 spectrum from a newly cleaved sample as a reference for fitting to the plasmon losses in the $Cu_{0.3}Bi_2Se_3$ spectrum (Fig. 6.2(f)). After fitting Voigt peaks to the Se 3d peaks and the loss features in the reference spectrum, the result is a background containing the loss features (dashed curve). Fitting this background to the $Cu_{0.3}Bi_2Se_3$ spectrum allows us to isolate the Cu 3p signal intensity, shown as a separate Voigt doublet (brown curve). The areas of the fitted Cu, Se, and Bi peaks then correspond to the total XPS intensity for these elements.

Figure 6.3 shows the main results of the AP-XPS experiment, which track the evolution of the Cu and Se composition from an initial condition with no O_2 dosing, and later times in 0.133 mbar O_2 to simulate ambient atmosphere. The chemical compositions are expressed in terms of the atomic fractions of Cu/Bi and Se/Bi for each time and photon energy, with $x = 2 \times \text{Cu/Bi}$. To determine the atomic fractions, the XPS intensities determined from the peak fitting were weighed by the RSF for each element and photon energy. The atomic fractions are normalized to the Bi peaks since Bi intensities change less compared to Cu and Se in our experiments.

Over the course of the four day experiment, the Cu fraction x increases from $x = 0.13$ to $x = 0.40$ after dosing O_2 for the $E_{\text{ph}} = 900\,\text{eV}$ data, with smaller changes seen at lower, more surface sensitive E_{ph} (Fig. 6.3(a)). The growth of the Cu/Bi ratio is consistent with Cu migrating vertically to the probed surface region of the sample, since the only additional Cu present is deeper within the sample, with no external Cu deposition. This is best seen when expressed versus the IMFP for each photon energy in Fig. 6.3(b), which provides a

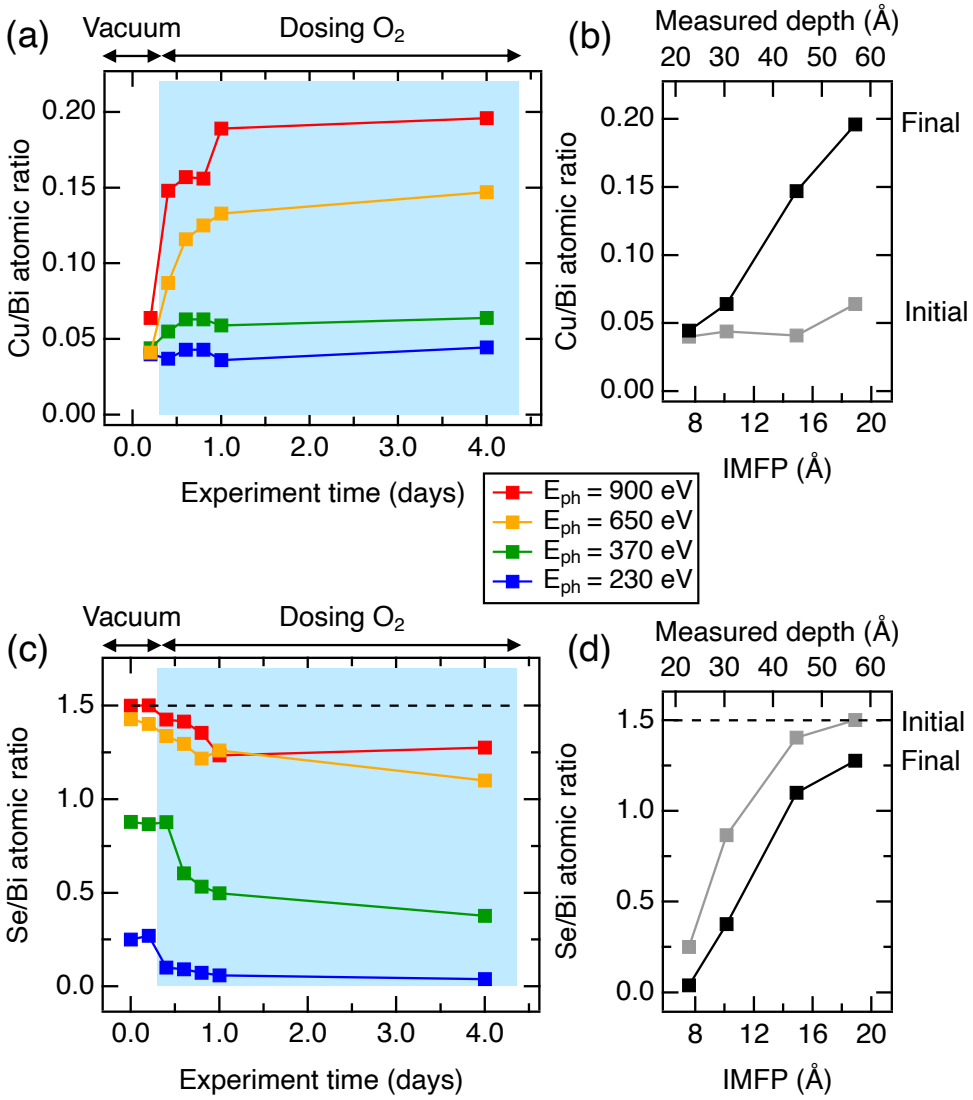

FIGURE 6.3. Evolution of Cu and Se composition in $Cu_{0.3}Bi_2Se_3$ in the AP-XPS experiment. (a) Cu/Bi atomic ratios for four different photon energies, initially in vacuum and after in 0.133 mbar O_2. (b) Initial and final Cu/Bi ratios expressed in terms of the IMFP and the measured depth (3×IMFP) for each E_{ph} as determined from (a). Initial: in vacuum after cleaving. Final: in O_2 for 4 days. (c) Se/Bi atomic ratios for the same photon energies and conditions. Dashed line at Se/Bi = 1.5 indicates the ideal Se/Bi = 3/2 ratio. (d) Initial and final Se/Bi ratios from (c) expressed in terms of IMFP and measured depth.

length scale for the observed Cu migration. The measured depth (3×IMFP) at each photon energy includes depths below one IMFP, which still contribute to the XPS measurement. A

similar plot of the Se/Bi fraction is shown in Fig. 6.3(c), showing a steady decrease in Se/Bi at all E_{ph} after dosing O_2, decreasing from the ideal Se/Bi = 3/2 fraction of Bi_2Se_3. There are large differences in the initial and final Se/Bi fractions for the different E_{ph}, implying a large variation in the Se distribution, with the bulk rich in Se and the surface deficient in Se (Fig. 6.3(d)). Between one and four days in the AP-XPS chamber, the changes to Cu/Bi and Se/Bi are less pronounced than those that happen immediately after dosing O_2.

6.4 AP-XPS in a mixed O_2/H_2O environment

Similar trends are also observed in a mixed O_2/H_2O environment. Here, separate AP-XPS experiments were performed in a mixed O_2/H_2O environment (100 mTorr/20 mTorr) showing a similar increase in Cu/Bi and decrease in Se/Bi consistent with the O_2 experiment (Fig. 6.4). At 10 h after measurements began, 20 mTorr H_2O was introduced into the chamber. At 20 h, the sample was heated to 80 °C from room temperature. The growth of the Cu 3p peaks can be expressed as loss feature-corrected spectra at different times in Fig. 6.4(a) and in terms of the atomic fraction Cu/Bi (Fig. 6.4(b)). The decrease in the signal-to-noise ratio over time in Fig. 6.4(a) is indicative of increased Cu content being measured at later times.

The XPS spectrum of the same $Cu_{0.15}Bi_2Se_3$ sample was collected with the Kratos AXIS SUPRA$^+$ (E_{ph} = 1486.6 eV) after 1 month and 24 days of aging in air. Shown in Figure 6.5, the Cu 3p peaks and the Se and Bi oxide peaks are considerably larger after extended air exposure. We note the growth of the valence band states in Fig. 6.5(b), which are also consistent with greater Cu near the surface.

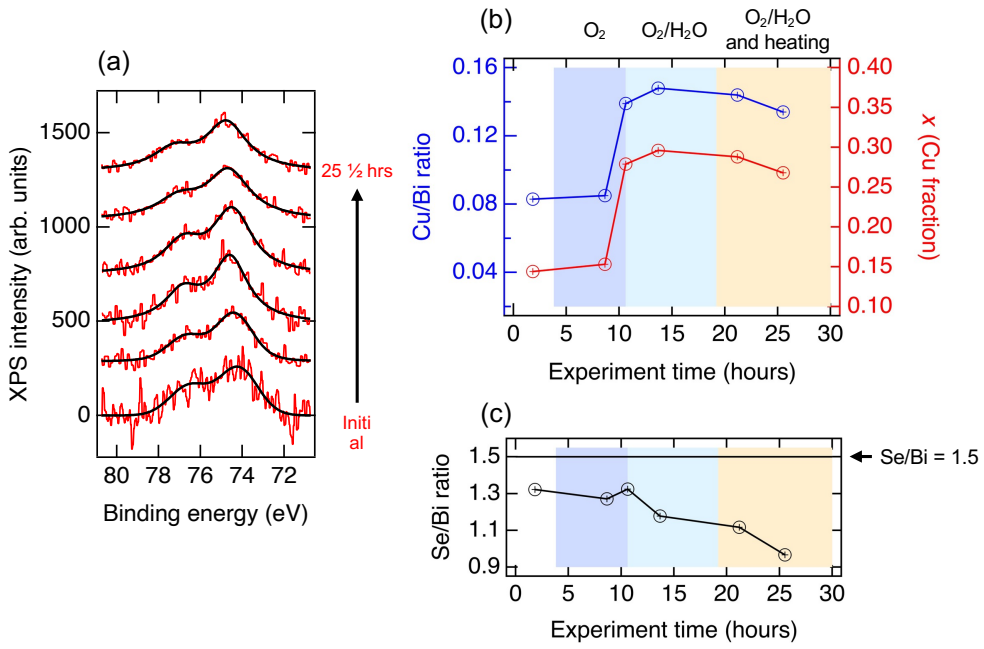

FIGURE 6.4. AP-XPS data for $Cu_{0.15}Bi_2Se_3$ in a mixed O_2/H_2O environment, measured with $E_{ph} = 370\,eV$. (a) Evolution of Cu 3p peaks, after correcting for the loss feature background. (b) Growth of Cu/Bi ratio and Cu fraction x for several conditions: before dosing O_2, dosing O_2, dosing mixed O_2/H_2O, and heating when dosing O_2/H_2O. (c) Decrease of Se/Bi ratio for the same conditions.

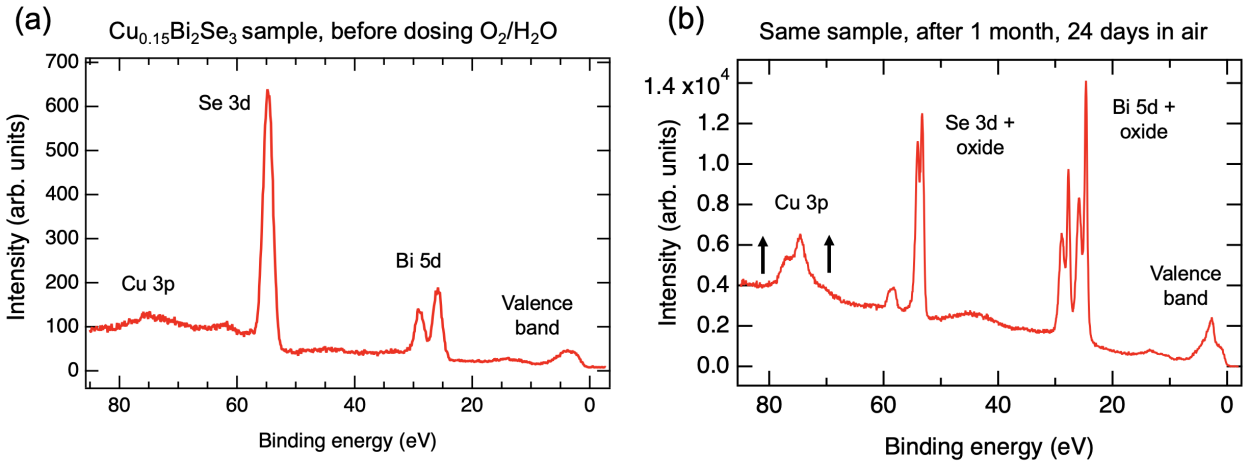

FIGURE 6.5. $Cu_{0.15}Bi_2Se_3$ sample after oxidation in air. (a) Shallow core levels including the valence band measured with $E_{ph} = 900\,eV$, prior to any O_2/H_2O dosing. (b) XPS spectrum taken on the same sample after the AP-XPS experiment and 1 month, 24 days in air, using $E_{ph} = 1486.6\,eV$.

6.5 Se depletion and oxidation

In the mixed O_2/H_2O AP-XPS experiments, the $Cu_xBi_2Se_3$ Se 3d peak intensities were observed dropping right after cleaving (Fig. 6.6(a)), and continue to decrease at later times after dosing O_2 and H_2O (Fig. 6.4(c)). These observations show that the Se content is highly volatile even in the earliest moments of handling the sample and when starting O_2 dosing. Due to the lower partial pressure of O_2, no Se oxidation was observed in the AP-XPS experiments, and was not included in subsequent modelling. Se oxidation can be observed, but only in measurements taken after oxidation in full atmosphere for several days. In Fig. 6.6(b), a feature to the higher binding energy side of the Se 3d levels indicates that Se is oxidized, and follows the growth trend shown in Fig. 6.6(c).

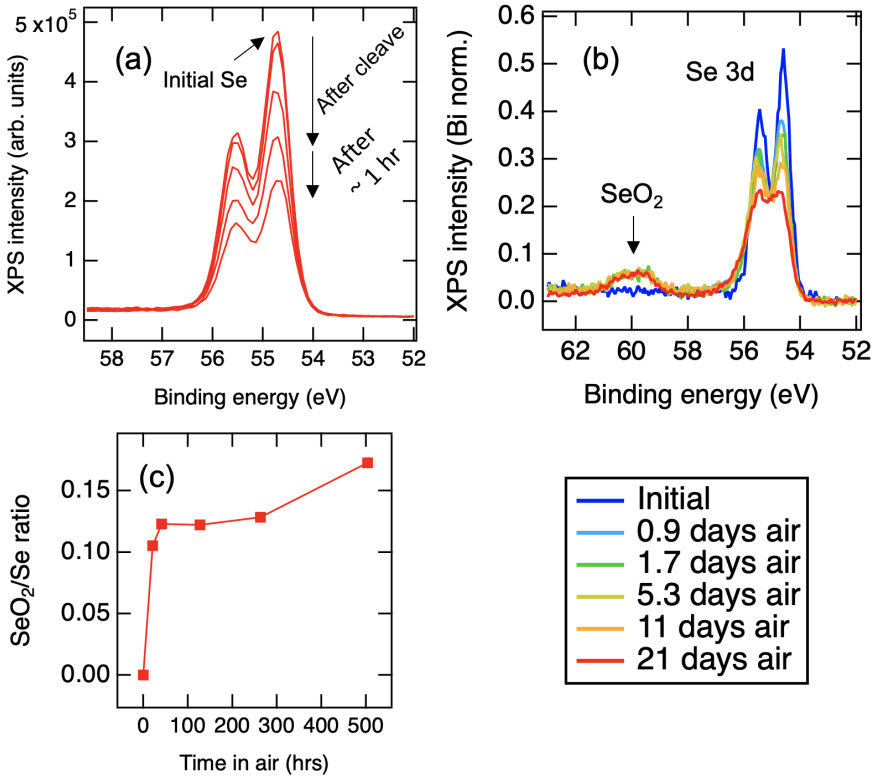

FIGURE 6.6. Se depletion and oxidation in $Cu_{0.15}Bi_2Se_3$. (a) Se depletion after cleaving in the AP-XPS experiment ($E_{ph} = 370\,eV$). (b) Se 3d peaks over several days of oxidation, with SeO_2 visible at higher E_B ($E_{ph} = 1486.6\,eV$). (c) Growth of SeO_2 relative to Se over several days.

Additionally, we have compared the changes in Se content to those in pure, unintercalated Bi_2Se_3. The Se/Bi XPS intensity ratios are plotted in Figure 6.7. After O_2 dosing, Se content decreases. The Se content in Bi_2Se_3 when compared to $Cu_{0.3}Bi_2Se_3$ is initially higher for the lowest photon energies, but consistent with a Se/Bi = 3/2 stoichiometry. The lower initial near-surface Se content in $Cu_{0.3}Bi_2Se_3$ is likely due to differences in the near-surface composition of the $Cu_{0.3}Bi_2Se_3$ arising from chemical intercalation and several heating cycles in the synthesis.

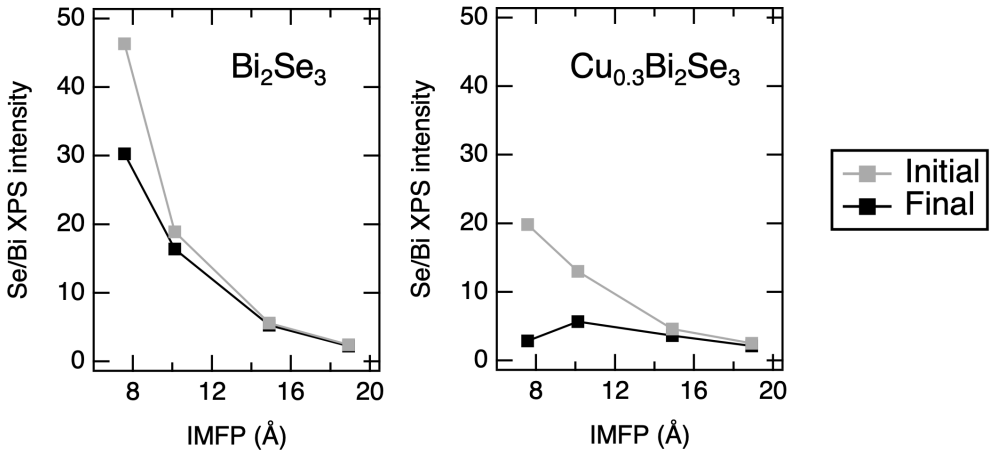

FIGURE 6.7. Se/Bi XPS intensity ratios initially before and after dosing O_2 for Bi_2Se_3 (left) and $Cu_{0.3}Bi_2Se_3$ (right).

6.6 Bi_2Se_3 loss feature correction

This section describes the procedure that was implemented to systematically background-correct the AP-XPS $Cu_xBi_2Se_3$ spectra in the vicinity of the Cu 3p core levels to isolate the Cu 3p intensity. This procedure has the advantage of incorporating the plasmon energy loss features in the $Cu_xBi_2Se_3$ spectra, and is able to discriminate between the small Cu 3p intensity and the loss features for each excitation energy. The background is initially estimated by fitting to Bi_2Se_3 reference spectra at each excitation energy containing the plasmon energy loss features (Fig. 5.5) [**163**]. To model the loss features, several Voigt peaks and a linear background were fit to the reference Bi_2Se_3 spectrum (Figs. 5.5 and

6.2(e)), forming the composite background that was subsequently fitted to the $Cu_xBi_2Se_3$ spectra in Fig. 6.2(f). The peak widths, peak ratios, and energy spacing between individual peaks were fixed, with only the amplitudes varying as a fitting parameter, up to an overall binding energy offset determined by the Se 3d peak. The Cu 3p spectra were fitted to another Voigt doublet to quantify the XPS intensity of Cu 3p.

It is also possible to quantify Cu 3p after directly subtracting a normalized Bi_2Se_3 reference spectrum, which was done for the separate AP-XPS experiment in a mixed O_2/H_2O environment and the experiment in full atmosphere. A similar increasing Cu/Bi trend was seen with this background correction method, shown in Figs. 6.4(a) and Fig. 6.10(a).

6.7 Oxidation in $Cu_xBi_2Se_3$

Figure 6.8 shows the initial and final Bi 5d peaks for all E_{ph} before and after dosing O_2, quantifying the growth of oxides. The initial state peaks are well separated, showing little to no signs of Bi oxidation (Fig. 6.8(a)). After four days in the AP-XPS chamber, chemically-shifted peaks are present for $E_{ph} = 650\,eV, 370\,eV$, and $230\,eV$ (Fig. 6.8(b), dashed colored lines). These changes to the Bi levels directly show the formation of Bi_2O_3 at the surface, which is most dominant at lower E_{ph}. The noise in the initial $E_{ph} = 230\,eV$ spectrum (blue, left) is due to the low photon flux at this particular E_{ph}, which was improved for the final state (blue, right) by extending the measurement time. The large width of the oxide components in the Bi 5d spectra suggest a convolution of several electrostatic (i.e., band bent) or chemically distinctive states, which are most pronounced in the spectrum measured with highest surface sensitivity ($E_{ph} = 230\,eV$). Fig. 6.8(c) quantifies the growth of the Bi_2O_3 peaks relative to the total Bi peak intensity, showing that oxidation starts after dosing O_2, with a larger oxide fraction seen with the more surface-sensitive $E_{ph} = 370\,eV$. When compared to the $E_{ph} = 650\,eV$ data, the overall detected oxide is less and with a more gradual onset due to the lower surface sensitivity of $E_{ph} = 650\,eV$. Interestingly, most of the

oxidation process occurs within the first day and only little change is observed thereafter, as is the case with the Cu and Se changes.

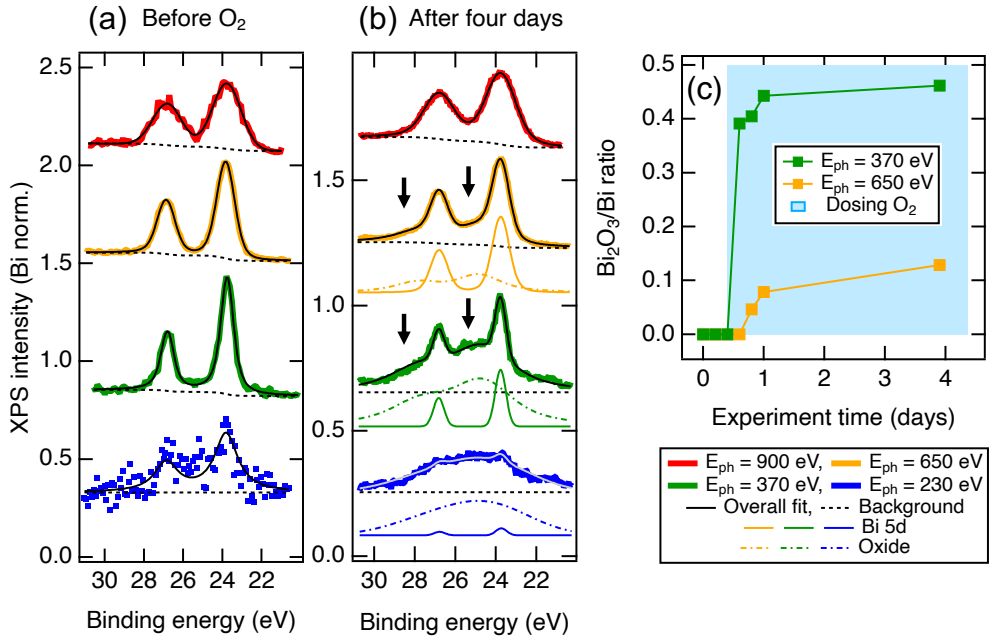

FIGURE 6.8. Oxidation of Bi in $Cu_{0.3}Bi_2Se_3$ in the AP-XPS experiment. (a) Bi 5d levels before dosing O_2 and (b) after four days of oxidation in 0.133 mbar O_2. Solid colored lines indicate the Bi 5d components of the overall fits, and the dashed colored lines indicate the Bi_2O_3 contributions. (c) Bi_2O_3/Bi ratio over the course of the entire experiment for two photon energies. We note that the first point for $E_{ph} = 370$ eV after dosing O_2 does not show oxide yet, as that dataset was collected nearly concurrently with the introduction of O_2 into the chamber.

Additional spectra taken with $E_{ph} = 650$ eV in the AP-XPS experiment shows that the growth of the Bi_2O_3 features is coincident with the growth of the O 1s peak. Initially right after the cleave, adventitious O is adsorbed at the surface, as seen by the non-zero initial O 1s peak (Fig. 6.9, right). After dosing O_2, the O 1s peak steadily grows, reaching the highest intensity at the end of the AP-XPS experiment when the Bi is most oxidized. We note that the O 1s peak is still growing at the end of the AP-XPS experiment, consistent with our longer timescale observations that show continued oxidation over several weeks.

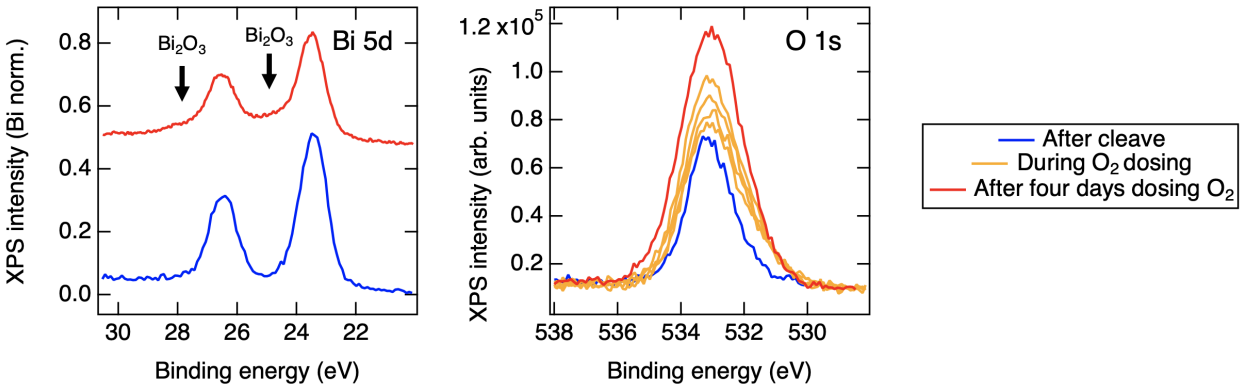

FIGURE 6.9. Oxidation of $Cu_{0.3}Bi_2Se_3$ and O 1s in the AP-XPS experiment, taken with $E_{ph} = 650\,eV$. Left: growth of the Bi 5d levels initially after cleaving and after four days dosing O_2. Bi 5d peaks have been normalized to the total Bi intensity, and offset for clarity. Right: unnormalized O 1s peaks during the AP-XPS experiment.

To gain insight into changes in the $Cu_{0.15}Bi_2Se_3$ composition over longer timescales ($t > 20\,h$), we continue by performing a different set of lab-based *ex situ* cleaved XPS measurements after exposing a $Cu_{0.15}Bi_2Se_3$ sample to full atmosphere in air, with increasing periods of air exposure. The loss feature-corrected spectra for Cu 3p are shown in Fig. 6.10(a), with large changes in the Cu/Bi fraction after exposure to air for multiple days (Fig. 6.10(b)). In Fig. 6.10(c), we again see the oxidation of the surface, with the Bi oxides showing stronger growth over several weeks. The evolution of Bi_2O_3 in Fig. 6.10(d) shows an initial jump after exposure to air for 0.9 days, and continues to grow afterward. Oxidation of Se is also seen (Fig. 6.6(b)), and we note that this sample had a smaller initial Cu concentration than the sample measured with AP-XPS.

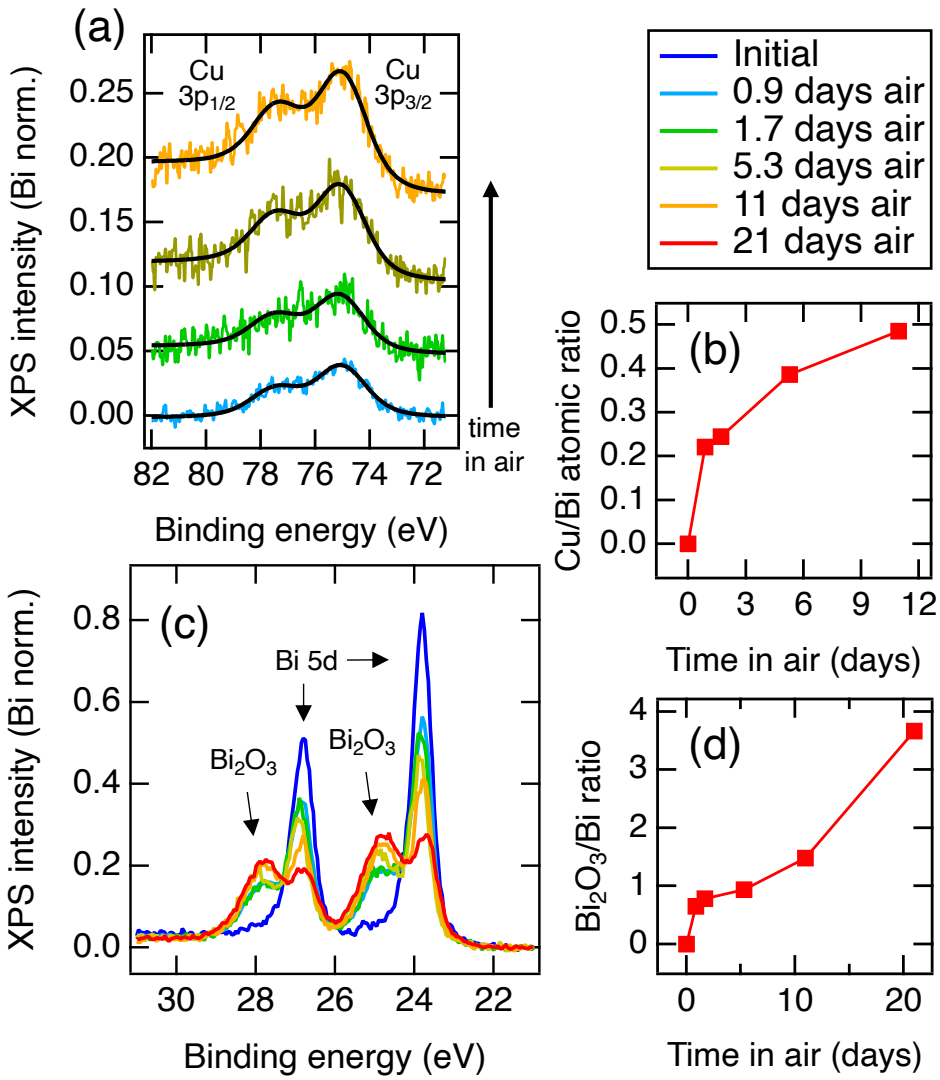

FIGURE 6.10. Growth of Cu 3p and Bi oxidation at longer ($t > 20\,\mathrm{h}$) timescales in $Cu_{0.15}Bi_2Se_3$. (a) Increasing Cu 3p signal over 11 days of air exposure with $E_{\mathrm{ph}} = 1486.6\,\mathrm{eV}$. All Cu 3p spectra are loss feature-corrected and normalized to their total Bi 5d intensities, including oxide peaks. (b) Cu/Bi atomic ratio after air exposure. (c) Evolution of Bi 5d peaks over time, showing the appearance of Bi_2O_3 peaks. (d) Growth of Bi_2O_3/Bi over many days.

6.8 Discussion

Our interpretation of present data is guided by prior studies of pristine Bi_2Se_3 exposed to air and controlled ambient environments. The effects of ambient conditions in regular Bi_2Se_3 have been studied in the following ways with the following conclusions. Exposure to ambient environments has been shown to alter measured ARPES spectra and the surface composition in Bi_2Se_3 [164–167]. The topological surface states can be modified by the formation of 2D quantum well states in ambient conditions [165], and can present band bending and controlled charge-doping after H_2O dosing [164] and UV irradiation [168]. In most cases, the robust topological surface states are still present in Bi_2Se_3 despite air exposure and oxidation [165, 169]. The thinness of the oxide layer and the robustness of the topological surface states are common themes in Bi_2Se_3, including the persistence of surface states in intercalated samples [159, 170], with some works not reporting any surface reactivity [171,172]. Still, the surface chemistry in Bi_2Se_3 remains an open question, particularly after intercalation.

To begin the discussion of our results, we first turn to the observations seen in the AP-XPS experiment. The main result in Fig. 6.3 shows that the increase in the Cu 3p peak intensity over the course of the experiment is coincident with the introduction of O_2 gas, demonstrating that Cu migrates to the surface region during the measurement. This behavior has not been previously reported or quantified in a topological insulator with XPS, although some indications of Cu near the surface have been reported with STM imaging after cleaving [47], and in electrochemically intercalated $Cu_xBi_2Se_3$ [155].

The measured depth in XPS is mainly limited by the IMFP of escaped electrons at each E_{ph}, so measurement with several different E_{ph} to vary IMFP allows one to obtain a depth profile of the elements in the sample. Between the photon energy range $E_{\mathrm{ph}} = 230 - 900\,\mathrm{eV}$ in $Cu_{0.3}Bi_2Se_3$, the IMFP of Cu 3p photoelectrons ranges from $7.6 - 18.9\,\mathrm{Å}$, calculated in QUASES using the TPP2M algorithm [143].

Measured XPS intensities generally follow an exponential form for attenuation [131]:

$$dI = I_0 \cdot X(z) \cdot e^{-z/\lambda \cos(\theta)} dz \tag{6.1}$$

with a total emitted photoelectron intensity I_0, vertical depth z, atomic fraction $X(z)$ at each depth z, the IMFP λ, and the photoelectron collection angle θ from the surface normal. From Eq. 6.1, the measured intensity is $I \approx 0.95 I_0$ within three IMFPs below the surface, providing an upper limit for the measured depth. Fig. 6.3(b) shows the initial and final distributions of Cu/Bi as a function of IMFP and the measured depth ($3 \times$ IMFP) in the AP-XPS experiment (black and gray solid lines), showing the growth of Cu from deeper within the sample. The greatest Cu increase is at an IMFP of 18.9 Å, which corresponds to Cu migrating into the top 6 nm surface region of the sample.

We note that the observed Cu migration is very small when measured with $E_{\text{ph}} = 230$ eV, which is indicative of change in the Cu concentration within the topmost layers of the sample due to the surface bismuth oxide. The beamline photon flux is also considerably lower at $E_{\text{ph}} = 230$ eV, which can contribute to measurement error.

Another notable observation is the decrease in Se content relative to Bi in Fig. 6.3(c) over the course of the AP-XPS experiment. Initially after cleaving (that is, prior to the first data points in Fig. 6.3(c)), the Se 3d intensity is already reduced, and continues to drop over the course of the experiment from the ideal Se/Bi = 3/2. The initial distribution of Se when expressed versus IMFP in Fig. 6.3(d) shows that the uppermost 2 nm (2 quintuple layers) is deficient in Se, while the uppermost 6 nm (6 quintuple layers) is richer in Se and representative of bulk stoichiometric Bi_2Se_3. After four days in O_2, Se/Bi decreases at all depths.

The observation of a long Se gradient with minimal Se at the surface is consistent with the well known volatility of Se in Bi_2Se_3. Bi_2Se_3 generally has selenium vacancies which make samples naturally n-type without further chemical compensation. [18, 25, 76, 164, 165, 173–

176]. However, our results indicate that these selenium vacancies may be more concentrated near the surface, and the deeper bulk is closer to nominal stoichiometry. The pure Bi_2Se_3 reference sample also shows a decrease in Se after dosing O_2, and with the decrease being more significant at the surface (Fig. 6.7). The Fermi level E_F in the ARPES spectrum in Fig. 6.2(b) intersects the bulk conduction band, confirming that this specimen is n-type at the surface region, with an IMFP of 4.9 Å for $E_{\text{ph}} = 39.2\,\text{eV}$ calculated in QUASES. Cu doping is also known to shift the chemical potential further into the bulk conduction band [**176**].

A prior XPS/AFM study has observed small Bi islands that appear within one hour after cleaving [**166**], which is also consistent with decreasing Se/Bi in Fig. 6.3(c), suggesting that some Bi migration could also be occurring along with Cu. However, the larger increases in Cu/Bi we see suggest that any Bi migration would be very small, below the sensitivity of a standard XPS instrument [**166**] and indistinguishable from Bi oxides at the surface.

While Cu migration can be seen on shorter timescales, the process continues and is more easily seen at the longer timescales ($t > 25\,\text{h}$) in Fig. 6.10(a). On these timescales the oxidation of the near-surface Bi is evident with new oxide peaks, consistent with prior work [**18**, **166**] and the oxide peaks we see during the AP-XPS experiment in Fig. 6.8. The oxidation is stronger and continues for longer in full atmosphere ($P = 1013.25\,\text{mbar}$) than in the AP-XPS experiment ($P = 0.133\,\text{mbar}$), even when considering the deeper probing depth of the $E_{\text{ph}} = 1486.6\,\text{eV}$ Al-Kα source (IMFP = 28.9 Å). The oxidation is accompanied by a steady increase in Cu 3p over several days (Fig. 6.10(b)), greater than what was observed in AP-XPS. The link between oxidation and Cu migration is clear when looking at the trends in Figs. 6.3, 6.8, 6.10: both Cu migration and Bi_2O_3 formation start right after dosing O_2, and when oxide growth slows between 1-4 days, Cu growth also slows, changing only slightly. This suggests that surface oxides establish the conditions needed for Cu to diffuse towards the surface. Our observations in Fig. 6.10 suggest that surface oxidation and Cu migration continue slowly for months in air, until the oxidation becomes self-limiting.

6.9 Additional Cu migration data and discussion

At higher photon energy ($E_{\text{ph}} = 1486.6\,\text{eV}$) using the Kratos AXIS SUPRA$^+$, several higher binding energy Cu, Bi, and O levels are observable in the survey spectra: Cu $2p_{3/2}$, Cu $2p_{1/2}$ ($E_B = 932.7, 952.3\,\text{eV}$), Bi 4s ($E_B = 939\,\text{eV}$), and O KL23L23, KL1L23 Auger peaks ($E_B = 970.6, 990.1\,\text{eV}$). These are shown in Figure 6.11. The Cu 2p levels near $E_B = 933 - 952\,\text{eV}$ are more intense than Cu 3p and generally preferable for quantifying Cu, CuO, and Cu_2O. However, tracking Cu 3p is needed over Cu 2p due to the strong overlapping Bi 4s level at $E_B = 939\,\text{eV}$, so only a qualitative analysis of the XPS spectra is possible. Nevertheless, separate observations also show that the Cu 2p levels increase in intensity after exposing $Cu_{0.15}Bi_2Se_3$ samples to air for several weeks, simultaneously with the growing Cu 3p levels.

Freshly cleaved $Cu_{0.15}Bi_2Se_3$ shows only a small Bi 4s peak in Fig. 6.11(a), with no Cu 2p or O Auger peaks. After 20 h in air in Fig. 6.11(b), Cu 2p peaks appear, consistent with the increase in the Cu 3p peaks at $E_B = 76\,\text{eV}$ after 20 h. The O Auger peaks also appear, which indicate surface oxidation. After 163 h in Fig. 6.11(c), the Cu 2p peaks continue to grow relative to the O Auger peak (larger blue arrows) demonstrating that Cu migration continues on the timescale as seen with Cu 3p. Interestingly, a small peak on the higher binding energy side of Cu $2p_{1/2}$ forms after 2 months in Fig. 6.11(d), which is not observed in a similarly oxidized Bi_2Se_3 sample. This peak is consistent with a CuO shakeup peak or a different oxidation state of Cu, indicating that a small amount of Cu probably oxidizes after many weeks of air exposure.

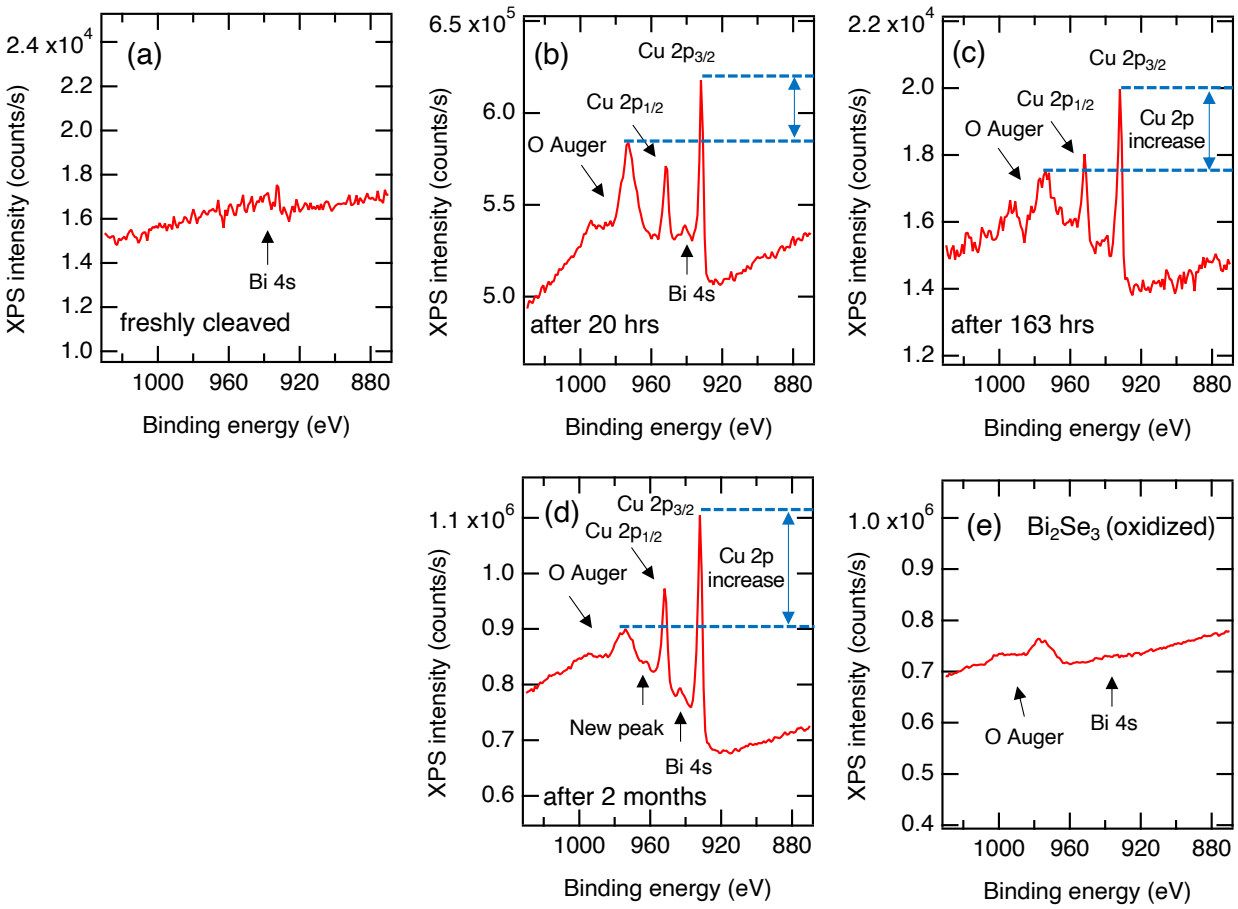

FIGURE 6.11. XPS spectra showing Bi 4s and Cu 2p core levels, taken with $E_{\mathrm{ph}} = 1486.6\,\mathrm{eV}$. (a) XPS spectrum of a freshly cleaved $Cu_{0.15}Bi_2Se_3$ sample, showing a small Bi 4s peak and no visible Cu 2p peaks. (b) Spectrum of $Cu_{0.15}Bi_2Se_3$ after 20 hrs in air. Note the appearance of Cu 2p peaks, and O Auger peaks. The difference between the O Auger feature peak and the Cu $2p_{3/2}$ peak is indicated by the spacing between the blue dashed lines. (c) Spectrum of $Cu_{0.15}Bi_2Se_3$ after 163 hrs, showing growth of the Cu 2p peaks relative to the O Auger peaks (longer blue arrow). (d) Spectrum of $Cu_{0.15}Bi_2Se_3$ after 2 months, showing further growth of the Cu 2p peaks. (e) Spectrum of a Bi_2Se_3 sample kept in air for several months, for comparison.

There are several microscopic mechanisms that can promote Cu migration, such as a surface work function mismatch between Bi_2O_3 and $Cu_xBi_2Se_3$ which can drive the Cu to the surface with a built-in E-field. The work function difference between Bi_2O_3 and Bi_2Se_3 is estimated to be $\sim 1.6\,\text{eV}$ [177, 178], which would create a sufficiently large E-field near the surface. Cu is able to occupy five different sites in the Van der Waals gap and in interstitial vacancies [175, 176], and some migration could be driven by Cu diffusion among these sites. Occupation of surface Se vacancies by Cu could also influence the Cu migration to the surface, which is possible due to the amphoteric character of Cu impurities in Bi_2Se_3 [179]. It is likely that Cu migration can happen for different intercalation and synthesis methods, and Cu migration has been previously observed in electrochemically intercalated $Cu_xBi_2Se_3$ [155], but the details of the phenomenon may vary depending on the synthesis method.

6.10 SESSA simulations of AP-XPS intensities

To connect the proposed changes in chemical composition to the measured XPS intensities, we model our experimental results with core electron spectroscopy simulations using the National Institute of Standards and Technology (NIST) Simulation of Electron Spectra for Surface Analysis (SESSA) software/database [180, 181]. SESSA can accurately simulate XPS spectra and peak intensities for different experimental conditions, geometries, and sample compositions using database reference values. As shown by our experimental observations, Cu and Se form compositional gradients in the near-surface region of the material. A gradient structure consisting of several discretized, homogeneous layers with varying Cu, Bi, and Se compositions models a sample with Cu and Se gradients, shown in Figs. 6.12(a,b). The gradients are selected to have a $X(Z) = Ae^{-Z/L}+B$ falloff when approaching the surface, with fitting parameters A, L, and B, which were selected to match the boundary conditions observed in the experiment. The initial Cu distribution is assumed to be constant. Due to the oxidation present after O_2 dosing, the final simulated structure is capped with a thin $2\,\text{Å}$ overlayer of Bi_2O_3. Physical representations of the final simulated structures are shown

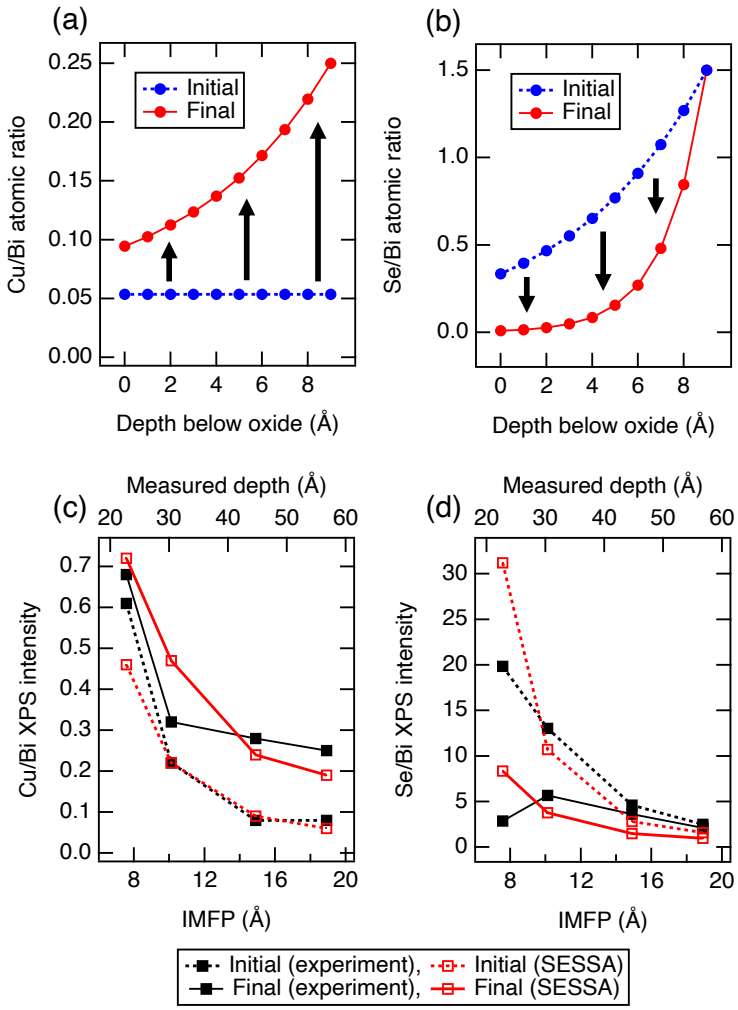

FIGURE 6.12. SESSA modelling of surface compositional gradients in $Cu_xBi_2Se_y$. (a) Proposed Cu distributions for the initial state (before dosing O_2) and the final state (after dosing O_2 for four days) at different depths below the bismuth oxide layer. The initial Cu distribution is uniform, and the final Cu distribution has developed a Cu gradient with a 2 Å-thick Bi_2O_3 overlayer. The black arrows are guides to the eye indicating the passage of time. (b) Proposed Se gradients before and after dosing O_2. The final Se distribution has a steeper falloff when nearing the surface, with a 2 Å Bi_2O_3 overlayer. (c) Comparison of the AP-XPS Cu/Bi intensity ratios (black squares) to SESSA simulated intensity ratios (red squares) for the initial and final states. (d) Comparison of the AP-XPS Se/Bi intensity ratios to SESSA simulated intensity ratios.

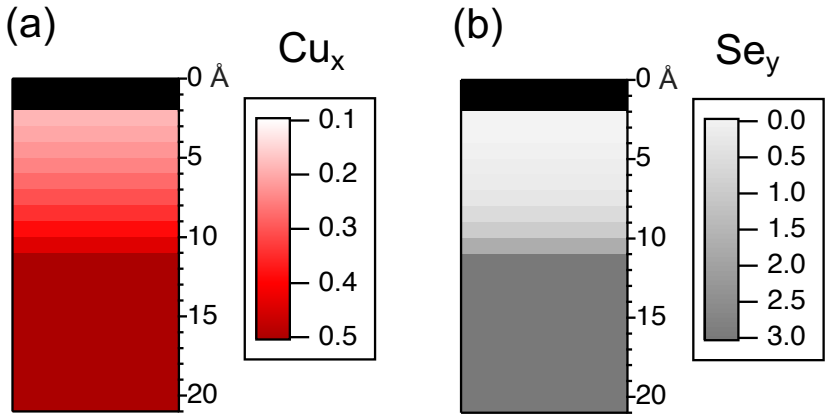

FIGURE 6.13. Final Cu and Se gradient structures modelled in SESSA. (a) Cu gradient for the final state, with a 2 Å-thick Bi_2O_3 overlayer. (b) The final Se gradient, also with a 2 Å-thick Bi_2O_3 overlayer. The Cu and Se fractions are represented as x and y in $Cu_xBi_2Se_y$.

in Figure 6.13. Modelling the topmost 10 Å of $Cu_xBi_2Se_3$ is motivated by the fact that the topmost 10 Å contributes predominately to the measured XPS intensities, as it is on the order of one IMFP. Below the topmost 10 Å, we model the Cu and Se distributions as constant equal to the maximum values of the gradients. Additionally, 10 Å is the approximate thickness of one quintuple layer in Bi_2Se_3, and the van der Waals gap can serve as a barrier to deeper oxidation of the material [**166**]. Thus, it is likely that the oxidation is limited to the uppermost quintuple layer in the AP-XPS experiment, with lesser contributions below.

The red points in Figs. 6.12(c,d) show the SESSA-calculated peak intensity ratios for the initial and final structures, expressed in terms of the Cu/Bi and Se/Bi intensity ratios versus IMFP and the measured depth. The SESSA-calculated intensity ratios are compared to the experimental XPS intensity ratios to confirm agreement between the model and the experimental data. In the initial state, a structure with a single homogeneous Cu composition with no Cu gradient matches closely with the observed constant dependence versus IMFP in Fig. 6.3(b). Initially, no Cu has migrated into the surface region and no oxide has formed yet. In the final state after oxidation, the dual Cu, Se gradient structure agrees

best with our measured XPS intensities in Figs. 6.12(c,d), capturing both the increase in Cu and the decrease in Se near the surface. We note that there is greater error when comparing the gradient to experiment at the smallest IMFP, beacause of the low photon flux at $E_{\mathrm{ph}} = 230\,\mathrm{eV}$.

There are other factors that are not present in this model which can also affect the evolution of $Cu_xBi_2Se_3$ surface chemistry. These include imperfect cleaves that can form step edge sites for oxidation [167], lingering Cu remaining at the surface after the cleave, different Bi, Se surface terminations [173], as well as nanosheet morphology [18, 182]. Other Cu, Se compositional distributions are possible and consistent with our experimental observations, such as ones with discontinuous step edges or sigmoidal distributions. Because of the exponential falloff at greater depths, compositional changes deeper in the sample are more difficult to detect. Thus there may also be less significant compositional changes occurring below the topmost 10 Å, but still within the overall measured depth, which our model does not include.

6.11 Characterization of superconductivity in $Cu_xBi_2Se_3$

To observe any possible indications of superconductivity in $Cu_xBi_2Se_3$, we have measured the DC magnetic susceptibility of a selection of samples using a Quantum Design SQUID Magnetometer (MPMS). During the measurement, the $Cu_xBi_2Se_3$ samples were wedged between multiple straws and oriented so the applied magnetic field was parallel to the crystal c-axis, which was done to limit the diamagnetic background signal.

For a superconducting sample, one would ideally expect a 100% shielding fraction (i.e., $M/H = -1$) in zero field cooled measurements. The M/H vs. T plot shows that none of the studied samples have a significant superconducting shielding fraction ($< 0.3\%$). In prior works, $Cu_xBi_2Se_3$ crystals have been reported to have shielding fractions up to 50% for $x = 0.4$ [49] and up to 56% for $x = 0.35$ [156] and $x = 0.46$ [155]. Another study

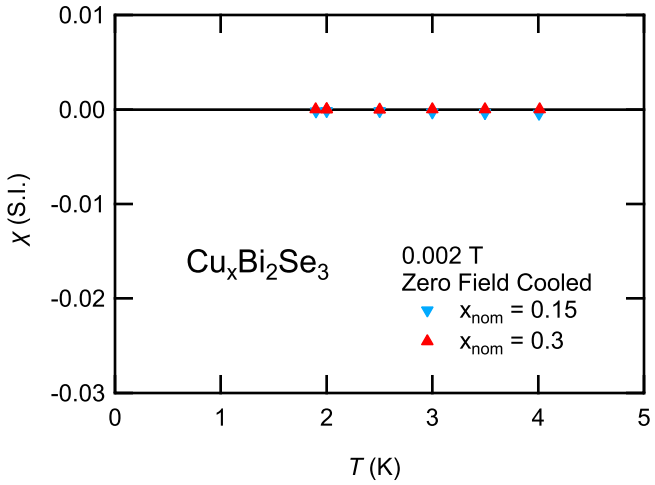

FIGURE 6.14. DC magnetic susceptibility of $Cu_xBi_2Se_3$ samples with nominal Cu fractions $x = 0.15$ and $x = 0.3$, measured down to 1.9 K in a Quantum Design MPMS. No superconducting transition was observed in either sample.

has determined a 17% superconducting shielding fraction after factoring in demagnetization effects [162].

Notably, the shielding fraction can depend on method of synthesis. Melt-growth methods, when quenching from above 560 °C and annealing, are known to produce superconducting samples, while floating zone crystal growth methods do not tend to produce superconducting samples [156]. Electrochemical synthesis also tends to promote superconductivity in $Cu_xBi_2Se_3$ [49]. These examples suggest potential approaches to fully realize superconductivity in Cu-intercalated samples.

6.12 Conclusion

In summary, we have observed an increase in the surface Cu content in the intercalated TI $Cu_xBi_2Se_3$ with ambient-pressure XPS measurements. Our results show that Cu migrates to the surface and is enhanced by the appearance and growth of surface oxides over several days, with the most pronounced changes seen in full atmosphere. Modelling Cu migration

concomitant with Se depletion and oxidation matches our depth-selective XPS observations for a wide range of photon energies.

These findings show that oxidation can be used as an approach for driving chemical species towards the surface of layered intercalated materials, and add additional chemical complexity that must be considered at TI surfaces exposed to ambient conditions. Chemically tailoring the surfaces of topological materials will be needed for realizing real-world environmental applications in chemical sensing, catalysis, and electronics. Most intriguingly, the physical proximity of the topological surface state to the observed chemical changes in $Cu_xBi_2Se_3$ points to further study of the effect of intercalants on the surface states of TIs, particularly on timescales that allow environmental changes to influence them.

Chapter 7

Conclusion and outlook

In summary, results from several spectroscopic studies on the Bi_2Se_3 class of topological insulators have been presented. Ultrafast optical pump-probe spectroscopy has demonstrated novel carrier dynamics in bulk-insulating $Bi_{2-x}Sb_xSe_3$ nanoplatelets that are favorable for the generation of long-lived charge carriers. Fluence- and doping-dependent measurements have identified bimolecular recombination of carriers and possible exciton condensation present in $Bi_{2-x}Sb_xSe_3$. Ambient-pressure XPS has demonstrated that the surface chemistry of $Cu_xBi_2Se_3$ is dynamic and strongly dependent on the external ambient environment, which unambiguously affects the oxidation of the surface and the near-surface Se and Cu composition. Many open questions remain, such as in connecting changes in the Cu and Se surface composition to likely concurrent changes in its electronic band structure that are measurable with ARPES. Additional studies and continuing advances in experimental technique, particularly in synchrotron-based spectroscopy and microscopy, are needed to simultaneously measure both the changes in the electronic structure and the surface chemistry of $Cu_xBi_2Se_3$. Doing so will enable fuller exploration of the aspects of superconducting $Cu_xBi_2Se_3$ that can be useful for developing qubits or other electronic devices.

Topological materials as exemplified by the Bi_2Se_3 class of compounds show great promise both intellectually and for future technological applications. New materials often drive advances in technology, such as silicon and the wide array of semiconductors used in the manufacturing of transistors, solar cells, and LEDs. Topological insulators and the broader family of topological quantum materials are fundamentally new, with their properties not fully understood and technologies based on topological quantum materials in their earliest stages. This underscores the need for using a suite of experimental approaches for synthesis and characterization, where the ultimate goal is to discover the properties of these materials that are useful for new technology.

Bibliography

[1] B. Keimer and J. E. Moore, "The physics of quantum materials," *Nature Physics*, vol. 13, pp. 1045–1055, Oct. 2017.

[2] N. Gedik and I. Vishik, "Photoemission of quantum materials," *Nature Physics*, vol. 13, pp. 1029–1033, Sept. 2017.

[3] K. A. Moler, "Imaging quantum materials," *Nature Materials*, vol. 16, pp. 1049–1052, Oct. 2017.

[4] Y. Tokura, M. Kawasaki, and N. Nagaosa, "Emergent functions of quantum materials," *Nature Physics*, vol. 13, pp. 1056–1068, Sept. 2017.

[5] D. N. Basov, R. D. Averitt, and D. Hsieh, "Towards properties on demand in quantum materials," *Nature Materials*, vol. 16, pp. 1077–1088, Oct. 2017.

[6] N. Samarth, "Quantum materials discovery from a synthesis perspective," *Nature Materials*, vol. 16, pp. 1068–1076, Oct. 2017.

[7] F. Giustino, J. H. Lee, F. Trier, M. Bibes, S. M. Winter, R. Valentí, Y.-W. Son, L. Taillefer, C. Heil, A. I. Figueroa, B. Plaçais, Q. Wu, O. V. Yazyev, E. P. A. M. Bakkers, J. Nygård, P. Forn-Díaz, S. D. Franceschi, J. W. McIver, L. E. F. F. Torres, T. Low, A. Kumar, R. Galceran, S. O. Valenzuela, M. V. Costache, A. Manchon, E.-A. Kim, G. R. Schleder, A. Fazzio, and S. Roche, "The 2021 quantum materials roadmap," *Journal of Physics: Materials*, vol. 3, p. 042006, Oct. 2020.

[8] J. A. Sobota, Y. He, and Z.-X. Shen, "Angle-resolved photoemission studies of quantum materials," *Reviews of Modern Physics*, vol. 93, May 2021.

[9] M. Z. Hasan and C. L. Kane, "Colloquium: Topological insulators," *Reviews of Modern Physics*, vol. 82, pp. 3045–3067, Nov. 2010.

[10] J. E. Moore, "The birth of topological insulators," *Nature*, vol. 464, pp. 194–198, Mar. 2010.

[11] X.-L. Qi and S.-C. Zhang, "The quantum spin Hall effect and topological insulators," *Physics Today*, vol. 63, pp. 33–38, Jan. 2010.

[12] X.-L. Qi and S.-C. Zhang, "Topological insulators and superconductors," *Reviews of Modern Physics*, vol. 83, pp. 1057–1110, Oct. 2011.

[13] Y. Ando, "Topological insulator materials," *Journal of the Physical Society of Japan*, vol. 82, p. 102001, Oct. 2013.

[14] Y. Ando and L. Fu, "Topological crystalline insulators and topological superconductors: From concepts to materials," *Annual Review of Condensed Matter Physics*, vol. 6, pp. 361–381, Mar. 2015.

[15] T. Wehling, A. Black-Schaffer, and A. Balatsky, "Dirac materials," *Advances in Physics*, vol. 63, pp. 1–76, Jan. 2014.

[16] B. Seradjeh, J. E. Moore, and M. Franz, "Exciton condensation and charge fractionalization in a topological insulator film," *Physical Review Letters*, vol. 103, Aug. 2009.

[17] I. Garate and M. Franz, "Inverse spin-galvanic effect in the interface between a topological insulator and a ferromagnet," *Physical Review Letters*, vol. 104, Apr. 2010.

[18] D. Kong, Y. Chen, J. J. Cha, Q. Zhang, J. G. Analytis, K. Lai, Z. Liu, S. S. Hong, K. J. Koski, S.-K. Mo, Z. Hussain, I. R. Fisher, Z.-X. Shen, and Y. Cui, "Ambipolar field effect in the ternary topological insulator $(Bi_xSb_{1-x})_2Te_3$ by composition tuning," *Nature Nanotechnology*, vol. 6, pp. 705–709, Oct. 2011.

[19] H. Peng, W. Dang, J. Cao, Y. Chen, D. Wu, W. Zheng, H. Li, Z.-X. Shen, and Z. Liu, "Topological insulator nanostructures for near-infrared transparent flexible electrodes," *Nature Chemistry*, vol. 4, pp. 281–286, Feb. 2012.

[20] D. Pesin and A. H. MacDonald, "Spintronics and pseudospintronics in graphene and topological insulators," *Nature Materials*, vol. 11, pp. 409–416, Apr. 2012.

[21] C. Kastl, C. Karnetzky, H. Karl, and A. W. Holleitner, "Ultrafast helicity control of surface currents in topological insulators with near-unity fidelity," *Nature Communications*, vol. 6, Mar. 2015.

[22] Z. Jiang, C.-Z. Chang, M. R. Masir, C. Tang, Y. Xu, J. S. Moodera, A. H. MacDonald, and J. Shi, "Enhanced spin seebeck effect signal due to spin-momentum locked topological surface states," *Nature Communications*, vol. 7, May 2016.

[23] Z. Yue, G. Xue, J. Liu, Y. Wang, and M. Gu, "Nanometric holograms based on a topological insulator material," *Nature Communications*, vol. 8, May 2017.

[24] Y. Wang, D. Zhu, Y. Wu, Y. Yang, J. Yu, R. Ramaswamy, R. Mishra, S. Shi, M. Elyasi, K.-L. Teo, Y. Wu, and H. Yang, "Room temperature magnetization switching in topological insulator-ferromagnet heterostructures by spin-orbit torques," *Nature Communications*, vol. 8, Nov. 2017.

[25] Y. Hou, R. Wang, R. Xiao, L. McClintock, H. C. Travaglini, J. P. Francia, H. Fetsch, O. Erten, S. Y. Savrasov, B. Wang, A. Rossi, I. Vishik, E. Rotenberg, and D. Yu, "Millimetre-long transport of photogenerated carriers in topological insulators," *Nature Communications*, vol. 10, Dec. 2019.

[26] Y. Hou, R. Xiao, S. Li, L. Wang, and D. Yu, "Nonlocal chemical potential modulation in topological insulators enabled by highly mobile trapped charges," *ACS Applied Electronic Materials*, vol. 2, pp. 3436–3442, Sept. 2020.

[27] C. Kane, "Topological band theory and the $\mathbb{Z}_2$ invariant," in *Contemporary Concepts of Condensed Matter Science*, pp. 3–34, Elsevier, 2013.

[28] J. E. Moore, "Theory of three-dimensional topological insulators," in *Contemporary Concepts of Condensed Matter Science*, pp. 35–57, Elsevier, 2013.

[29] M. Z. Hasan, S.-Y. Xu, and M. Neupane, "Topological insulators, topological Dirac semimetals, topological crystalline insulators, and topological Kondo insulators," in *Topological Insulators*, pp. 55–100, Wiley, Feb. 2015.

[30] M. G. Vergniory, B. J. Wieder, L. Elcoro, S. S. P. Parkin, C. Felser, B. A. Bernevig, and N. Regnault, "All topological bands of all nonmagnetic stoichiometric materials," *Science*, vol. 376, May 2022.

[31] H. Zhang, C.-X. Liu, X.-L. Qi, X. Dai, Z. Fang, and S.-C. Zhang, "Topological insulators in Bi_2Se_3, Bi_2Te_3 and Sb_2Te_3 with a single Dirac cone on the surface," *Nature Physics*, vol. 5, pp. 438–442, May 2009.

[32] H. Weng, R. Yu, X. Hu, X. Dai, and Z. Fang, "Quantum anomalous Hall effect and related topological electronic states," *Advances in Physics*, vol. 64, pp. 227–282, May 2015.

[33] D. Hsieh, Y. Xia, D. Qian, L. Wray, J. H. Dil, F. Meier, J. Osterwalder, L. Patthey, J. G. Checkelsky, N. P. Ong, A. V. Fedorov, H. Lin, A. Bansil, D. Grauer, Y. S. Hor, R. J. Cava, and M. Z. Hasan, "A tunable topological insulator in the spin helical Dirac transport regime," *Nature*, vol. 460, pp. 1101–1105, July 2009.

[34] P. Corbae, S. Ciocys, D. Varjas, E. Kennedy, S. Zeltmann, M. Molina-Ruiz, S. M. Griffin, C. Jozwiak, Z. Chen, L.-W. Wang, A. M. Minor, M. Scott, A. G. Grushin, A. Lanzara, and F. Hellman, "Observation of spin-momentum locked surface states in amorphous Bi_2Se_3," *Nature Materials*, vol. 22, pp. 200–206, Jan. 2023.

[35] P. Roushan, J. Seo, C. V. Parker, Y. S. Hor, D. Hsieh, D. Qian, A. Richardella, M. Z. Hasan, R. J. Cava, and A. Yazdani, "Topological surface states protected from backscattering by chiral spin texture," *Nature*, vol. 460, pp. 1106–1109, Aug. 2009.

[36] A. A. Taskin, S. Sasaki, K. Segawa, and Y. Ando, "Manifestation of topological protection in transport properties of epitaxial Bi_2Se_3 thin films," *Physical Review Letters*, vol. 109, Aug. 2012.

[37] S. Kim, S. Yoshizawa, Y. Ishida, K. Eto, K. Segawa, Y. Ando, S. Shin, and F. Komori, "Robust protection from backscattering in the topological insulator $Bi_{1.5}Sb_{0.5}Te_{1.7}Se_{1.3}$," *Physical Review Letters*, vol. 112, Apr. 2014.

[38] Y. Xia, D. Qian, D. Hsieh, L. Wray, A. Pal, H. Lin, A. Bansil, D. Grauer, Y. S. Hor, R. J. Cava, and M. Z. Hasan, "Observation of a large-gap topological-insulator class with a single Dirac cone on the surface," *Nature Physics*, vol. 5, pp. 398–402, May 2009.

[39] Y. L. Chen, J. G. Analytis, J.-H. Chu, Z. K. Liu, S.-K. Mo, X. L. Qi, H. J. Zhang, D. H. Lu, X. Dai, Z. Fang, S. C. Zhang, I. R. Fisher, Z. Hussain, and Z.-X. Shen, "Experimental realization of a three-dimensional topological insulator, Bi_2Te_3," vol. 325, pp. 178–181, July 2009.

[40] S. Souma, K. Kosaka, T. Sato, M. Komatsu, A. Takayama, T. Takahashi, M. Kriener, K. Segawa, and Y. Ando, "Direct measurement of the out-of-plane spin texture in the Dirac-cone surface state of a topological insulator," *Physical Review Letters*, vol. 106, May 2011.

[41] D. Hsieh, D. Qian, L. Wray, Y. Xia, Y. S. Hor, R. J. Cava, and M. Z. Hasan, "A topological Dirac insulator in a quantum spin Hall phase," *Nature*, vol. 452, pp. 970–974, Apr. 2008.

[42] D. M. Nisson, *Nuclear Magnetic Resonance Studies of Topological Insulators and Materials with a Large Spin-Orbit Coupling*. PhD thesis, University of California, Davis, 2015.

[43] P. W. Bridgman, "Certain physical properties of single crystals of tungsten, antimony, bismuth, tellurium, cadmium, zinc, and tin," *Proceedings of the American Academy of Arts and Sciences*, vol. 60, no. 6, p. 305, 1925.

[44] W. Ko, I. Jeon, H. W. Kim, H. Kwon, S.-J. Kahng, J. Park, J. S. Kim, S. W. Hwang, and H. Suh, "Atomic and electronic structure of an alloyed topological insulator, $Bi_{1.5}Sb_{0.5}Te_{1.7}Se_{1.3}$," *Scientific Reports*, vol. 3, Sept. 2013.

[45] M. Sharma and D. Mishra, "*CrysX*: crystallographic tools for the Android platform," *Journal of Applied Crystallography*, vol. 52, pp. 1449–1454, Oct. 2019.

[46] L. A. Wray, S.-Y. Xu, Y. Xia, Y. S. Hor, D. Qian, A. V. Fedorov, H. Lin, A. Bansil, R. J. Cava, and M. Z. Hasan, "Observation of topological order in a superconducting doped topological insulator," *Nature Physics*, vol. 6, pp. 855–859, Sept. 2010.

[47] Y. S. Hor, A. J. Williams, J. G. Checkelsky, P. Roushan, J. Seo, Q. Xu, H. W. Zandbergen, A. Yazdani, N. P. Ong, and R. J. Cava, "Superconductivity in $Cu_xBi_2Se_3$ and its implications for pairing in the undoped topological insulator," *Physical Review Letters*, vol. 104, Feb. 2010.

[48] S. Sasaki, M. Kriener, K. Segawa, K. Yada, Y. Tanaka, M. Sato, and Y. Ando, "Topological superconductivity in $Cu_xBi_2Se_3$," *Physical Review Letters*, vol. 107, Nov. 2011.

[49] M. Kriener, K. Segawa, Z. Ren, S. Sasaki, S. Wada, S. Kuwabata, and Y. Ando, "Electrochemical synthesis and superconducting phase diagram of $Cu_xBi_2Se_3$," *Physical Review B*, vol. 84, Aug. 2011.

[50] T. Das, S. Bhattacharyya, B. P. Joshi, A. Thamizhavel, and S. Ramakrishnan, "Direct evidence of intercalation in a topological insulator turned superconductor," *Materials Letters*, vol. 93, pp. 370–373, Feb. 2013.

[51] K. Matano, M. Kriener, K. Segawa, Y. Ando, and G.-Q. Zheng, "Spin-rotation symmetry breaking in the superconducting state of $Cu_xBi_2Se_3$," *Nature Physics*, vol. 12, pp. 852–854, May 2016.

[52] S. Yonezawa, K. Tajiri, S. Nakata, Y. Nagai, Z. Wang, K. Segawa, Y. Ando, and Y. Maeno, "Thermodynamic evidence for nematic superconductivity in $Cu_xBi_2Se_3$," *Nature Physics*, vol. 13, pp. 123–126, Oct. 2016.

[53] S. Yonezawa, "Nematic superconductivity in doped Bi_2Se_3 topological superconductors," *Condens. Matter*, vol. 4, p. 2, Dec. 2018.

[54] N. Gedik, P. Blake, R. C. Spitzer, J. Orenstein, R. Liang, D. A. Bonn, and W. N. Hardy, "Single-quasiparticle stability and quasiparticle-pair decay in $YBa_2Cu_3O_{6.5}$," *Physical Review B*, vol. 70, July 2004.

[55] R. D. Averitt, G. Rodriguez, A. I. Lobad, J. L. W. Siders, S. A. Trugman, and A. J. Taylor, "Nonequilibrium superconductivity and quasiparticle dynamics in $YBa_2Cu_3O_{7-\delta}$," *Physical Review B*, vol. 63, Mar. 2001.

[56] D. H. Torchinsky, G. F. Chen, J. L. Luo, N. L. Wang, and N. Gedik, "Band-dependent quasiparticle dynamics in single crystals of the $Ba_{0.6}K_{0.4}Fe_2As_2$ superconductor revealed by pump-probe spectroscopy," *Physical Review Letters*, vol. 105, July 2010.

[57] D. H. Torchinsky, J. W. McIver, D. Hsieh, G. F. Chen, J. L. Luo, N. L. Wang, and N. Gedik, "Nonequilibrium quasiparticle relaxation dynamics in single crystals of hole- and electron-doped $BaFe_2As_2$," *Physical Review B*, vol. 84, Sept. 2011.

[58] R. V. Yusupov, T. Mertelj, J.-H. Chu, I. R. Fisher, and D. Mihailovic, "Single-particle and collective mode couplings associated with 1- and 2-directional electronic ordering in metallic RTe_3 (R= Ho, Dy, Tb)," *Physical Review Letters*, vol. 101, Dec. 2008.

[59] R. Y. Chen, S. J. Zhang, E. D. Bauer, J. D. Thompson, and N. L. Wang, "Optical spectroscopy and ultrafast pump-probe studies on the heavy-fermion compound $CePt_2In_7$," *Physical Review B*, vol. 94, July 2016.

[60] N. Kumar, B. A. Ruzicka, N. P. Butch, P. Syers, K. Kirshenbaum, J. Paglione, and H. Zhao, "Spatially resolved femtosecond pump-probe study of topological insulator Bi_2Se_3," *Physical Review B*, vol. 83, June 2011.

[61] L. Cheng, C. La–o–vorakiat, C. S. Tang, S. K. Nair, B. Xia, L. Wang, J.-X. Zhu, and E. E. M. Chia, "Temperature-dependent ultrafast carrier and phonon dynamics of topological insulator $Bi_{1.5}Sb_{0.5}Te_{1.8}Se_{1.2}$," *Applied Physics Letters*, vol. 104, p. 211906, May 2014.

[62] Y. D. Glinka, S. Babakiray, T. A. Johnson, M. B. Holcomb, and D. Lederman, "Acoustic phonon dynamics in thin-films of the topological insulator Bi_2Se_3," *Journal of Applied Physics*, vol. 117, p. 165703, Apr. 2015.

[63] R. D. Averitt and A. J. Taylor, "Ultrafast optical and far-infrared quasiparticle dynamics in correlated electron materials," *Journal of Physics: Condensed Matter*, vol. 14, pp. R1357–R1390, Dec. 2002.

[64] A. Ashoka, R. R. Tamming, A. V. Girija, H. Bretscher, S. D. Verma, S.-D. Yang, C.-H. Lu, J. M. Hodgkiss, D. Ritchie, C. Chen, C. G. Smith, C. Schnedermann, M. B. Price, K. Chen, and A. Rao, "Extracting quantitative dielectric properties from pump-probe spectroscopy," *Nature Communications*, vol. 13, Mar. 2022.

[65] M. Rohlfing and S. G. Louie, "Electron-hole excitations and optical spectra from first principles," *Physical Review B*, vol. 62, pp. 4927–4944, Aug. 2000.

[66] C. J. Stevens, D. Smith, C. Chen, J. F. Ryan, B. Podobnik, D. Mihailovic, G. A. Wagner, and J. E. Evetts, "Evidence for two-component high-temperature superconductivity in the femtosecond optical response of $YBa_2Cu_3O_7$," *Physical Review Letters*, vol. 78, pp. 2212–2215, Mar. 1997.

[67] V. V. Kabanov, J. Demsar, B. Podobnik, and D. Mihailovic, "Quasiparticle relaxation dynamics in superconductors with different gap structures: Theory and experiments on YBCO," *Physical Review B*, vol. 59, pp. 1497–1506, Jan. 1999.

[68] J. Demsar, B. Podobnik, V. V. Kabanov, T. Wolf, and D. Mihailovic, "Superconducting gap Δ_c, the pseudogap Δ_p, and pair fluctuations above T_c in overdoped $Y_{1-x}Ca_xBa_2Cu_3O_{7-\delta}$ from femtosecond time-domain spectroscopy," *Physical Review Letters*, vol. 82, pp. 4918–4921, June 1999.

[69] J. Demsar, L. Forró, H. Berger, and D. Mihailovic, "Femtosecond snapshots of gap-forming charge-density-wave correlations in quasi-two-dimensional dichalcogenides $1\,T$–TaS_2 and $2H$–$TaSe_2$," *Physical Review B*, vol. 66, June 2002.

[70] J. Demsar, R. D. Averitt, K. H. Ahn, M. J. Graf, S. A. Trugman, V. V. Kabanov, J. L. Sarrao, and A. J. Taylor, "Quasiparticle relaxation dynamics in heavy fermion compounds," *Physical Review Letters*, vol. 91, July 2003.

[71] L. Stojchevska, P. Kusar, T. Mertelj, V. V. Kabanov, X. Lin, G. H. Cao, Z. A. Xu, and D. Mihailovic, "Electron-phonon coupling and the charge gap of spin-density wave iron-pnictide materials from quasiparticle relaxation dynamics," *Physical Review B*, vol. 82, July 2010.

[72] I. M. Vishik, F. Mahmood, Z. Alpichshev, N. Gedik, J. Higgins, and R. L. Greene, "Ultrafast dynamics in the presence of antiferromagnetic correlations in electron-doped cuprate $La_{2-x}Ce_xCuO_4$," *Physical Review B*, vol. 95, Mar. 2017.

[73] W. Putnam, "EEC 289K: Ultrafast photonics course notes," *UC Davis*, 2020.

[74] F. X. Kärtner, *Ultrafast Optics*. Massachusetts Institute of Technology, 2021.

[75] "Mai Tai mode-locked Ti:sapphire laser user's manual (Spectra Physics),"

[76] A. L. Gross, Y. Hou, A. Rossi, D. Yu, and I. M. Vishik, "Nanosecond dynamics in intrinsic topological insulator $Bi_{2-x}Sb_xSe_3$ revealed by time-resolved optical reflectivity," *Physical Review B*, vol. 103, Jan. 2021.

[77] J. Qi, X. Chen, W. Yu, P. Cadden-Zimansky, D. Smirnov, N. H. Tolk, I. Miotkowski, H. Cao, Y. P. Chen, Y. Wu, S. Qiao, and Z. Jiang, "Ultrafast carrier and phonon dynamics in Bi_2Se_3 crystals," *Applied Physics Letters*, vol. 97, p. 182102, Nov. 2010.

[78] Y.-P. Lai, H.-J. Chen, K.-H. Wu, and J.-M. Liu, "Temperature-dependent carrier-phonon coupling in topological insulator Bi_2Se_3," *Applied Physics Letters*, vol. 105, p. 232110, Dec. 2014.

[79] G. Jnawali, S. Linser, I. A. Shojaei, S. Pournia, H. E. Jackson, L. M. Smith, R. F. Need, and S. D. Wilson, "Revealing optical transitions and carrier recombination dynamics within the bulk band structure of Bi_2Se_3," *Nano Letters*, vol. 18, pp. 5875–5884, Aug. 2018.

[80] S. Sim, M. Brahlek, N. Koirala, S. Cha, S. Oh, and H. Choi, "Ultrafast terahertz dynamics of hot Dirac-electron surface scattering in the topological insulator Bi_2Se_3," *Physical Review B*, vol. 89, Apr. 2014.

[81] R. V. Aguilar, J. Qi, M. Brahlek, N. Bansal, A. Azad, J. Bowlan, S. Oh, A. J. Taylor, R. P. Prasankumar, and D. A. Yarotski, "Time-resolved terahertz dynamics in thin films of the topological insulator Bi_2Se_3," *Applied Physics Letters*, vol. 106, p. 011901, Jan. 2015.

[82] W. Richter and C. R. Becker, "A Raman and far-infrared investigation of phonons in the rhombohedral V_2–VI_3 compounds Bi_2Te_3, Bi_2Se_3, Sb_2Te_3 and $Bi_2(Te_{1-x}Se_x)_3$ $(0 < x < 1)$, $(Bi_{1-y}Sb_y)_2Te_3$ $(0 < y < 1)$," *Physica Status Solidi (b)*, vol. 84, pp. 619–628, Dec. 1977.

[83] H. J. Zeiger, J. Vidal, T. K. Cheng, E. P. Ippen, G. Dresselhaus, and M. S. Dresselhaus, "Theory for displacive excitation of coherent phonons," *Physical Review B*, vol. 45, pp. 768–778, Jan. 1992.

[84] P. G. Klemens, "Anharmonic decay of optical phonons," *Physical Review*, vol. 148, pp. 845–848, Aug. 1966.

[85] J. W. McIver, D. Hsieh, S. G. Drapcho, D. H. Torchinsky, D. R. Gardner, Y. S. Lee, and N. Gedik, "Theoretical and experimental study of second harmonic generation from the surface of the topological insulator Bi_2Se_3," *Physical Review B*, vol. 86, July 2012.

[86] P. B. Allen, "Theory of thermal relaxation of electrons in metals," *Physical Review Letters*, vol. 59, pp. 1460–1463, Sept. 1987.

[87] R. H. M. Groeneveld, R. Sprik, and A. Lagendijk, "Femtosecond spectroscopy of electron-electron and electron-phonon energy relaxation in Ag and Au," *Physical Review B*, vol. 51, pp. 11433–11445, May 1995.

[88] Y. H. Wang, D. Hsieh, E. J. Sie, H. Steinberg, D. R. Gardner, Y. S. Lee, P. Jarillo-Herrero, and N. Gedik, "Measurement of intrinsic Dirac fermion cooling on the surface of the topological insulator Bi_2Se_3 using time-resolved and angle-resolved photoemission spectroscopy," *Physical Review Letters*, vol. 109, Sept. 2012.

[89] J. Sobota, S.-L. Yang, D. Leuenberger, A. Kemper, J. Analytis, I. Fisher, P. Kirchmann, T. Devereaux, and Z.-X. Shen, "Distinguishing bulk and surface electron-phonon coupling in the topological insulator Bi_2Se_3 using time-resolved photoemission spectroscopy," *Physical Review Letters*, vol. 113, Oct. 2014.

[90] B. Xia, P. Ren, A. Sulaev, P. Liu, S.-Q. Shen, and L. Wang, "Indications of surface-dominated transport in single crystalline nanoflake devices of topological insulator $Bi_{1.5}Sb_{0.5}Te_{1.8}Se_{1.2}$," *Physical Review B*, vol. 87, Feb. 2013.

[91] Y. Onishi, Z. Ren, K. Segawa, W. Kaszub, M. Lorenc, Y. Ando, and K. Tanaka, "Ultrafast carrier relaxation through Auger recombination in the topological insulator $Bi_{1.5}Sb_{0.5}Te_{1.7}Se_{1.3}$," *Physical Review B*, vol. 91, Feb. 2015.

[92] T. Plecháček, J. Navrátil, and J. Horák, "Free current carrier concentration and point defects in $Bi_{2-x}Sb_xSe_3$ crystals," *Journal of Solid State Chemistry*, vol. 165, pp. 35–41, Apr. 2002.

[93] J. W. McIver, D. Hsieh, H. Steinberg, P. Jarillo-Herrero, and N. Gedik, "Control over topological insulator photocurrents with light polarization," *Nature Nanotechnology*, vol. 7, pp. 96–100, Dec. 2011.

[94] T. R. Devidas, E. P. Amaladass, S. Sharma, A. Mani, R. Rajaraman, C. S. Sundar, and A. Bharathi, "Effect of Sb substitution on the topological surface states in Bi_2Se_3 single crystals: a magneto-transport study," *Materials Research Express*, vol. 4, p. 026101, Feb. 2017.

[95] Y. Zhang, K. He, C.-Z. Chang, C.-L. Song, L.-L. Wang, X. Chen, J.-F. Jia, Z. Fang, X. Dai, W.-Y. Shan, S.-Q. Shen, Q. Niu, X.-L. Qi, S.-C. Zhang, X.-C. Ma, and Q.-K. Xue, "Crossover of the three-dimensional topological insulator Bi_2Se_3 to the two-dimensional limit," *Nature Physics*, vol. 6, pp. 584–588, June 2010.

[96] M. Weis, B. Wilk, G. Vaudel, K. Balin, R. Rapacz, A. Bulou, B. Arnaud, J. Szade, and P. Ruello, "Quantum size effect on charges and phonons ultrafast dynamics in atomically controlled nanolayers of topological insulators Bi_2Te_3," *Scientific Reports*, vol. 7, Oct. 2017.

[97] A. Crepaldi, F. Cilento, B. Ressel, C. Cacho, J. C. Johannsen, M. Zacchigna, H. Berger, P. Bugnon, C. Grazioli, I. C. E. Turcu, E. Springate, K. Kern, M. Grioni, and F. Parmigiani, "Evidence of reduced surface electron-phonon scattering in the conduction band of Bi_2Se_3 by nonequilibrium ARPES," *Physical Review B*, vol. 88, Sept. 2013.

[98] J. Sobota, S.-L. Yang, D. Leuenberger, A. Kemper, J. Analytis, I. Fisher, P. Kirchmann, T. Devereaux, and Z.-X. Shen, "Ultrafast electron dynamics in the topological insulator Bi_2Se_3 studied by time-resolved photoemission spectroscopy," *Journal of Electron Spectroscopy and Related Phenomena*, vol. 195, pp. 249–257, Aug. 2014.

[99] A. Sterzi, G. Manzoni, L. Sbuelz, F. Cilento, M. Zacchigna, P. Bugnon, A. Magrez, H. Berger, A. Crepaldi, and F. Parmigiani, "Bulk diffusive relaxation mechanisms in optically excited topological insulators," *Physical Review B*, vol. 95, Mar. 2017.

[100] K. Sumida, Y. Ishida, S. Zhu, M. Ye, A. Pertsova, C. Triola, K. A. Kokh, O. E. Tereshchenko, A. V. Balatsky, S. Shin, and A. Kimura, "Prolonged duration of nonequilibrated Dirac fermions in neutral topological insulators," *Scientific Reports*, vol. 7, Oct. 2017.

[101] F. Freyse, M. Battiato, L. V. Yashina, and J. Sánchez-Barriga, "Impact of ultrafast transport on the high-energy states of a photoexcited topological insulator," *Physical Review B*, vol. 98, Sept. 2018.

[102] J. Zhang, Z. Peng, A. Soni, Y. Zhao, Y. Xiong, B. Peng, J. Wang, M. S. Dresselhaus, and Q. Xiong, "Raman spectroscopy of few-quintuple layer topological insulator Bi_2Se_3 nanoplatelets," *Nano Letters*, vol. 11, pp. 2407–2414, May 2011.

[103] C. W. Luo, H. J. Wang, S. A. Ku, H.-J. Chen, T. T. Yeh, J.-Y. Lin, K. H. Wu, J. Y. Juang, B. L. Young, T. Kobayashi, C.-M. Cheng, C.-H. Chen, K.-D. Tsuei, R. Sankar, F. C. Chou, K. A. Kokh, O. E. Tereshchenko, E. V. Chulkov, Y. M. Andreev, and G. D. Gu, "Snapshots of Dirac fermions near the Dirac point in topological insulators," *Nano Letters*, vol. 13, pp. 5797–5802, Nov. 2013.

[104] M. Hajlaoui, E. Papalazarou, J. Mauchain, L. Perfetti, A. Taleb-Ibrahimi, F. Navarin, M. Monteverde, P. Auban-Senzier, C. Pasquier, N. Moisan, D. Boschetto, M. Neupane, M. Hasan, T. Durakiewicz, Z. Jiang, Y. Xu, I. Miotkowski, Y. Chen, S. Jia, H. Ji, R. Cava, and M. Marsi, "Tuning a Schottky barrier in a photoexcited topological insulator with transient Dirac cone electron-hole asymmetry," *Nature Communications*, vol. 5, Jan. 2014.

[105] S. Ciocys, T. Morimoto, J. E. Moore, and A. Lanzara, "Tracking surface photovoltage dipole geometry in Bi_2Se_3 with time-resolved photoemission," *Journal of Statistical Mechanics: Theory and Experiment*, vol. 2019, p. 104008, Oct. 2019.

[106] S. Ciocys, T. Morimoto, R. Mori, K. Gotlieb, Z. Hussain, J. G. Analytis, J. E. Moore, and A. Lanzara, "Manipulating long-lived topological surface photovoltage in bulk-insulating topological insulators Bi_2Se_3 and Bi_2Te_3," *npj Quantum Materials*, vol. 5, Mar. 2020.

[107] X. Lu, O. Khatib, X. Du, J. Duan, W. Wei, X. Liu, H. A. Bechtel, F. D'Apuzzo, M. Yan, A. Buyanin, Q. Fu, J. Chen, M. Salmeron, J. Zeng, M. B. Raschke, P. Jiang, and X. Bao, "Nanoimaging of electronic heterogeneity in Bi_2Se_3 and Sb_2Te_3 nanocrystals," *Advanced Electronic Materials*, vol. 4, p. 1700377, Dec. 2017.

[108] M. Lewin, L. Mester, T. Saltzmann, S.-J. Chong, M. Kaminski, B. Hauer, M. Pohlmann, A. M. Mio, M. Wirtssohn, P. Jost, M. Wuttig, U. Simon, and T. Taubner, "Sb_2Te_3 growth study reveals that formation of nanoscale charge carrier domains is an intrinsic feature relevant for electronic applications," *ACS Applied Nano Materials*, vol. 1, pp. 6834–6842, Nov. 2018.

[109] D. K. Schroder, "Surface voltage and surface photovoltage: history, theory and applications," *Measurement Science and Technology*, vol. 12, pp. R16–R31, Feb. 2001.

[110] T. Yoshikawa, Y. Ishida, K. Sumida, J. Chen, K. A. Kokh, O. E. Tereshchenko, S. Shin, and A. Kimura, "Enhanced photovoltage on the surface of topological insulator via optical aging," *Applied Physics Letters*, vol. 112, p. 192104, May 2018.

[111] L. V. Butov, A. C. Gossard, and D. S. Chemla, "Macroscopically ordered state in an exciton system," *Nature*, vol. 418, pp. 751–754, Aug. 2002.

[112] J. P. Eisenstein and A. H. MacDonald, "Bose-Einstein condensation of excitons in bilayer electron systems," *Nature*, vol. 432, pp. 691–694, Dec. 2004.

[113] A. Kogar, M. S. Rak, S. Vig, A. A. Husain, F. Flicker, Y. I. Joe, L. Venema, G. J. MacDougall, T. C. Chiang, E. Fradkin, J. van Wezel, and P. Abbamonte, "Signatures of exciton condensation in a transition metal dichalcogenide," *Science*, vol. 358, pp. 1314–1317, Dec. 2017.

[114] Z. Wang, D. A. Rhodes, K. Watanabe, T. Taniguchi, J. C. Hone, J. Shan, and K. F. Mak, "Evidence of high-temperature exciton condensation in two-dimensional atomic double layers," *Nature*, vol. 574, pp. 76–80, Oct. 2019.

[115] R. Mori, S. Ciocys, K. Takasan, P. Ai, K. Currier, T. Morimoto, J. E. Moore, and A. Lanzara, "Spin-polarized spatially indirect excitons in a topological insulator," *Nature*, vol. 614, pp. 249–255, Feb. 2023.

[116] G. Y. Cho and J. E. Moore, "Quantum phase transition and fractional excitations in a topological insulator thin film with Zeeman and excitonic masses," *Physical Review B*, vol. 84, Oct. 2011.

[117] D. Tilahun, B. Lee, E. M. Hankiewicz, and A. H. MacDonald, "Quantum Hall superfluids in topological insulator thin films," *Physical Review Letters*, vol. 107, Dec. 2011.

[118] E. G. Moon and C. Xu, "Exciton condensation in thin-film topological insulator," *Europhysics Letters*, vol. 97, p. 66008, Mar. 2012.

[119] M. P. Mink, H. T. C. Stoof, R. A. Duine, M. Polini, and G. Vignale, "Probing the topological exciton condensate via Coulomb drag," *Physical Review Letters*, vol. 108, May 2012.

[120] D. K. Efimkin, Y. E. Lozovik, and A. A. Sokolik, "Electron-hole pairing in a topological insulator thin film," *Physical Review B*, vol. 86, Sept. 2012.

[121] S. Rist, A. A. Varlamov, A. H. MacDonald, R. Fazio, and M. Polini, "Photoemission spectra of massless Dirac fermions on the verge of exciton condensation," *Physical Review B*, vol. 87, Feb. 2013.

[122] C. Triola, A. Pertsova, R. S. Markiewicz, and A. V. Balatsky, "Excitonic gap formation in pumped Dirac materials," *Physical Review B*, vol. 95, May 2017.

[123] A. Pertsova and A. V. Balatsky, "Dynamically induced excitonic instability in pumped Dirac materials," *Annalen der Physik*, vol. 532, p. 1900549, Jan. 2020.

[124] N. P. Butch, K. Kirshenbaum, P. Syers, A. B. Sushkov, G. S. Jenkins, H. D. Drew, and J. Paglione, "Strong surface scattering in ultrahigh-mobility Bi_2Se_3 topological insulator crystals," *Physical Review B*, vol. 81, June 2010.

[125] F. Xiu, L. He, Y. Wang, L. Cheng, L.-T. Chang, M. Lang, G. Huang, X. Kou, Y. Zhou, X. Jiang, Z. Chen, J. Zou, A. Shailos, and K. L. Wang, "Manipulating surface states in topological insulator nanoribbons," *Nature Nanotechnology*, vol. 6, pp. 216–221, Feb. 2011.

[126] A. L. Gross, L. Falling, M. C. Staab, M. I. Montero, R. R. Ullah, D. M. Nisson, P. Klavins, K. J. Koski, N. J. Curro, V. Taufour, S. Nemsak, and I. M. Vishik, "Copper migration and surface oxidation of

$Cu_xBi_2Se_3$ in ambient pressure environments," *Journal of Physics: Materials*, vol. 5, p. 044005, Oct. 2022.

[127] A. Rossi, V. Ivanov, S. Sreedhar, A. L. Gross, Z. Shen, E. Rotenberg, A. Bostwick, C. Jozwiak, V. Taufour, S. Y. Savrasov, and I. M. Vishik, "Electronic structure and topology across T_c in the magnetic Weyl semimetal $Co_3Sn_2S_2$," *Physical Review B*, vol. 104, Oct. 2021.

[128] A. Damascelli, Z. Hussain, and Z.-X. Shen, "Angle-resolved photoemission studies of the cuprate superconductors," *Reviews of Modern Physics*, vol. 75, pp. 473–541, Apr. 2003.

[129] A. Damascelli, "Probing the electronic structure of complex systems by ARPES," *Physica Scripta*, vol. T109, p. 61, 2004.

[130] M. P. Seah and W. A. Dench, "Quantitative electron spectroscopy of surfaces: A standard data base for electron inelastic mean free paths in solids," *Surface and Interface Analysis*, vol. 1, pp. 2–11, Feb. 1979.

[131] S. Tougaard, "Practical guide to the use of backgrounds in quantitative XPS," *Journal of Vacuum Science & Technology A*, vol. 39, p. 011201, Jan. 2021.

[132] P. Zhang, P. Richard, T. Qian, Y.-M. Xu, X. Dai, and H. Ding, "A precise method for visualizing dispersive features in image plots," *Review of Scientific Instruments*, vol. 82, p. 043712, Apr. 2011.

[133] R. A. Fisher, "Foundations of nonlinear optics course notes," *CLEO: Conference on Lasers and Electro-Optics*, 2018.

[134] J. D. Koralek, J. F. Douglas, N. C. Plumb, J. D. Griffith, S. T. Cundiff, H. C. Kapteyn, M. M. Murnane, and D. S. Dessau, "Experimental setup for low-energy laser-based angle resolved photoemission spectroscopy," *Review of Scientific Instruments*, vol. 78, p. 053905, May 2007.

[135] E. Kotta, L. Miao, Y. Xu, S. A. Breitweiser, C. Jozwiak, A. Bostwick, E. Rotenberg, W. Zhang, W. Wu, T. Suzuki, J. Checkelsky, and L. A. Wray, "Spectromicroscopic measurement of surface and bulk band structure interplay in a disordered topological insulator," *Nature Physics*, vol. 16, pp. 285–289, Jan. 2020.

[136] E. Rotenberg and A. Bostwick, "microARPES and nanoARPES at diffraction-limited light sources: opportunities and performance gains," *Journal of Synchrotron Radiation*, vol. 21, pp. 1048–1056, Aug. 2014.

[137] G. P. Williams, *X-Ray Data Booklet*. Lawrence Berkeley National Laboratory, University of California, Berkeley, 2001.

[138] CasaXPS, *http://www.casaxps.com*.

[139] KolXPD, *https://www.kolibrik.net/en/solutions-products/kolxpd*.

[140] F. A. Stevie and C. L. Donley, "Introduction to X-ray photoelectron spectroscopy," *Journal of Vacuum Science &amp Technology A*, vol. 38, p. 063204, Dec. 2020.

[141] A. G. Shard, "Practical guides for X-ray photoelectron spectroscopy: Quantitative XPS," *Journal of Vacuum Science & Technology A*, vol. 38, p. 041201, July 2020.

[142] J. Yeh and I. Lindau, "Atomic subshell photoionization cross sections and asymmetry parameters: $1 \leq Z \leq 103$," *Atomic Data and Nuclear Data Tables*, vol. 32, pp. 1–155, Jan. 1985.

[143] S. Tanuma, C. J. Powell, and D. R. Penn, "Calculations of electron inelastic mean free paths. v. data for 14 organic compounds over the 50-2000 eV range," *Surface and Interface Analysis*, vol. 21, pp. 165–176, Mar. 1994.

[144] J. Yeh, *Atomic Calculation of Photoionization Cross-Sections and Asymmetry Parameters*. Gordon and Breach Science Publishers, 1993.

[145] Lawrence Berkeley National Laboratory, "Advanced Light Source quick facts," 2018.

[146] M. Salmeron and R. Schlögl, "Ambient pressure photoelectron spectroscopy: A new tool for surface science and nanotechnology," *Surface Science Reports*, vol. 63, pp. 169–199, Apr. 2008.

[147] M. E. Grass, P. G. Karlsson, F. Aksoy, M. Lundqvist, B. Wannberg, B. S. Mun, Z. Hussain, and Z. Liu, "New ambient pressure photoemission endstation at Advanced Light Source Beamline 9.3.2," *Review of Scientific Instruments*, vol. 81, p. 053106, May 2010.

[148] J. Schnadt, J. Knudsen, and N. Johansson, "Present and new frontiers in materials research by ambient pressure X-ray photoelectron spectroscopy," *Journal of Physics: Condensed Matter*, vol. 32, p. 413003, July 2020.

[149] K. Paraskevopoulos, E. Hatzikraniotis, K. Chrisafis, M. Zamani, J. Stoemenos, N. Economou, K. Alexiadis, and M. Balkanski, "Intercalation studies in bismuth selenide," *Materials Science and Engineering: B*, vol. 1, pp. 147–154, Nov. 1988.

[150] J. Bludská, I. Jakubec, S. Karamazov, J. Horák, and C. Uher, "Lithium ions in the van der Waals gap of Bi_2Se_3 single crystals," *Journal of Solid State Chemistry*, vol. 183, pp. 2813–2817, Dec. 2010.

[151] Y. H. Choi, N. H. Jo, K. J. Lee, J. B. Yoon, C. Y. You, and M. H. Jung, "Transport and magnetic properties of Cr-, Fe-, Cu-doped topological insulators," *Journal of Applied Physics*, vol. 109, p. 07E312, Apr. 2011.

[152] Shruti, V. K. Maurya, P. Neha, P. Srivastava, and S. Patnaik, "Superconductivity by Sr intercalation in the layered topological insulator Bi_2Se_3," *Physical Review B*, vol. 92, July 2015.

[153] K. Mazumder, A. Sharma, Y. Kumar, and P. M. Shirage, "Effect of Cu intercalation on humidity sensing properties of Bi_2Se_3 topological insulator single crystals," *Phys. Chem. Chem. Phys.*, vol. 20, no. 44, pp. 28257–28266, 2018.

[154] S.-H. Wang, D. Shen, T.-W. Yang, I.-N. Chen, C.-H. Wang, and L.-M. Wang, "Large positive magnetoresistance with high Hall mobility and intercalation of Fe dopants in the quenched Bi_2Te_3 single crystals," *Journal of Alloys and Compounds*, vol. 844, p. 156153, Dec. 2020.

[155] T. Kawai, C. G. Wang, Y. Kandori, Y. Honoki, K. Matano, T. Kambe, and G.-Q. Zheng, "Direction and symmetry transition of the vector order parameter in topological superconductors $Cu_xBi_2Se_3$," *Nature Communications*, vol. 11, Jan. 2020.

[156] J. A. Schneeloch, R. D. Zhong, Z. J. Xu, G. D. Gu, and J. M. Tranquada, "Dependence of superconductivity in $Cu_xBi_2Se_3$ on quenching conditions," *Physical Review B*, vol. 91, Apr. 2015.

[157] M. Whittingham, "Chemistry of intercalation compounds: Metal guests in chalcogenide hosts," *Progress in Solid State Chemistry*, vol. 12, pp. 41–99, Jan. 1978.

[158] A. G. Ryabishchenkova, M. M. Otrokov, V. M. Kuznetsov, and E. V. Chulkov, "Ab initio study of the adsorption, diffusion, and intercalation of alkali metal atoms on the (0001) surface of the topological insulator Bi_2Se_3," *Journal of Experimental and Theoretical Physics*, vol. 121, pp. 465–476, Sept. 2015.

[159] M. Ye, K. Kuroda, M. M. Otrokov, A. G. Ryabishchenkova, Q. Jiang, A. Ernst, E. V. Chulkov, M. Nakatake, M. Arita, T. Okuda, T. Matsushita, L. Tóth, H. Daimon, K. Shimada, Y. Ueda, and A. Kimura, "Persistence of the topological surface states in Bi_2Se_3 against Ag intercalation at room temperature," *The Journal of Physical Chemistry C*, vol. 125, pp. 1784–1792, Jan. 2021.

[160] K. J. Koski, J. J. Cha, B. W. Reed, C. D. Wessells, D. Kong, and Y. Cui, "High-density chemical intercalation of zero-valent copper into Bi_2Se_3 nanoribbons," *Journal of the American Chemical Society*, vol. 134, pp. 7584–7587, Apr. 2012.

[161] S.-H. Yu, T. L. Hung, M.-N. Ou, M. M. C. Chou, and Y.-Y. Chen, "Zero Cu valence and superconductivity in high-quality $Cu_xBi_2Se_3$ crystal," *Physical Review B*, vol. 100, Nov. 2019.

[162] Y. Fang, W.-L. You, and M. Li, "Unconventional superconductivity in $Cu_xBi_2Se_3$ from magnetic susceptibility and electrical transport," *New Journal of Physics*, vol. 22, p. 053026, May 2020.

[163] V. Nascimento, V. de Carvalho, R. Paniago, E. Soares, L. Ladeira, and H. Pfannes, "XPS and EELS study of the bismuth selenide," *Journal of Electron Spectroscopy and Related Phenomena*, vol. 104, pp. 99–107, July 1999.

[164] H. M. Benia, C. Lin, K. Kern, and C. R. Ast, "Reactive chemical doping of the Bi_2Se_3 topological insulator," *Physical Review Letters*, vol. 107, Oct. 2011.

[165] C. Chen, S. He, H. Weng, W. Zhang, L. Zhao, H. Liu, X. Jia, D. Mou, S. Liu, J. He, Y. Peng, Y. Feng, Z. Xie, G. Liu, X. Dong, J. Zhang, X. Wang, Q. Peng, Z. Wang, S. Zhang, F. Yang, C. Chen, Z. Xu, X. Dai, Z. Fang, and X. J. Zhou, "Robustness of topological order and formation of quantum well states in topological insulators exposed to ambient environment," *Proceedings of the National Academy of Sciences*, vol. 109, pp. 3694–3698, Feb. 2012.

[166] A. J. Green, S. Dey, Y. Q. An, B. O'Brien, S. O'Mullane, B. Thiel, and A. C. Diebold, "Surface oxidation of the topological insulator Bi_2Se_3," *Journal of Vacuum Science & Technology A: Vacuum, Surfaces, and Films*, vol. 34, p. 061403, Nov. 2016.

[167] C. R. Thomas, M. K. Vallon, M. G. Frith, H. Sezen, S. K. Kushwaha, R. J. Cava, J. Schwartz, and S. L. Bernasek, "Surface oxidation of $Bi_2(Te, Se)_3$ topological insulators depends on cleavage accuracy," *Chemistry of Materials*, vol. 28, pp. 35–39, Dec. 2015.

[168] K. Sakamoto, H. Ishikawa, T. Wake, C. Ishimoto, J. Fujii, H. Bentmann, M. Ohtaka, K. Kuroda, N. Inoue, T. Hattori, T. Miyamachi, F. Komori, I. Yamamoto, C. Fan, P. Krüger, H. Ota, F. Matsui, F. Reinert, J. Avila, and M. C. Asensio, "Spatial control of charge doping in n-type topological insulators," *Nano Letters*, vol. 21, pp. 4415–4422, May 2021.

[169] J. Yang, B. Zheng, Z. Chen, W. Xu, R. Wang, and H. Xu, "Robust topological states in Bi_2Se_3 against surface oxidation," *The Journal of Physical Chemistry C*, vol. 124, pp. 6253–6259, Feb. 2020.

[170] Y. Tanaka, K. Nakayama, S. Souma, T. Sato, N. Xu, P. Zhang, P. Richard, H. Ding, Y. Suzuki, P. Das, K. Kadowaki, and T. Takahashi, "Evolution of electronic structure upon Cu doping in the topological insulator Bi_2Se_3," *Physical Review B*, vol. 85, Mar. 2012.

[171] L. V. Yashina, J. Sánchez-Barriga, M. R. Scholz, A. A. Volykhov, A. P. Sirotina, S. N. Vera, M. E. Tamm, A. Varykhalov, D. Marchenko, G. Springholz, G. Bauer, A. Knop-Gericke, and O. Rader, "Negligible surface reactivity of topological insulators Bi_2Se_3 and Bi_2Te_3 towards oxygen and water," *ACS Nano*, vol. 7, pp. 5181–5191, May 2013.

[172] V. V. Atuchin, V. A. Golyashov, K. A. Kokh, I. V. Korolkov, A. S. Kozhukhov, V. N. Kruchinin, S. V. Makarenko, L. D. Pokrovsky, I. P. Prosvirin, K. N. Romanyuk, and O. E. Tereshchenko, "Formation of inert Bi_2Se_3 (0001) cleaved surface," *Crystal Growth & Design*, vol. 11, pp. 5507–5514, Oct. 2011.

[173] D. Biswas, S. Thakur, K. Ali, G. Balakrishnan, and K. Maiti, "Anomalies of a topologically ordered surface," *Scientific Reports*, vol. 5, June 2015.

[174] M. Bianchi, D. Guan, S. Bao, J. Mi, B. B. Iversen, P. D. King, and P. Hofmann, "Coexistence of the topological state and a two-dimensional electron gas on the surface of Bi_2Se_3," *Nature Communications*, vol. 1, Nov. 2010.

[175] M. A. Tumelero, R. Faccio, and A. A. Pasa, "The role of interstitial native defects in the topological insulator Bi_2Se_3," *Journal of Physics: Condensed Matter*, vol. 28, p. 425801, Sept. 2016.

[176] Y.-L. Wang, Y. Xu, Y.-P. Jiang, J.-W. Liu, C.-Z. Chang, M. Chen, Z. Li, C.-L. Song, L.-L. Wang, K. He, X. Chen, W.-H. Duan, Q.-K. Xue, and X.-C. Ma, "Structural defects and electronic properties of the Cu-doped topological insulator Bi_2Se_3," *Physical Review B*, vol. 84, Aug. 2011.

[177] J. Morasch, S. Li, J. Brötz, W. Jaegermann, and A. Klein, "Reactively magnetron sputtered Bi_2O_3 thin films: Analysis of structure, optoelectronic, interface, and photovoltaic properties," *physica status solidi (a)*, vol. 211, pp. 93–100, Nov. 2013.

[178] D. Takane, S. Souma, T. Sato, T. Takahashi, K. Segawa, and Y. Ando, "Work function of bulk-insulating topological insulator $Bi_{2-x}Sb_xTe_{3-y}Se_y$," *Applied Physics Letters*, vol. 109, p. 091601, Aug. 2016.

[179] A. Vaško, L. Tichý, J. Horák, and J. Weissenstein, "Amphoteric nature of copper impurities in Bi_2Se_3 crystals," *Applied Physics*, vol. 5, pp. 217–221, Dec. 1974.

[180] W. Smekal, W. S. M. Werner, and C. J. Powell, "Simulation of electron spectra for surface analysis (SESSA): a novel software tool for quantitative Auger-electron spectroscopy and X-ray photoelectron spectroscopy," *Surface and Interface Analysis*, vol. 37, no. 11, pp. 1059–1067, 2005.

[181] W. S. M. Werner, W. Smekal, and C. J. Powell, "Simulation of electron spectra for surface analysis (SESSA) version 2.1," tech. rep., Dec. 2017.

[182] G. Jia, Z. Wu, P. Wang, J. Yao, and K. Chang, "Morphological evolution of self-deposition Bi_2Se_3 nanosheets by oxygen plasma treatment," *Scientific Reports*, vol. 6, Feb. 2016.